UNIVERSITY OF CALIFORNIA SAN DIEGO

Non-linear, Time-Variant and Reconfigurable Metasurfaces

A dissertation submitted in partial satisfaction of the
requirements for the degree Doctor of Philosophy

in

Electrical Engineering (Applied Electromagnetics)

by

Xiaozhen Yang

Committee in charge:

Professor Daniel F. Sievenpiper, Chair
Professor Prabhakar R. Bandaru
Professor Dinesh Bharadia
Professor Zhaowei Liu
Professor George C. Papen

2024

The Dissertation of Xiaozhen Yang is approved, and it is acceptable in quality and form for publication on microfilm and electronically.

University of California San Diego

2024

DEDICATION

TO MY FAMILY

ACKNOWLEDGEMENTS

My Ph.D. journey is an amazing experience. I am very lucky to have so many inspiring minds to guide me along the way.

My biggest thank goes to my advisor and mentor, Professor Daniel F. Sievenpiper, for always being responsive and supportive. He is full of innovative ideas and he always encourages me to explore my academic interest without setting any limitations. I also appreciate his trust in my ability to handle project timelines and never being pushy. It is really a pleasure and honor to work with him. I would like to thank my committee members, Professor Prabhakar R. Bandaru, Professor Dinesh Bharadia, Professor Zhaowei Liu and Professor George C. Papen, for their valuable suggestions and time.

I thank all my colleagues in the Applied Electromagnetic lab. Dr. Dia'aaldin Bisharat, thank you for your generous guidance and help when I just started. To Dr. Shreya Singh, thank you for all the gentle and sweet comfort when I am frustrated. To Dr. Yun Zhou, Dr. Kyle Thackston, Dr. Jiyeon Lee and Dr. Aobo Li, thank you for sharing valuable life experiences. To Dr. Matt Smith, thank you for all the delightful conversations and help on experimental setup. To Dr. Robert Davis, thank you for taking care of everything in the lab and thank you for always being enthusiastic. To Feng Li, thank you for always being kind and considerate.

I would like to thank my family and friends. My parents Zhongming Yuan and Hongchun Yang, thank you for your unconditional support and respect to all my decisions. To my fiance, Erda Wen, thank you for the encouragement during the hard times and thank you for always being there for me. To Hejia Tang, thank you for all the joy that we share since high school. To Sourpatch, thank you for the warm accompany in the late nights and for being the cutest alarm clock in the morning. I love you. This won't happen without you.

The material in this dissertation is based on the following papers or manuscripts.

Chapter 2 is based on the following paper: Yang, X., Wen, E., & Sievenpiper, D. F. (2022). "Broadband time-modulated absorber beyond the Bode-Fano limit for short pulses by energy trapping." *Physical Review Applied*, 17(4), 044003. The dissertation author was the

primary investigator and author of this paper.

Chapter 3 is based on the following paper: Yang, X., Wen, E., & Sievenpiper, D. F. (2022). "Power-Dependent Metasurface With Self-Induced Bandgap." *IEEE Antennas and Wireless Propagation Letters*, 21(6), 1115-1119. The dissertation author was the primary investigator and author of this paper.

Chapter 4 is based on the following paper: Yang, X., Wen, E., & Sievenpiper, D. F. (2023). "All-passive microwave-diode nonreciprocal metasurface." *Communications Physics*, 6(1), 333. The dissertation author was the primary investigator and author of this paper.

Chapter 5 is based on the following manuscript to be published: Yang, X., Wen, E., Bharadia, D., & Sievenpiper, D. F. (2024). "Multifunctional Metasurface: Simultaneous Beam Steering, Polarization Conversion and Phase Offset." *IEEE Transactions on Antennas and Propagation*, 72(5), 4589 - 4593. The dissertation author was the primary investigator and author of this paper.

VITA

2018	B. Eng. in Electrical Engineering, University of Electronic Science and Technology of China
2019	M. S. in Electrical Engineering, The Ohio State University
2024	Ph. D. in Electrical Engineering (Applied Electromagnetics), University of California San Diego

PUBLICATIONS

Xiaozhen Yang, Erda Wen, and Daniel F. Sievenpiper. "Broadband time-modulated absorber beyond the Bode-Fano limit for short pulses by energy trapping." *Physical Review Applied* 17.4 (2022): 044003.

Xiaozhen Yang, Erda Wen, and Daniel F. Sievenpiper. "Power-Dependent Metasurface With Self-Induced Bandgap." *IEEE Antennas and Wireless Propagation Letters* 21.6 (2022): 1115-1119.

Xiaozhen Yang, Erda Wen, and Daniel F. Sievenpiper. "All-passive Microwave-Diode Nonreciprocal Metasurface." *Communications Physics* 6.1 (2023): 333.

Xiaozhen Yang, Erda Wen, and Daniel F. Sievenpiper. "Multifunctional Metasurface: Simultaneous Beam Steering, Polarization Conversion and Phase Offset." *IEEE Transactions on Antennas and Propagation.* 72.5 (2024): 4589 - 4593.

Xiaozhen Yang, Erda Wen, and Daniel F. Sievenpiper. "Pseudo diffsusive surface wave enabling flat wavefront." *Physical Review Applied* 21.4 (2024): 044043.

Erda Wen, **Xiaozhen Yang**, and Daniel F. Sievenpiper. "Real-data-driven Real-time Reconfigurable Microwave Reflective Surface." *Nature Communications* 14.1 (2023): 7736.

Erda Wen, **Xiaozhen Yang**, and Daniel F. Sievenpiper. "Real-Time 2-D Beamforming With Rotatable Dielectric Slabs Enabled by Generative Neural Network." *IEEE Transactions on Antennas and Propagation* 70.9 (2022): 8360-8367.

Erda Wen, **Xiaozhen Yang**, and Daniel F. Sievenpiper. "Observing flat wavefront formation with diffusive transport in microwave graphene with topological insulator protected edges." *Applied Physics Letters* 118.16 (2021): 161102.

Erda Wen, J. Bisharat Dia'aaldin, Robert J. Davis, **Xiaozhen Yang**, and Daniel F. Sievenpiper. "Designing Topological Defect Lines Protected by Gauge-Dependent Symmetry Indicators."

Physical Review Applied 17.6 (2022): 064008.

Shreya Singh, Robert J. Davis, J. Bisharat Dia'aaldin, Jiyeon Lee, Sara M. Kandil, Erda Wen, **Xiaozhen Yang**, Yun Zhou, Prabhakar R. Bandaru, and Daniel F. Sievenpiper. "Advances in Metasurfaces: Topology, Chirality, Patterning, and Time Modulation." *IEEE Antennas and Propagation Magazine* 64.4 (2021): 51-62.

CONFERENCES

Xiaozhen Yang, Dinesh Bharadia, and Daniel F. Sievenpiper. "Simultaneous Beam-Steering and Polarization Conversion Using a Varactor-Integrated Metasurface." *2023 International Applied Computational Electromagnetics Society Symposium (ACES)*. IEEE, 2023.

Erda Wen, **Xiaozhen Yang**, and Daniel F. Sievenpiper. "Generative Neural Network Enables Reconfigurable Metasurface on Real-Time Free-Form Targets." *2023 International Applied Computational Electromagnetics Society Symposium (ACES)*. IEEE, 2023.

Erda Wen, **Xiaozhen Yang**, and Daniel F. Sievenpiper. "Surface Wave Wavefront Formation with Photonic Graphene and Topological Waveguide." *2022 IEEE International Symposium on Antennas and Propagation and USNC-URSI Radio Science Meeting (AP-S/URSI)*. IEEE, 2022.

ABSTRACT OF THE DISSERTATION

Non-linear, Time-Variant and Reconfigurable Metasurfaces

by

Xiaozhen Yang

Doctor of Philosophy in Electrical Engineering (Applied Electromagnetics)

University of California San Diego, 2024

Professor Daniel F. Sievenpiper, Chair

Metasurfaces, constructed with periodic subwavelength meta-atoms, have aroused wide attention since it exhibits extraordinary electromagnetic behaviours in wave manipulation from microwave regime to optical ranges. Meanwhile the low-cost, ease of fabrication and compact features make it more appealing for various applications. Researchers have shown that conventional linear-time-invariant (LTI) metasurfaces are capable of energy absorption, beam formation, radiation control and polarization conversion. However, their abilities are limited since the electromagnetic (EM) response is unchangeable regardless of input power and phase.

This dissertation discusses how to empower classic LTI metasurfaces with unconventional abilities by integrating nonlinear electronic devices. The integration of nonlinear device offers

more degrees of freedom to metasurfaces, enabling versatile abilities to meet complex growing demands in EM protection, isolation and wave manipulation. This dissertation theoretically and experimentally demonstrates four novel non-LTI or reconfigurable metasurfaces designs with promising application value. First, we propose a broadband absorber beyond the Bode-Fano limit by creating an energy trap using time-modulated switch/diodes. The second design realizes power-dependent reflection, instead of absorption, to realize EM protection. The triggering of the integrated diodes directly transforms the structure from a surface wave supportive state to a self-induced bandgap topology if exposed to high power RF illumination. The third concept proposes an all-passive and magnetic-free structure integrated with diodes to achieve nonreciprocity, which is a promising candidate for EM protecting layers and EM isolators/circulators. The last proposed varactor-based reconfigurable metasurface focuses on multifunctional wave manipulation, including beam steering, polarization conversion and phase offset. All these proposed structures expand the capability of wave manipulation and their applications compared to traditional LTI metasurfaces.

Chapter 1

Introduction

Electromagnetic wave plays an important role in human society ever since Maxwell's theory is experimentally proved, as it enables information transmission at the speed of light in the free space. It's high application value arouses highly attention from academic to industry and it has been widely used in imaging, sensing and communication. As the EM environment becomes increasingly complicated, researchers have been exploring more approaches to manipulate EM waves. Wave propagation, energy absorption, cloaking, interference reduction are intensively studied. Metasurfaces, the two-dimensional (2-D) counterpart of a metamaterial, draw attention due to its compatibility to modern electronic systems, low-profile characteristics and ease of fabrication. To meet the rising demands of efficient and safe communication, versatile non-linear-time-invariant and reconfigurable metasurface is proposed to improve the performance and tunability of conventional LTI metasurface in wideband absorption, power-dependent transmission, nonreciprocal propagation, etc.

1.1 Metasurface and Its Applications

Metamaterial arouses attention due to its unprecedented and versatile behaviour in wave manipulation from microwave frequency to optical range. By artificially engineering the structure of the metamaterial, as shown in Figure 1.1, rather than investigating the intrinsic chemical properties of bulk material, researchers have achieved properties that are not available in nature such as negative refractive index. Recent research advances to various applications from metamaterial antenna, absorbers, artificial magnetism, superlens and cloaking devices [1].

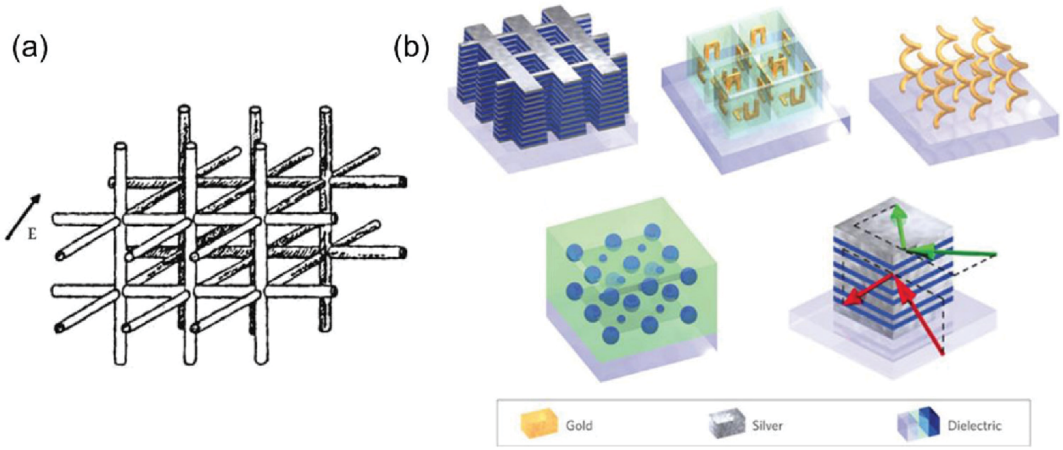

Figure 1.1. Examples of metamaterial structures (Source:[1]). (a) Early structure of artificial plasma using conducting wire at microwave frequency. (b) Modern structures at optical frequencies.

Metasurfaces, the 2-D counterpart of metamaterial, have the advantages of low-profile, low-cost, ease of fabrication and compatibility with modern electronic devices. Composed of periodic subwavelength metallic structures or dielectric patterning, metasurfaces is capable of manipulating the effective permittivity and permeability, thus controlling the dispersion, absorption and reflection characteristics of the surface.

One of the classic metasurfaces is high impedance surface as illustrated in Figure 1.2 (a) [2]. The metallic mushroom structure enables a complete bandgap from Γ to K by creating a resonance as illustrated in Figure 1.2 (c). The resonance is usually characterized by a parallel LC circuit, whose inductance and capacitance are related to the neighboring unit as shown in Figure

1.2 (b). Surface waves are forbidden and high impedance is observed within the bandgap, and the surface currents are suppressed, which makes it a popular candidate as an artificial perfect magnetic conductor.

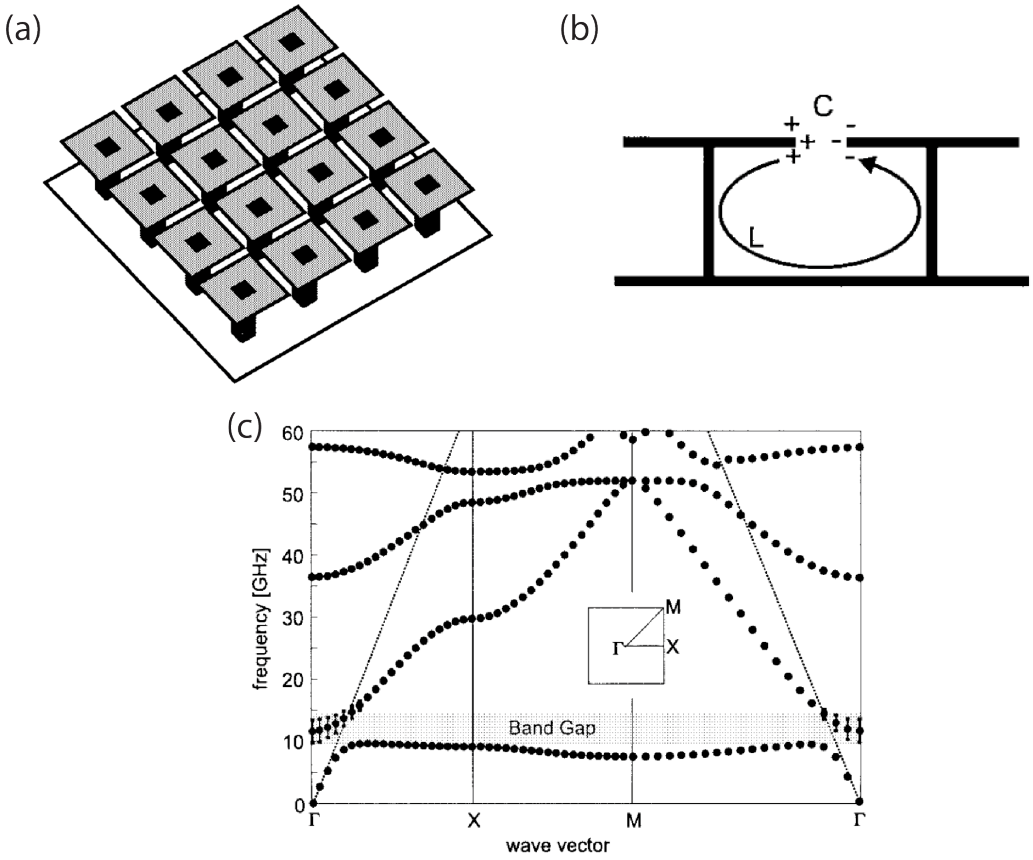

Figure 1.2. High impedance surface (Source:[2]). (a) Square unit HIS top view. (b) Equivalent circuit of HIS. (c) HIS band diagram.

Metasurfaces can also be used as low-profile absorbers as shown in Figure 1.3 [3]. Conventional metasurface absorbers consist of resonant structure and lossy substrate/components. Near the resonance, the EM waves interact intensively with the surface, resulting in higher loss. Take Figure 1.3 (b) as an example, this structure consists of two metamaterials that respond to the electric and magnetic fields separately. By artificially engineering the permittivity and permeability at the same time, it reaches perfect absorption by both eclectic and magnetic absorption as shown in Figure 1.3 (c). The advantage of metasurface absorbers is low-profile, light-weight and low cost. However, they are restricted by the bandwidth limit [4].

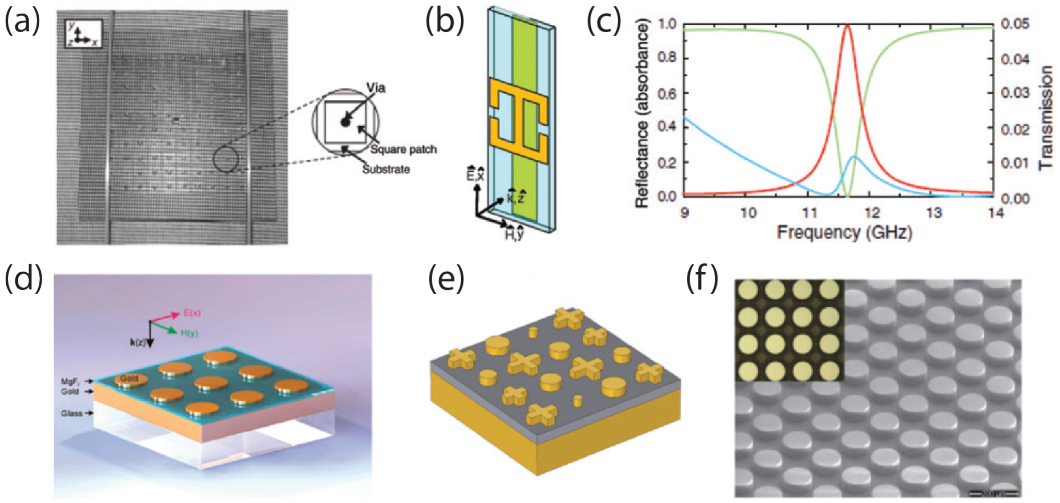

Figure 1.3. Conventional metasurface absorbers operating from microwave to optical frequencies (Source:[3]). (a) HIS based absorber. (b) The unit cell of perferct metamaterial absorber. (c) Simulated absorption of (b). (d) Infrared perfect absorber. (e) Wideband Solar absorber. (f) All-dielectric absorber working at THz range.

Metasurface also provides a platform for polarization conversion [5]. If the unit cell design is highly symmetrical, the polarization state is maintained. On the contrary, polarization conversion is achieved by isotropy breaking as shown in Figure 1.4. As anisotropy increases in the x and y direction, cross-polarized reflection rises. The reason is that the orthogonal electric components of incident field interacts with the surface differently if anisotropic.

1.2 Motivations

Conventional metasurfaces are limited by its static behaviour regardless of incident power, angle and frequency. They also subject to bandwidth limit of LTI systems and reciprocity theorem if non-magnetic. Electronic components loading can provide another degree of freedom to enable more promising functionalities and increasing application value.

Wideband absorption is a popular topic in metasurface absorbers to protect sensitive devices against broadband sources. However, the Bode-Fano criterion defines the trade-off between bandwidth and efficiency for all passive LTI systems. One possible solution is to break the underlying assumption of being LTI by adding nonlinear components and apply

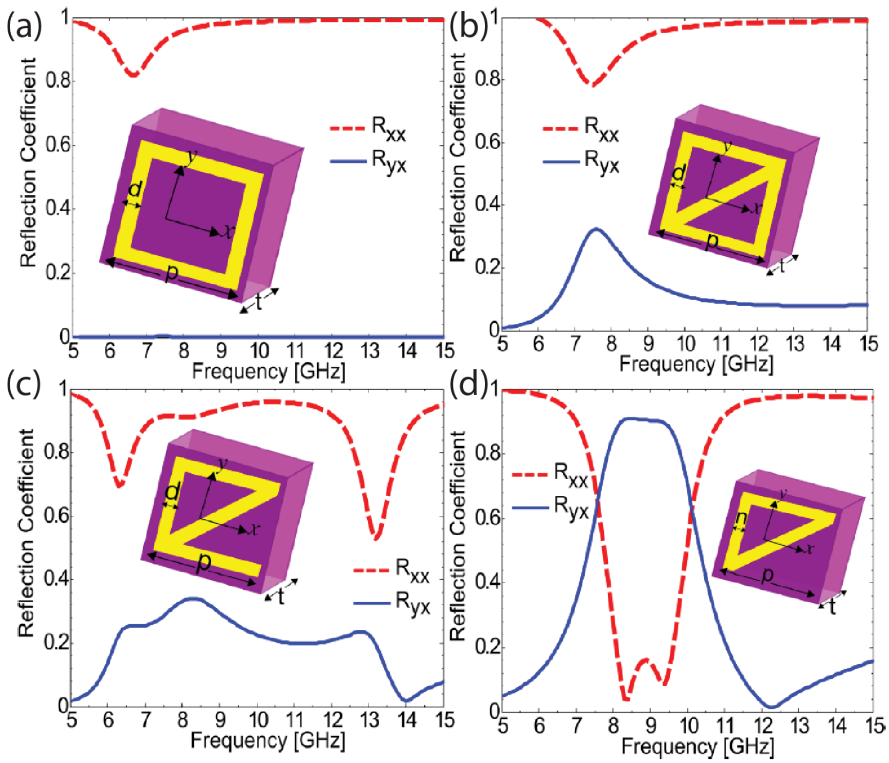

Figure 1.4. Example of anisotropic metasurface capable of polarization conversion (Source:[5]). Cross-polarized reflection is improved by breaking isotropy. (a) Square metallic ring. (b) Square ring with a diagonal strip. (c) One side of the square ring removed. (d) Two of the square sides removed.

time-modulation. In addition, LTI absorbers only have one working state, which means the communication signal dissipates as well as interference. By employing electronic components such as diodes could equip the surface with more working states. Thus, the surface could respond differently to varying incident power, angle, etc.

Breaking reciprocity in the microwave frequency range is strongly desirable in the development of modern electronic systems, as it enables nonreciprocal wave absorbing, nonreciprocal beam steering, frequency conversion, and protection of sensitive devices from high energy sources. However, non-magnetic LTI metasurfaces are subject to reciprocity theorem. Nonlinear metasurfaces provides an all-passive platform optimal configuration and efficient integration.

Conventional metasurface is capable of polarization conversion by adopting anisotropic unit cell. However, the polarization conversion is not optional. Reconfigurable metasurfaces may

address this issue by integrating nonlinear components or materials to increase the tunability, which further enhances the functionality and versatility of conventional metasurface.

1.3 Dissertation Organization

This thesis presents novel and unique approaches to achieve unconventional electromagnetic behaviour on metasurfaces by electronic loading, including breaking bandwidth limit, non-magnetic passive nonreciprocity, power-dependent transmission and malfunction realization.

Chapter 1 is an overview on the background of matasurfaces working mechanism, its applications and limitations, along with the motivation of introducing nonlinearity and time-modulation to improve the performance or overcome its limitations.

Chapter 2 presents the analysis, EM-circuit co-simulation and experimental results of a diodes-loaded cavity structure which overcomes the Bode-Fano limit by energy trapping using proper time-modulation strategy.

Chapter 3 investigates the a passive metasurface with different band structures dependent on the incident power level. The topology of the unit cell changes under high power illumination which triggers the diodes, transitioning from a surface wave supported structure to a bandgap structure.

Chapter 4 demonstrates the analysis, simulation and measurement results of an all-passive, non-magnetic, nonreciprocal microstrip line structure. Using the proposed microstrip line structure as a building block, a nonreciprocal metasurface is fabricated and measured.

Chapter 5 studies a varactor-based reconfigurable multifunctional metasurface. The unit cell is designed to naturally decompose the incident waves into orthogonal components. By adding tunable capacitance to the orthogonal fields, it performs simultaneous beam steering, polarization conversion and phase offset.

Chapter 6 summarizes and concludes the thesis, and addresses directions for further research.

Chapter 2

Broadband Time-modulated Absorber

Wide-band absorption has aroused attention in microwave engineering [6, 7, 8, 9, 10] during recent years to avoid damage from high energy and broadband microwave pulses [11]. Related research from metamaterials to nanostructures [12, 13] are conducted in attempt to provide absorption covering the range from microwave frequencies [14, 15] to infrared [16, 17] and Terahertz [18, 19]. Conventional methods focus on optimizing the balance between structure size and bandwidth by adopting passive multi-resonance structures [20, 12]. However, there is a physical limit between absorptance and bandwidth for any passive linear time-invariant(LTI) system, the Bode-Fano limit [21, 22, 23], which describes the trade-off between matching bandwidth and efficiency and is further proved to be applicable to antennas [24, 25], in another form, the Rozanov bound for absorbers [4], assuming the reflection coefficient to be a function of absorber thickness d and wavelength λ using the Fresnel law[26]. Fig.2.1(a) illustrates an example of a single-resonance absorber represented by a parallel *RLC* circuit with a broadband 3^{rd} order derivative Gaussian pulse input covering from DC to around 8 GHz, whose center frequency aligns with the resonating frequency of the *RLC* circuit. The absorptance on the load R_L is shown in Fig.2.1(c) when the matching network is either void or a 7^{th} order Chebyshev bandpass filter (details in 2.4.1). It can be observed that while absorptance approaches 1 around the center frequency when the Chebyshev filter is applied, the bandwidth is also compromised,

and as expected, the integral for both two curves fall below the Bode-Fano limit,

$$I(\omega_1, \omega_2) = \frac{R_L}{\pi L} \int_{\omega_1}^{\omega_2} \frac{1}{\omega^2} \ln \frac{1}{|\rho|} d\omega, \tag{2.1}$$

$$I(0, \infty) \leq 1, \tag{2.2}$$

where $\rho = \sqrt{1-A}$ is the reflection coefficient, in which the absorptance A is defined by the voltage across R_L by the input voltage $A = V_{R_L}^2 / V_{in}^2$ for $R_S = R_L$.

One possible solution to achieve beyond the Bode-Fano limit is to break its constraints of being a passive LTI system by introducing active devices, nonlinearity, or time-dependent elements, such as switches and diodes, etc. [27]. Non-foster components can break the passivity constraint by integrating amplifiers and other active elements, achieving ultra-wide band matching in contrast with conventional matching networks [28, 29, 30]. Additionally, research in direct antenna modulation (DAM) indicates that by applying time-modulation, transmitters can radiate beyond their original bandwidth [31, 32, 33]. Recent research on time-modulated absorbers for short pulses [34, 35] has developed analysis of absorbers with time-varying electromagnetic properties - the conductivity, permittivity, and permeability, and discuss a modulation strategy to go beyond the Rozanov bound. However, it is difficult to realize an absorber with varying dielectric characteristics in the real world, which hinders their applications.

In this chapter, we propose a more feasible temporal modulation approach that breaks the Bode-Fano limit, which instead of adopting hypothetical electrical material, employs only practical electric components - diodes/switches. The idea is to trap the incident ultra-wide band pulses within the resonator by adopting a modulated switch that cuts off the radiation path right after the signal fully enters the structure.

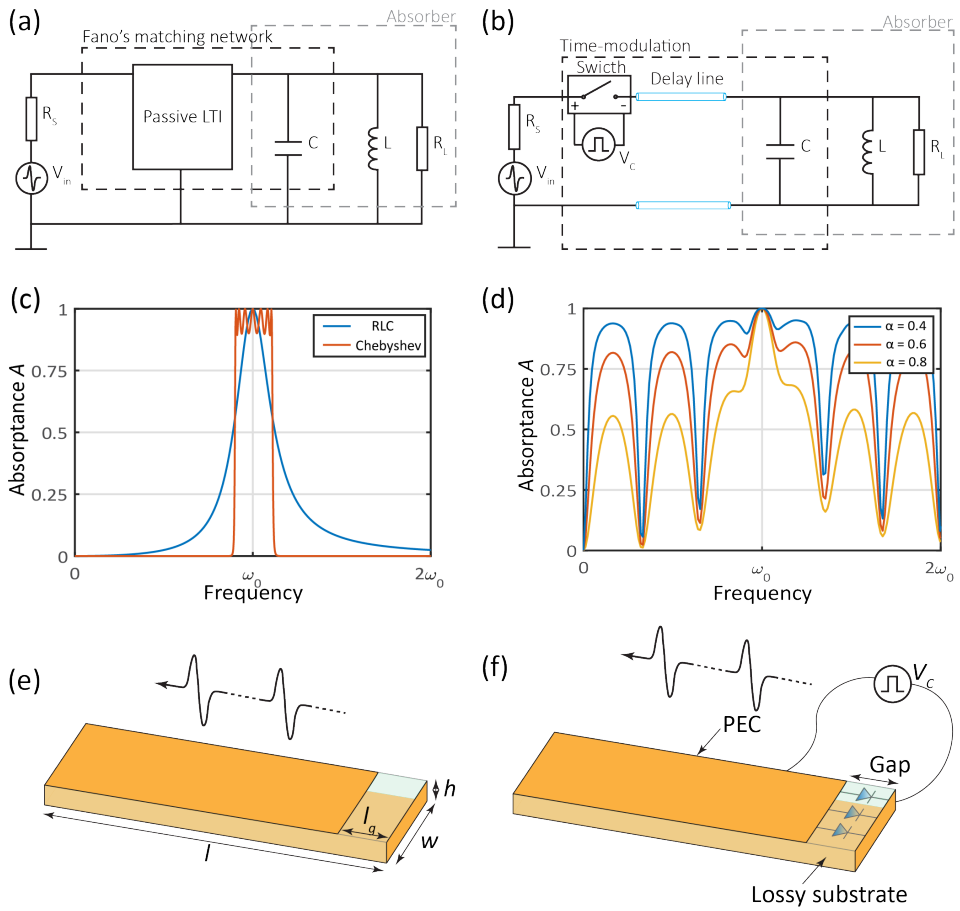

Figure 2.1. Circuit model: proof of concept. (a) Circuit representing a conventional single-resonance absorber, with $R_S = R_L = 653$ Ohms, $C = 0.5$ pF, $L = 3$ nH. (b) Circuit of the proposed time-modulated absorber. (c) Absorptance spectrum of (a) without matching and with a 7^{th} order Chebyshev bandpass filter, respectively, $\omega_0 = 1/\sqrt{LC}$. $I(0, 2\omega_0) = 0.977, 0.939$ for the RLC and the Chebyshev bandpass filter, respectively. (d) Absorptance spectrum of (b), with $t_d = 0.37$ ns through 15 reflections. (e) EM model of a conventional absorber being measured, with $h = 0.5$ cm, $w = 2.5$ cm, $l = 7$ cm, $l_g = 1$ cm. The substrate is FR4 with $\varepsilon_r = 4.8$. (f) EM model of the proposed time-modulated absorber being measured.

2.1 Analysis and Simulations

2.1.1 Analytical model

As a proof of concept illustrated in Fig.2.1(b), the switch, along with a delay line with a delay time of $t_d = t_p/2$, are inserted between the same Gaussian source and absorber as in Fig.(2.1)(a). The switch has a turn-on time of t_p, synchronized with the pulse, and is then left

OFF for the rest of the period, so that the input energy is allowed to only enter, but not to leave the network. The delay line ensures that the incoming pulse is inside the system before the switch turns OFF. As a result, the energy dissipates inside the network through multiple reflections. To obtain the transient voltage response on R_L, each reflection is treated separately using S parameters of a parallel *LC* circuit and is then summed up with its corresponding time shift.

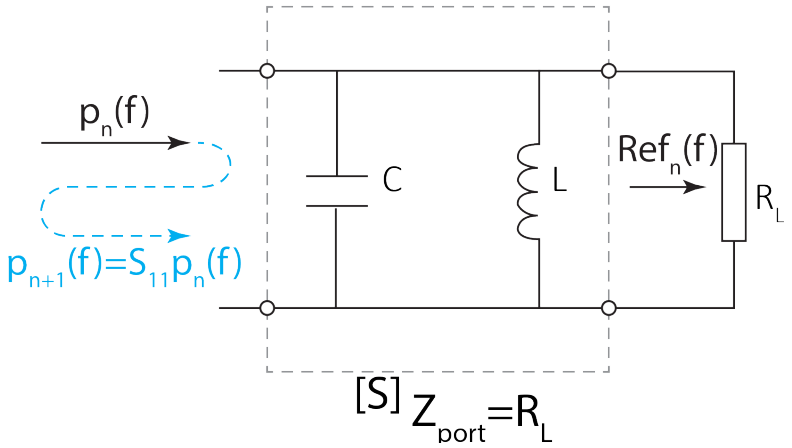

Figure 2.2. Analytical model: parallel LC circuit with load R_L.

The S parameters of a parallel *LC* circuit as shown in Fig.2.2, with the port impedance selected to be the same as the load R_L, are

$$S = \begin{pmatrix} \frac{-R_L(1-\omega^2 CL)}{2j\omega L+R_L(1-\omega^2 CL)} & \frac{2j\omega L}{R_L(1-\omega^2 CL)+2j\omega L} \\ \frac{2j\omega L}{R_L(1-\omega^2 CL)+2j\omega L} & \frac{-R_L(1-\omega^2 CL)}{2j\omega L+R_L(1-\omega^2 CL)} \end{pmatrix}. \tag{2.3}$$

$$Ref_{tot}(t) = \sum_{n=1}^{N} Ref_n(t-2nt_d), \tag{2.4}$$

$$Ref_n(t) = \mathscr{F}^{-1}\{S_{21}(f)\mathscr{F}\{p_n(t)\}\}, \tag{2.5}$$

$$p_n(t) = \mathscr{F}^{-1}\left\{(S_{11})^{n-1}\mathscr{F}\{p(t)\}(1-\alpha)^{n-1})\right\}, \tag{2.6}$$

where Ref_n represents the transient waveform in voltage on the load R_L during the n^{th} reflection neglecting the time delay, p_n is the input of the n^{th} reflection, S_{ij} is the S parameters of parallel *LC* network, and $p(t)$ is the original input from the broadband source. The derivation of Eqn.(2.4)

to Eqn.(2.6) are included in 2.4.2, and the transient waveform of the signals are depicted in 2.4.2 using Eqn.(2.4) to (2.6). We define the imperfection of the switch by a leakage factor $\alpha = E_{Trans.}/E_{Inc.}$. When $\alpha = 0$, all waves are trapped in the *RLC* circuit. Otherwise part of the incoming energy leaks out due to the imperfection of the switch. The non-modulated case can also be calculated with this model by setting $\alpha = 1$. Fig.2.1(d) shows the absorptance for a time-modulated absorber circuit model with different α. Note that the absorptance across the whole spectrum is 1, assuming an ideal switch with $\alpha = 0$ is used. Even with a highly imperfect switch, a drastic increase of bandwidth is observed in Fig.2.1(d) compared with (c), breaking the Bode-Fano limits even when the upper limit of the Bode-Fano integral is chosen to be a finite value such as $2\omega_0$: as an example, for $\alpha = 0.4$, $I(0, 2\omega_0) = 30.4$.

2.1.2 EM realization

The most straightforward way to realize the above circuit in an electromagetic structure is by adopting diode-integrated frequency selective surfaces (FSS) as the switch, and free space as the delay line (see 2.4.3). Thus, the ON and OFF states of the FSS corresponds to the ON and OFF states of the diodes. With the FSS in the OFF state, incident waves are allowed to propagate through; while in the ON state, the energy is trapped between the FSS and the conventional absorber. This method is rather general and can be applied to any passive absorber to broaden its bandwidth. However, the increased space needed conflicts with the objective of broadband absorption given a limited thickness. Thus, in this chapter, a more practical low-profile PCB realization is shown in Fig.2.1(e) and (f). A horizontally propagating incident pulse/pulse train is coupled to the structure through the gap on the top surface. the length of the structure performs equivalently as the delay line in the circuit model, and the switch is replaced by step recovery diodes (SRD) contolled by a signal V_C, which provides a Q-point for the diodes. When the control signal V_C is low, the diodes are OFF, and energy couples into the absorber; when V_C is high, the diodes turn ON, the absorber behaves as a closed cavity, and all the energy within is trapped inside. Instead of a lumped resistor R_L, the dissipation is distributive in the lossy FR4

substrate. The simulated results of the unit in static ON and OFF states are included in 2.4.4.

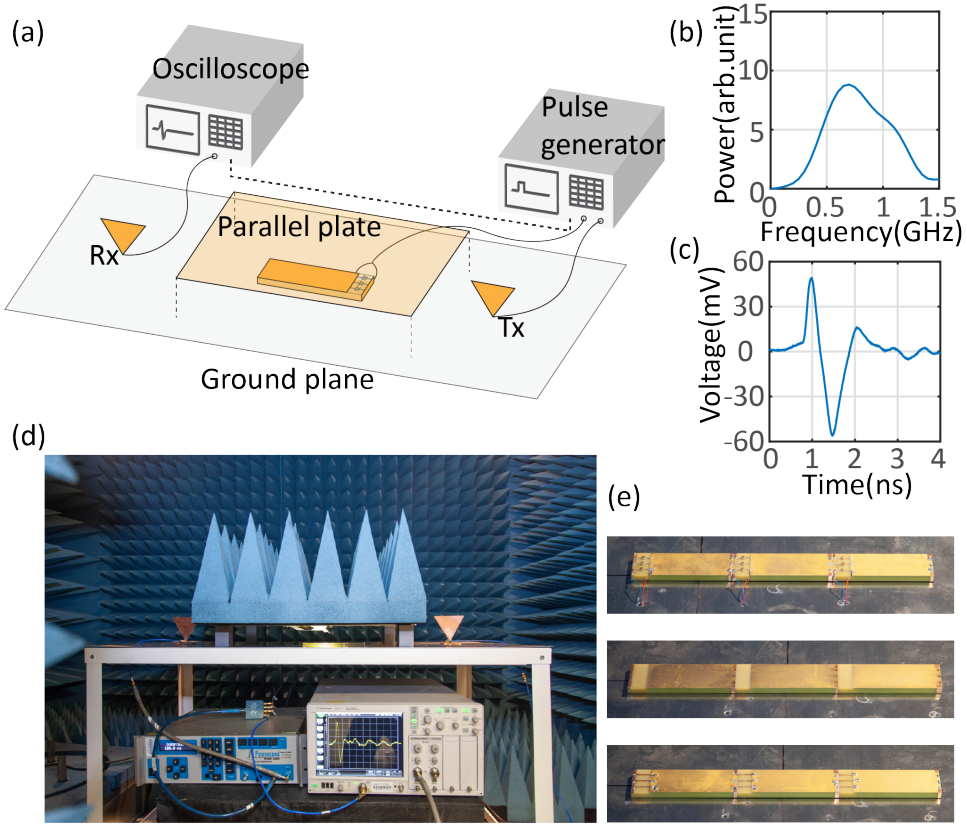

Figure 2.3. Measurement setup. (a) Measurement setup.(b) Measured spectrum of input signal from pulse generator using setup in (a), samples absent.(c) Measured transient waveform of input signal from pulse generator. (d) Picture of measurement setup in the anechoic chamber. (e) Measurement time-modulated, OFF state and ON state samples.

2.2 Measurement

The measurement sample is shown in Fig.2.3. The size of the structure is the same as shown in Fig.2.1(e) and (f), and the measurement setup is illustrated in Fig.2.3(a). The non-modulated sample with static ON and OFF states, and the time-modulated sample are measured, respectively, for one, two and three units. The signal is generated by a pulse generator and radiated by a broadband monopole bow-tie antenna Tx sitting on a 120 cm by 60 cm ground plane, travelling through a parallel plate 60 cm by 40 cm by 6 cm TEM waveguide (to confine energy) with the sample-under-test inside. The transmitted signal is received by another bow-tie

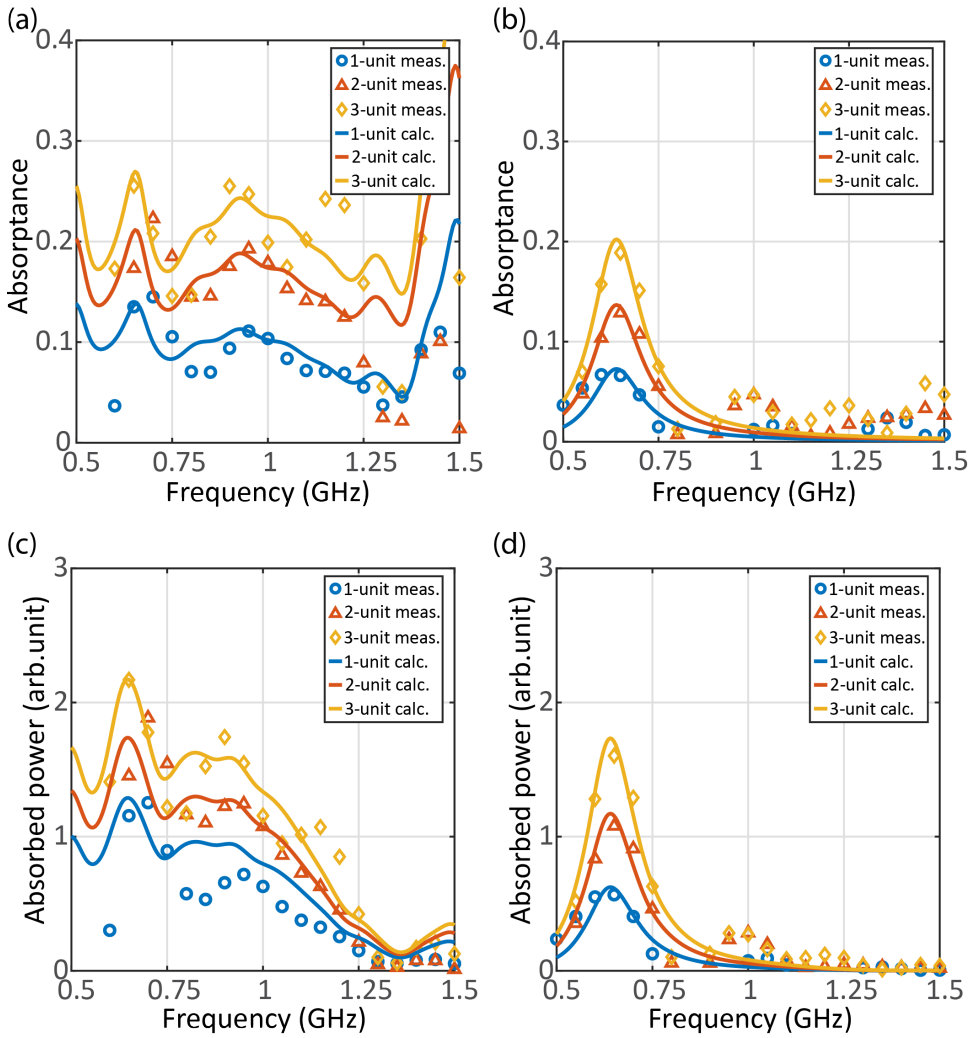

Figure 2.4. Measurement results. (a) Measured and calculated absorptance for time-modulated one-, two- and three-unit sample, respectively. r is assumed to be 0.27, 0.37, 0.47 in calculation for 1-,2-and 3-unit, respectively. $\alpha = 0.3$ for all calculations. (b) Measured and calculated absorptance for non-modulated one-, two- and three-unit sample, respectively. (c) Measured and calculated absorbed power for time-modulated one-, two- and three-unit sample, respectively. (d) Measured and calculated absorbed power for non-modulated one-, two- and three-unit sample, respectively.

antenna Rx and collected by a wide-band oscilloscope. The produced signal from the pulse generator is a 5 V repetitive pulse train lasting 100 ps with low duty cycle of 0.001% and a rise time around 70 ps. This signal is transformed from a unipolar pulse to a 3^{rd} order derivative Gaussian-like pulse by Tx, collected by Rx. The spectrum and transient waveform is shown in Fig.2.3(b) and (c). The distance between Tx and Rx is 90 cm. The osilloscope and the pulse

generator are synchronized with the trigger signal of the latter, and part of the trigger signal is split out by a power divider to be used as the control signal for the time-modulated absorber. The trigger signal lasts for 40 ns, which warrants adequate multi-reflection for sufficient dissipation. Short twisted pair wires with different lengths are adopted and tuned to precisely control the time delay between different units for multi-unit measurements when travelling wave modulation is performed. All the cables involved in this experiment are carefully chosen, such that the modulated signal synchronizes with the incident wave for the samples to trap as much energy as possible. For each configuration, the average of five sets of measurements is adopted to reduce noise and avoid fluctuations. 2.4.5 includes more details on measurements such as antenna design, pulse train waveform and twisted pair wires design.

From an analytical perspective, the R_L, L, C and R_S required for S parameter calculation in (2.6) can be extracted from non-modulated measurement results in Fig.2.4(b) by

$$L = \frac{1}{2\pi}\frac{\Delta f}{f_0^2}R_L, \tag{2.7}$$

$$C = \frac{1}{2\pi R_L}\Delta f, \tag{2.8}$$

where $f_0 = 640$ MHz is the center frequency, $\Delta f = 80$ MHz is the 3 dB bandwidth. By plugging (2.7) and (2.8) into (2.3), the S parameters for the parallel LC network become

$$S = \begin{pmatrix} \frac{\omega^2 - 4\pi f_0}{j4\pi\omega\Delta f - (\omega^2 - 4\pi^2 f_0)} & \frac{j4\pi\omega\Delta f}{j4\pi\omega\Delta f + (4\pi^2 f_0 - \omega^2)} \\ \frac{j4\pi\omega\Delta f}{j4\pi\omega\Delta f + (4\pi^2 f_0 - \omega^2)} & \frac{\omega^2 - 4\pi f_0}{j4\pi\omega\Delta f - (\omega^2 - 4\pi^2 f_0)} \end{pmatrix}, \tag{2.9}$$

which only depend on Δf and f_0 and are independent of R_L.

Different from the circuit model in Fig.2.1(b), only a portion of radiation from Tx couples into the sample in the measurement. Therefore, a parameter r is introduced to describe how

much energy is captured by the units and Eq.(2.6) accordingly changes to

$$p_n(t) = r\mathscr{F}^{-1}\left\{(S_{11})^{n-1}\mathscr{F}\{p(t)\}(1-\alpha)^{n-1})\right\}, \tag{2.10}$$

where $p(t)$ is assigned with the measured input pulse in FIG.2.3(c). Moreover, since the loss is distributive, instead of evaluating the absorption by calculating the dissipation on R_L, the absorptance A and absorbed power P are calculated with respect to transmission $Tran$ instead of absorption Ref_{tot} on the load by

$$A_{cal.}(f) = \frac{|\mathscr{F}\{p(t)\}|^2 - |\mathscr{F}\{Tran_{tot}(t)\}|^2}{|\mathscr{F}\{p(t)\}|^2}, \tag{2.11}$$

$$P_{cal.}(f) \propto |\mathscr{F}\{p(t)\}|^2 - |\mathscr{F}\{Tran_{tot}(t)\}|^2, \tag{2.12}$$

in which,

$$Tran_{tot}(t) = \sum_{n=1}^{N} Tran_n(t - 2nt_d), \tag{2.13}$$

corresponds to the transient transmission received by Rx and collected by the oscilloscope, and

$$Tran_n(t) = \alpha\mathscr{F}^{-1}\{\mathscr{F}\{S_{11}p_n(t)\}\}. \tag{2.14}$$

For the measurement results, to exclude the disturbance of fields by the samples and the reflection, the baseline is the ON state (replacing diodes with wires) instead of an empty waveguide.

$$A_{meas.}(f) = \frac{|\mathscr{F}\{Tran_{ON}(t)\}|^2 - \left|\mathscr{F}\{Tran_{TM/OFF}(t)\}\right|^2}{|\mathscr{F}\{Tran_{ON}(t)\}|^2}, \tag{2.15}$$

$$P_{meas.}(f) \propto |\mathscr{F}\{Tran_{ON}(t)\}|^2 - \left|\mathscr{F}\{Tran_{TM/OFF}(t)\}\right|^2, \tag{2.16}$$

where $Tran_{ON/OFF/TM}$ denotes transmitted signal measured with ON state, OFF state and time-modulated sample collected by the oscilloscope.

The measured and calculated absorptance is shown in Fig.2.4. As shown in Fig.2.4(b), the non-modulated sample absorbs energy at around the resonating frequency 0.64 GHz, while the modulated sample has a broadband absorption starting from 0.6 GHz to 1.5 GHz. Due to difficulty in directly determining α and r through measurement, these two parameters are numerically fitted. It is found that when $\alpha = 0.3$ (indicating 9 % of the coupled energy leaks out when the diodes are ON) and $r = 0.27,\ 0.37,\ 0.47$ for one-,two- and three-unit calculations, the predicted results show a good match with the measurement results in Fig.2.4. The calculated Bode-Fano integral $I(0.6\ GHz, 1.5\ GHz) = 5.81$ and 0.95 for single-unit modulated and non-modulated sample, respectively, $\rho_{meas.} = \sqrt{1 - A_{meas.}(f)}$. Since the incident wave propagates horizontally, increasing the number of the unit is equivalent to enlarging the thickness of an absorber under normal incidence, and thus the absorption rate increases for both modulated and non-modulated cases, indicating the potential to accommodate this design to larger-scale metasurfaces.

2.3 Conclusion

In this chapter, we proposed an approach for short pulses to break the Bode-Fano limit using time-modulation by creating an energy trap and discussed two possible EM structures based on the idea. Verified by analytical calculations, simulation results and measurement of the horizontal model, we proved the proposed method can achieve beyond the bandwidth limitations for passive LTI systems. The latter low-profile design integrates well with PCB and can be potentially applied to protect sensitive devices against broadband signals. Although measurements are done only for up to three units, the horizontal design could be extended to a metasurface. We would like to point out that the form factor of this design is related to the pulse width, and as a result the bandwidth of the pulse has a lower limit to warrant the unit to be sub-wavelength (in terms of center frequency). For our particular model, the fractional bandwidth need to be higher than 33.7% (details in 2.4.6), which is loose for a broadband pulse.

Time-modulation also brings other interesting properties, such as non-reciprocity [36, 37, 38]. The horizontal model we propose also has non-reciprocal behaviour caused by the temporal modulation and is discussed in 2.4.4. Further research may focus on self-triggering and self-delaying modules to automatically align the phase of the incident pulse and the control signal.

2.4 Extended Material

2.4.1 Chebyshev bandpass filter design

The circuit design of the 7^{th} order Chebyshev bandpass filter is shown in Fig.2.5, with the last section being the parallel *RLC* resonator with $R = 643$ Ohms, $L = 3$ nH and $C = 0.5$ pF. Element values for a 7^{th} 0.5 dB equal ripple Chebyshev filter are $g_1 = g_7 = 1.7372$, $g_2 = g_6 =$

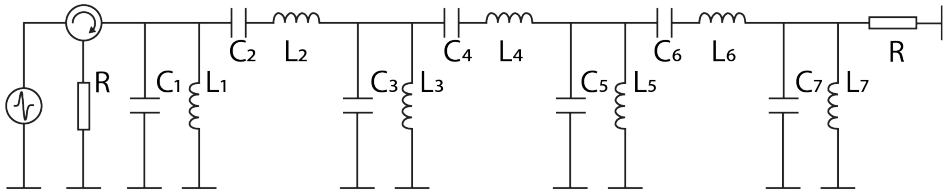

Figure 2.5. Circuit design of a 7^{th} order Chebyshev bandpass filter.

1.2583, $g_3 = g_5 = 2.6381$, $g_4 = 1.3444$. The last section is fixed to be a parallel *LC* circuit with $L_7 = 3$ nH and $C_7 = 0.5$ pF, and

$$L_1 = L_7 = \frac{R\Delta}{g_7\omega_0}, C_7 = C_1 = \frac{g_7}{R\omega_0\Delta},$$

where R=653 Ohms, $\omega_0 = \sqrt{\frac{1}{L_7C_7}}$. We derive $\Delta = 0.20607$, and therefore obtain

$$L_6 = L_2 = \frac{Rg_6}{\omega_0\Delta} = 154.43\ nH,$$
$$C_6 = C_2 = \frac{\Delta}{g_6R\omega_0} = 0.000971\ pF,$$

$$L_5 = L_3 = \frac{R\Delta}{g_5\omega_0} = 1.976\,nH,$$
$$C_5 = C_3 = \frac{g_5}{R\omega_0\Delta} = 0.759\,pF,$$

$$L_4 = \frac{Rg_4}{\omega_0\Delta} = 165\,nH,$$
$$C_4 = \frac{\Delta}{g_4 R\omega_0} = 0.00909\,pF.$$

2.4.2 Analytical derivation

Fig.2.6 shows the calculated S parameters using measured Δf and f_0. For steady state,

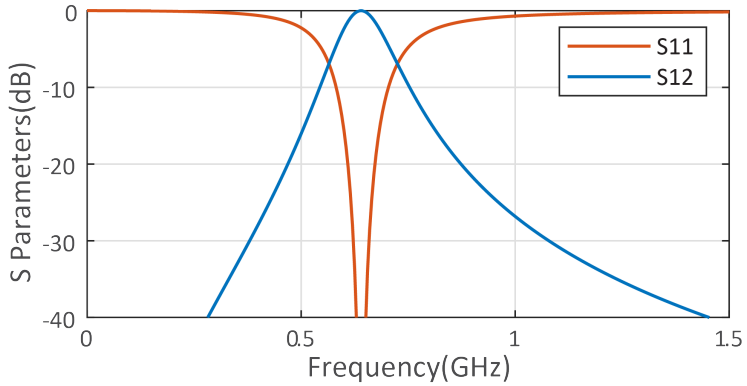

Figure 2.6. Calculated S parameters using measured Δf and f_0.

the response on the load Ref_{steady} can be derived by multiplication of the input signal $p(f)$ and the transmission S_{21},

$$Ref_{steady}(t) = \mathscr{F}^{-1}\{\mathscr{F}\{p(t)\}S_{21}\}.$$

For the time-modulated case, assuming the switches are ideal, the input p_n of the n^{th} reflection can be seen as the reflected signal during the $(n-1)^{th}$ reflection, determined by S_{11} of the

network,

$$
\begin{aligned}
p_1(t) &= p(t),\\
p_2(t) &= \mathscr{F}^{-1}\{S_{11}\mathscr{F}\{p_1(t)\}\},\\
p_3(t) &= \mathscr{F}^{-1}\{S_{11}\mathscr{F}\{p_2(t)\}\},\\
&\vdots\\
p_n(t) &= \mathscr{F}^{-1}\{S_{11}\mathscr{F}\{p_{n-1}(t)\}\} = \mathscr{F}^{-1}\{S_{11}^{n-1}\mathscr{F}\{p_1(t)\}\}.
\end{aligned}
$$

The transient waveform on the load is derived by multiplication of the input signal p_n and transmission of the network S_21,

$$
\begin{aligned}
Ref_1(t) &= \mathscr{F}^{-1}\{S_{21}\mathscr{F}\{p_1(t)\}\},\\
Ref_2(t) &= \mathscr{F}^{-1}\{S_{21}\mathscr{F}\{p_2(t)\}\},\\
Ref_3(t) &= \mathscr{F}^{-1}\{S_{21}\mathscr{F}\{p_3(t)\}\},\\
&\vdots\\
Ref_n(t) &= \mathscr{F}^{-1}\{S_{21}\mathscr{F}\{p_n(t)\}\}.
\end{aligned}
$$

Now adding the corresponding time delay to each R_n, for each reflection there is a $2t_d$ delay for going forward and backward on the delay line,

$$\Gamma_1'(t) = \Gamma_1(t - 2t_d),$$
$$\Gamma_2'(t) = \Gamma_2(t - 4t_d),$$
$$\Gamma_3'(t) = \Gamma_3(t - 6t_d),$$
$$\vdots$$
$$\Gamma_n'(t) = \Gamma_n(t - 2nt_d).$$

We then derive

$$\Gamma_{tot} = \sum_{n=1}^{N} \Gamma_n(t - 2nt_d).$$

If the switch is not ideal, a leakage factor $\alpha = \frac{E_{Trans}}{E_{inc}}$ is introduced. It only affects the input of the n^{th} reflection when $n > 1$, and $p_n(t)$ changes to

$$p_1(t) = p(t),$$
$$p_2(t) = \mathscr{F}^{-1}\{S_{11}\mathscr{F}\{p_1(t)\}(1-\alpha)\},$$
$$p_3(t) = \mathscr{F}^{-1}\{S_{11}\mathscr{F}\{p_2(t)\}(1-\alpha)\},$$
$$\vdots$$
$$p_n(t) = \mathscr{F}^{-1}\{S_{11}\mathscr{F}\{p_{n-1}(t)\}(1-\alpha)\}$$
$$= \mathscr{F}^{-1}\{S_{11}^{n-1}\mathscr{F}\{p_1(t)\}(1-\alpha)^{n-1}\}.$$

For measurements, since only a part of the incident wave couples into the structure, a factor r is introduced to describe how much is captured by the sample. It only affects the first input $p_1(t)$,

$$p_1(t) = rp(t),$$

Therefore $p_n(t)$ changes to

$$p_n(t) = \mathscr{F}^{-1}\{S_{11}\mathscr{F}\{p_{n-1}(t)\}\} = r\mathscr{F}^{-1}\{S_{11}^{n-1}\mathscr{F}\{p(t)\}\}.$$

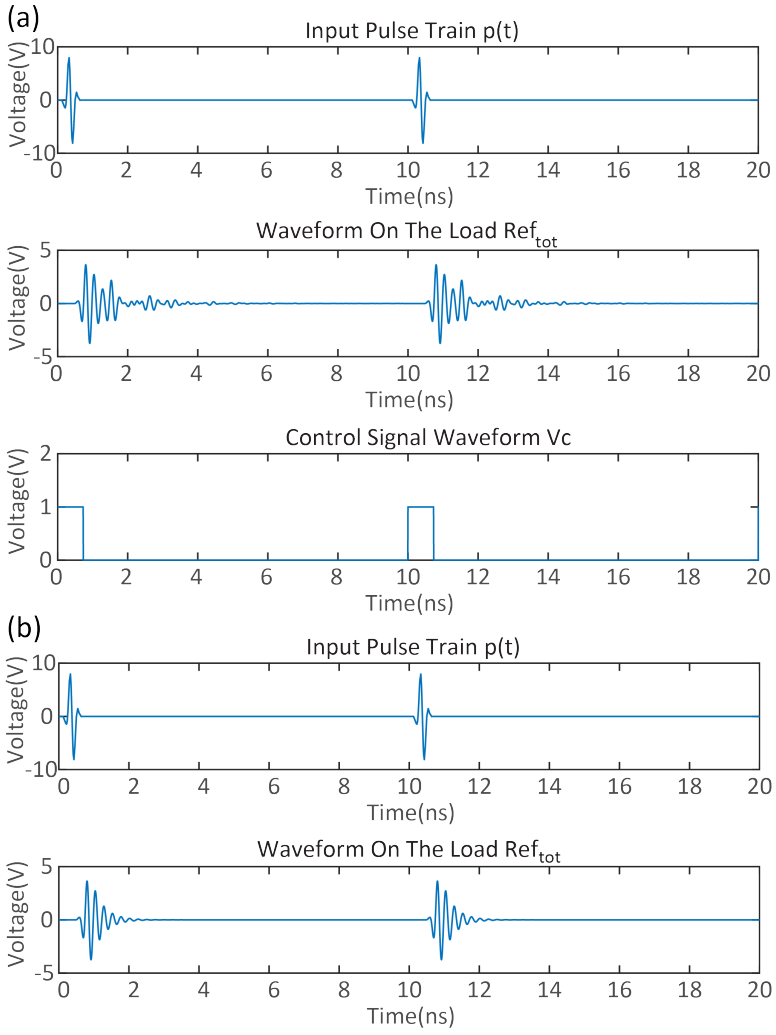

Figure 2.7. Transient waveform of signals in the system. (a) Time-modulated case with $\alpha = 0.2$. (b) Non-modulated case using $\alpha = 1$.

Using the equations derived above, the signals in the circuit model are plotted in Fig.2.7 for two periods. Fig.2.8 shows the Bode-Fano limit integral I as a function of delay time t_d assuming the length of the units l is infinity. I first rises as t_d increases, since the amount of trapped energy increases. After $t_d = t_p/2$, all the waves are trapped inside, thus I stops rising.

$t_d = t_p/2$ is the optimal value when designing an EM realization, since it requires the minimum size.

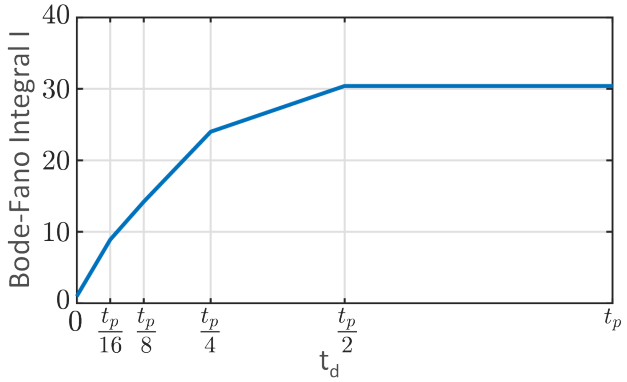

Figure 2.8. The Bode-Fano limit integral *I*.

2.4.3 Vertical model

The vertical model is a straight translation of the circuit model. A diode-integrated frequency selective surface (FSS) is used as the counterpart of the ideal switches in the circuit. The simulated ON and OFF state transmission characteristics using HFSS are shown in Fig.2.9.

Incident waves below 8 GHz can easily pass through the FSS, while they are blocked when the FSS is ON. Diodes are later connected at the gaps of the OFF state, so the state of the FSS is dependent on the state of the diodes.

This approach is more general, and can be applied to any absorber to broaden its bandwidth by adding a modulated FSS above it. Here we use a conventional ring absorber as an example shown in Fig.2.10. The absorber is connected with a capacitor indicated by the red square to shrink the electrical size in (b). A resistor is connected in circuit simulation to absorb incident energy, indicated by the red square, and is assigned with a lumped port in EM simulation. The properties are studied by conducting EM-circuit co-simulations in HFSS, and the results are shown in Fig.2.10. By adopting a temporally modulated FSS, the bandwidth of the absorber largely increases.

The ring absorber can be represented by a parallel *RLC* circuit, and the values are

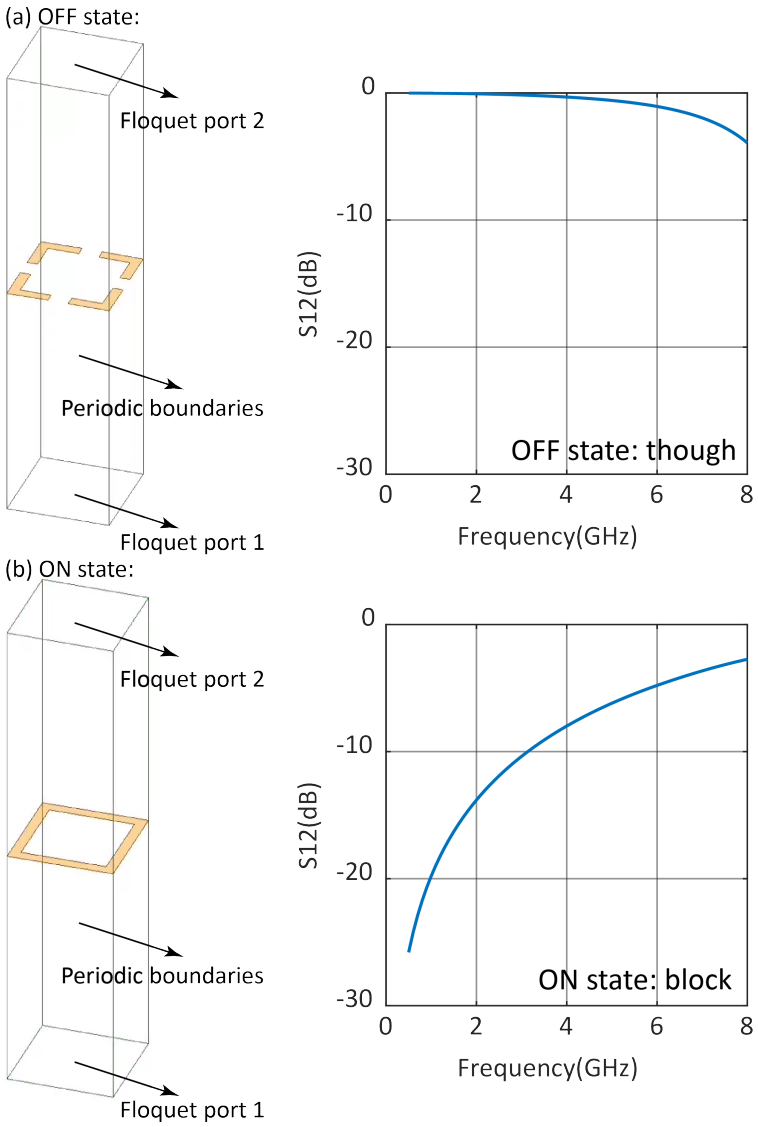

Figure 2.9. The static states of the vertical model. (a) The OFF state of the FSS, and its transmission characteristics simulated in HFSS. (b) The ON state of the FSS, and its transmission characteristics simulated in HFSS.

extracted by fitting the Z parameters of the lumped port, as shown in Fig.2.11 using $R = 653$ Ohms, $L = 3$ nH and $C = 0.5$ pF. Note that these values are the same as the values used in Fig2.1. It is shown that the simulation results in Fig.2.10 matches well with the results derived from the analytical model shown in Fig.2.1, assuming $\alpha = 0.2$ since the FSS is not ideal.

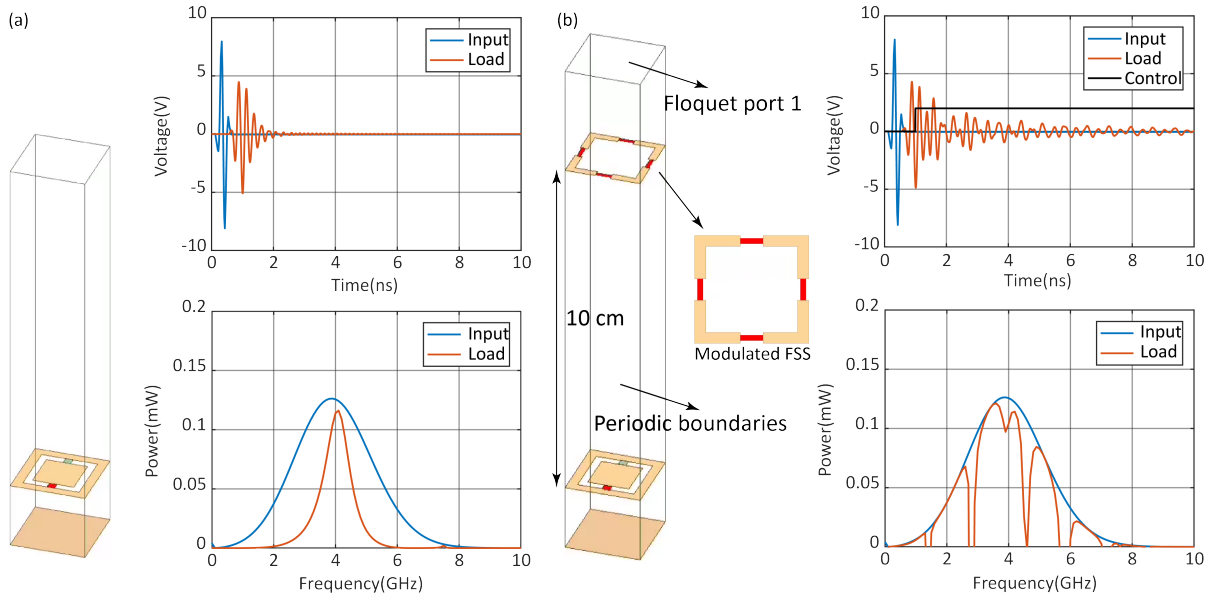

Figure 2.10. EM-co simulation results. Comparison between non-modulated and modulated vertical model simulated in HFSS. (a) Non-modulated ring absorber and its transient waveform and spectrum on the resistor. (b) Modulated ring absorber and its transient waveform and spectrum on the resistor.

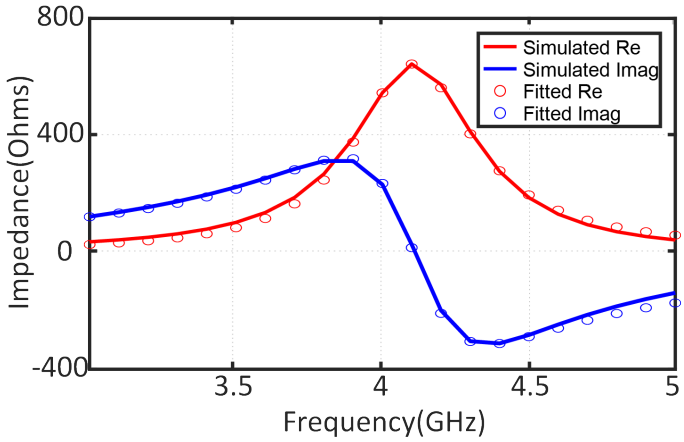

Figure 2.11. The simulated and fitted impedance of the lumped port. $R = 653$ Ohms, $L = 3$ nH and $C = 0.5$ pF.

2.4.4 Horizontal model

The steady states (ON and OFF) are simulated in HFSS and the results are shown in Fig.2.12. The absorption is calculated by

$$Absorption = 1 - S_{11}^2 - S_{12}^2,$$

where S_{11} and S_{12} are the S parameters of one of the wave ports. The OFF state shows high absorption around 0.62 GHz while the ON state behaves as a closed cavity. Fig.2.13 shows the

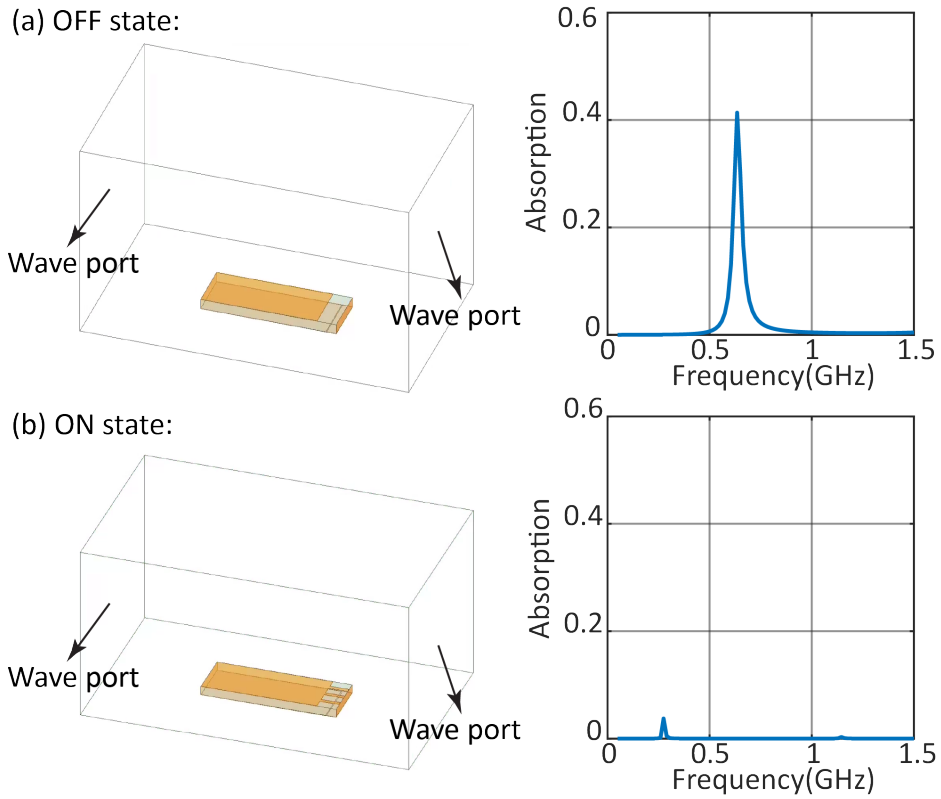

Figure 2.12. The EM model and its absorption. (a) ON state and (b) OFF state, respectively. A single unit is placed inside a TEM waveguide, whose top and bottom surface are assigned with PEC, front and back surface are PMC.

absorption when different number of units are employed for the modulated and non-modulated case in a 2.5 cm tall TEM waveguide. Since the incident wave propagates horizontally, as the number of units increases, the absorption rate increases. Another interesting property that time-modulation brings is non-reciprocity. When no modulation is applied, the structure is reciprocal. When waves are travelling from the right, more energy couples into the unit compared with left side incidence. After one reflection, more reflects to the source. Although less energy couples into the unit when coming from the left, less reflects to the source. Therefore, the structure shows reciprocity. However, after applying time-modulation, the absorption/reflection is only related to the first coupling into the units. Therefore, right hand side incidence shows a higher absorption

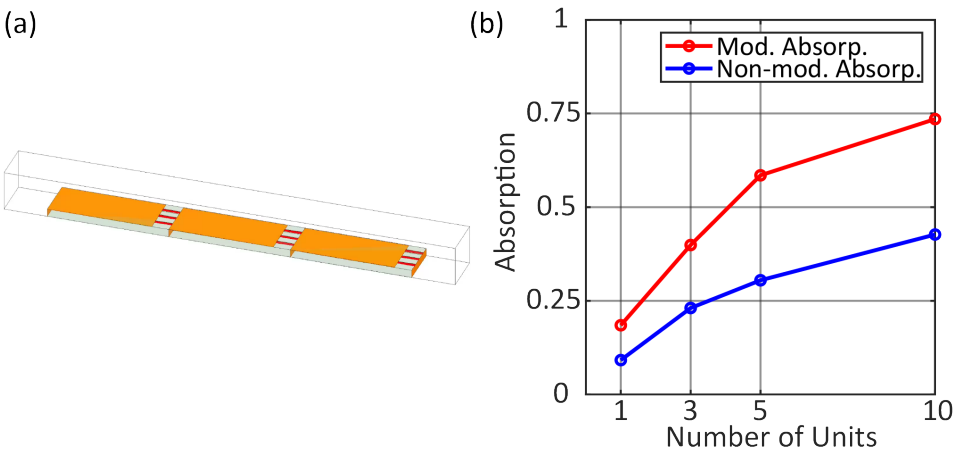

Figure 2.13. EM-circuit co-simulations in a 2.5 **cm by** 2.5 **cm by** 26 **cm TEM waveguide.** (a) Three-unit EM simulation model. (b) Absorption of the modulated and non-modulated model with different number of units.

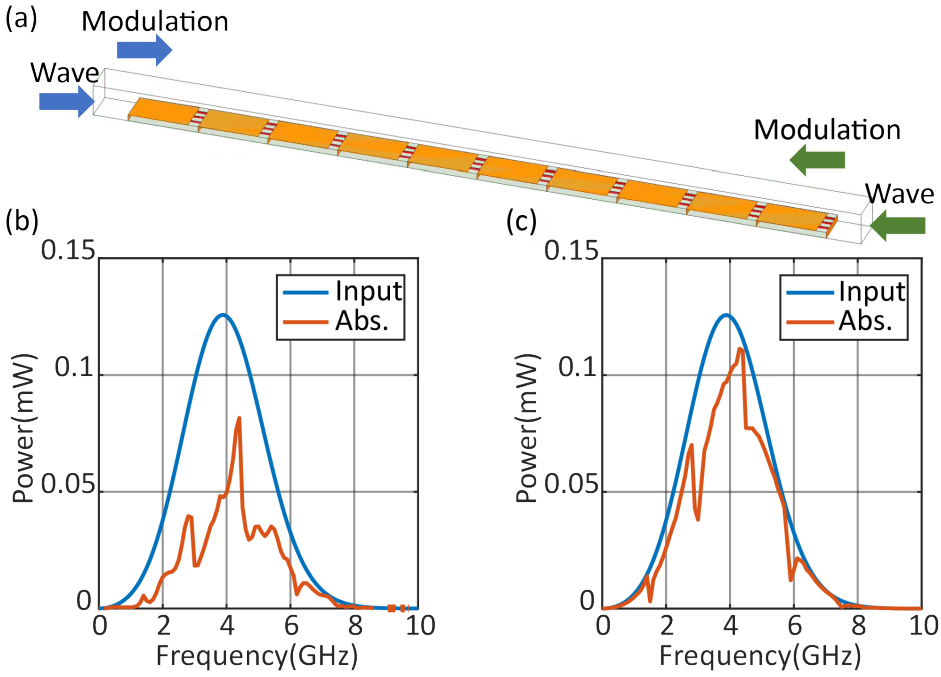

Figure 2.14. Non-reciprocity brought by time-modulation. (a) Ten-unit EM model. (b) Absorbed power when wave and modulation travelling from left to right. (c) Absorbed power when wave and modulation travelling from right to left.

compared with left hand side incidence as shown in Fig.2.14. This method could be applied to other asymmetrical structures to create non-reciprocity.

2.4.5 Equipment

The equipment involved in the measurement are: wide-band oscilloscope 86100*D* Infiniium DCA-X, picosecond pulse generator 10060*A*, and 4 way power divider Narda 4321$C-4$. The step recovery diodes are $GC2510-17$, whose threshold voltage is $V_{th} = 0.78$ V and series resistance is $R_s = 1.2$ Ohms, modulated by $V_c = 1.2$ V. The power absorbed by the diodes in the ON state can be estimated by $\frac{(V_c - V_{th})^2}{R_s} = 0.15$ W. This power is nearly independent of the dissipated RF signal strength on the load, considering working at Q-point, and it is mainly dependent on the bias V_c and properties of the diode. The E-field strength across the gap that is strong enough to change the bias condition of the diode is around $\frac{V_c - V_{th}}{l_g} = \frac{1.2\,V - 0.78\,V}{0.01\,m} m = 42$ V/m. It is reasonable to assume that the E-field is much smaller than this, thus no isolation circuit is needed for the biasing system. Fig.2.15 illustrates the waveform of the generated pulse from the pulse generator before it is radiated by Tx. The two bow-tie antennas involved

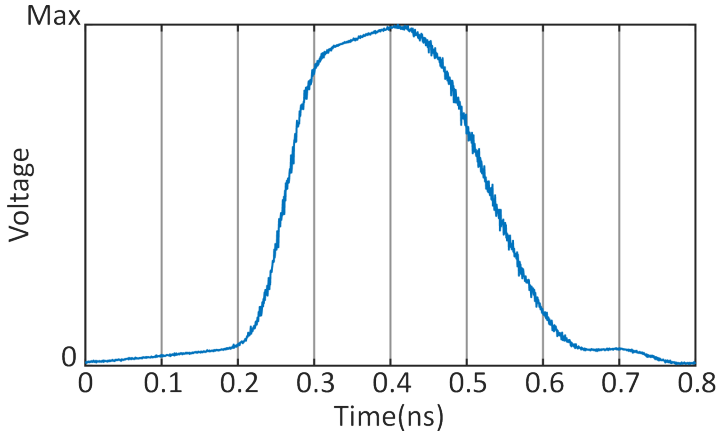

Figure 2.15. Generated pulse waveform Waveform of a pulse generated from the pulse generator (picosecond pulse generator 10060*A*), with the pulse width set to be 100 ps on the front panel.

in the measurement are made of 0.062" thick Rogers Duorid 5880 sitting on a small ground plane (5.01 cm by 5.74 cm) as shown in Fig.2.16. One of the three twisted lines is shown in Fig.2.17. There are three twisted lines involved in the measurement and they differ in length to realize a travelling wave modulation. The first unit (the one closest to Rx) is modulated

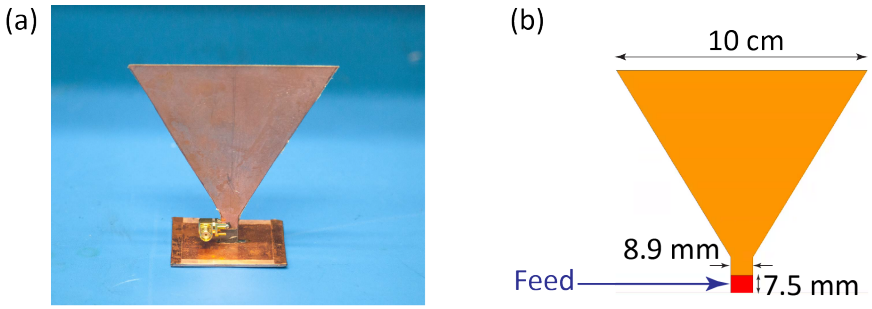

Figure 2.16. The bow-tie antenna used as the Tx and Rx. (a) A picture of the monopole bow-tie antenna. (b) Sizes of the antenna.

by the shortest twisted lines $l_1 = 33.0$ cm, the second unit is modulated by $l_2 = 38.5$ cm and $l_3 = 44.0$ cm. It is the difference in length Δl between each two adjacent lines that matters, not the length of lines. Since the length of the units is 7 cm, the time delay between each twisted line should be $\Delta t = (7\ cm)/(3 \times 10^8\ m/s) = 0.233$ ns. We are using 30 AWG by OK industries, the corresponding Δl to $\Delta t = 0.233$ ns is 5.55 cm. To determine Δl, we first measure the propagation speed v inside the lines using a pulse generator and an oscilloscope, then calculate Δl by $\Delta l = v\Delta t$, and lastly confirm the value of Δl by measuring delay time between two twisted lines with a Δl difference in length. Note that Δl might be different if using different wires.

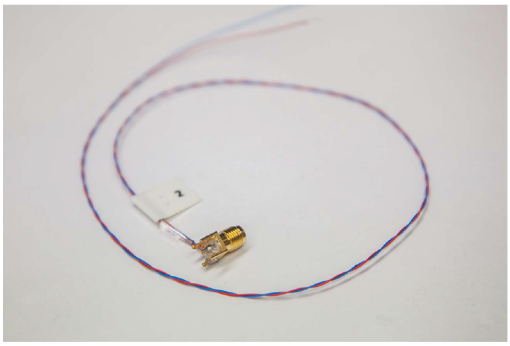

Figure 2.17. A picture of the twisted pairs involved in time-modulation.

2.4.6 Bandwidth limitation

In this section, we calculate the minimum bandwidth requirement to warrant a sub-wavelength unit design by examining the spectrum of an N^{th} order Gaussian derivative pulse.

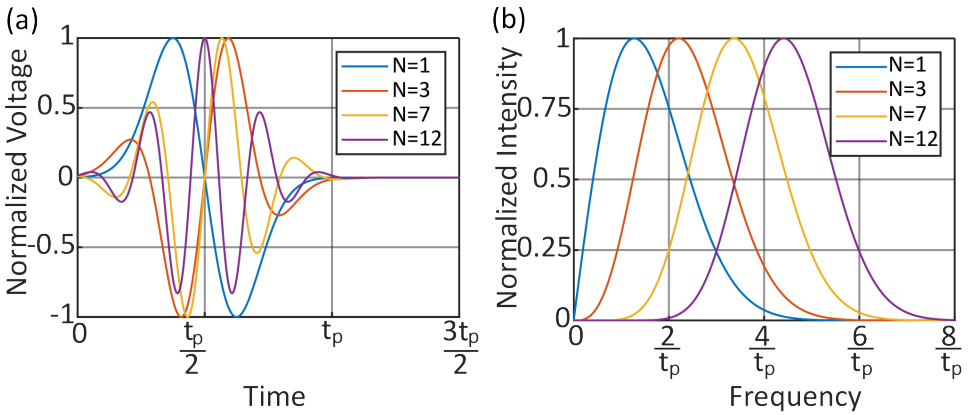

Figure 2.18. N^{th} **order Gaussian derivative pulse.** (a) Transient waveform. (b) Spectrum.

Fig.2.18 lists different order of Gaussian derivative pulse lasting t_p. The sub-wavelength requirement (in terms of center frequency) can be expressed by

$$\lambda_0 > l = \frac{t_p}{2\sqrt{\varepsilon_r}}c.$$

This yields

$$f_0 = \frac{c}{\lambda_0} < \frac{c}{l} = \frac{2\sqrt{\varepsilon_r}}{t_p}.$$

For our particular model, $\varepsilon_r = 4.8$, $f_0 < \frac{4.4}{t_p}$. This approximately corresponds to the $N = 12$ case, which has a -3 dB fractional bandwidth of 33.7 %.

This chapter is based on the following paper: Yang, X., Wen, E., & Sievenpiper, D. F. (2022). "Broadband time-modulated absorber beyond the Bode-Fano limit for short pulses by energy trapping." *Physical Review Applied*, 17(4), 044003. The dissertation author was the primary investigator and author of this paper.

Chapter 3

Power-dependent Transmission

The development of microwave technology [6, 7] in electronic devices and communication systems has brought much convenience to daily life. However, such low-power and sensitive systems can be easily interfered, or even damaged, by the complex electromagnetic environment or by external microwave sources. The incident waves can induce currents, which also radiate into the shielding, around any gaps in a metallic enclosure, even if the openings are electrically small.

Microwave absorbers are used to protect devices from incoming signals by absorbing the energy. Conventional approaches [39, 40] such as Salisbury screen [41] apply lossy coatings, which are usually bulky and expensive, to the surface of the metallic enclosure to dissipate the power. Recent research on metasurfaces offer another solution[2, 42, 43]. These low-profile, low-cost, sub-wavelength, PCB-based, periodic metallic structures can be engineered to various frequency ranges with adequate performance.

Although these approaches could reduce the transmission through gaps and openings, such linear absorption behaviour of conventional absorbers can also impair the performance of the protected device itself, especially for low-power communication systems. Nonlinear [44], switchable [45, 46, 47] and tunable [48, 49, 50] metasurface absorbers have arisen attention in recent years. By integrating with lumped elements, diodes, switches, and transistors, the absorbers work in different states dependent on the power level [51, 47] or the waveform [52] of

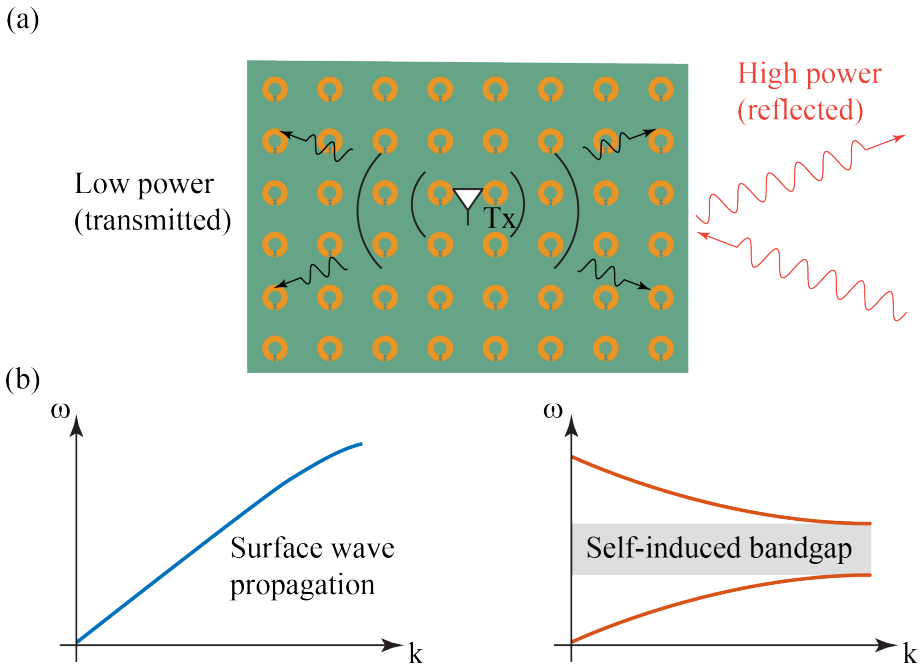

Figure 3.1. Concept illustration. (a) Nonlinear metasurface behaviour. (b) Band structure with low (left) and high (right) illumination.

the incoming signals due to the nonlinearity provided by the elements. However, these structures are usually complex and some require control circuits.

In this chapter, we propose a self-induced, diode-integrated, power-dependent metasurface which changes the topology of its surface wave band structure to create a self-induced bandgap with high power illumination as shown in Fig. 3.1. Thus, this nonlinear surface reflects the incoming wave rather than absorbing it within the bandgap region. Unlike the previous study [47], rather than shifting the band up and down to change the surface impedance, and thus change the absorption rate, we directly manipulate the band structure to open a bandgap which prevents propagation of surface waves.

3.1 Structure Design and Simulation Results

3.1.1 Static Unit Cell Design

The unit cell is designed to transition between two states (the ON and OFF states) based on the incident power: the low power state (the OFF state) as shown in Fig.3.2 (a) and the high power state (the ON state) as shown in Fig.3.2 (b). Either a "C" or "O" shaped metallic ring is printed on a 3.175 mm thick, 4 cm by 4 cm G10/FR4 square lattice for the OFF and ON states, respectively, with a ground plane at the bottom. An eigenmode simulation is performed in an 8 cm high airbox with PEC assigned on the top surface and periodic boundaries around it using Ansys Electronics Desktop. The band diagram is shown in Fig. 3.2 (c). The OFF state supports surface waves from 2.5 GHz to 4 GHz shown as the blue solid line. Since the modes above the light line are leaky waves, a complete bandgap below the light line, covering from 3.25 GHz to 3.55 GHz, is created for the ON state represented by the red solid line. A bandgap arises from the interaction between the resonance and the incident waves [53], as illustrated in Fig.3.2 (b). Thus, this structure can be used within the bandgap region by integrating with diodes at the gaps of the "C" shape geometry as shown in Fig. 3.2 (d). When the incoming power is high, the gaps are closed by the triggered diodes, and thus the unit cells are in the ON state with a bandgap. If the illumination is not high enough to turn on the diodes, the metallic ring remains in the "C" shape, and the surface supports surface wave propagation throughout the entire frequency band.

3.1.2 EM-Circuit Co-Simulation

To prove this concept, an EM-circuit co-simulation is conducted using Ansys Electronic Desktop. The full wave simulation model is shown in Fig. 3.2 (d). The OFF state unit cell is expanded to an 8 unit cell model placed inside a transverse electromagnetic (TEM) waveguide, whose top and bottom sides are assigned with PEC, front and back are assigned with PMC, and left and right are assigned with wave ports with proper characteristic impedance according to the size of the TEM waveguide. We chose this number of unit cells for two reasons: 8-unit is the

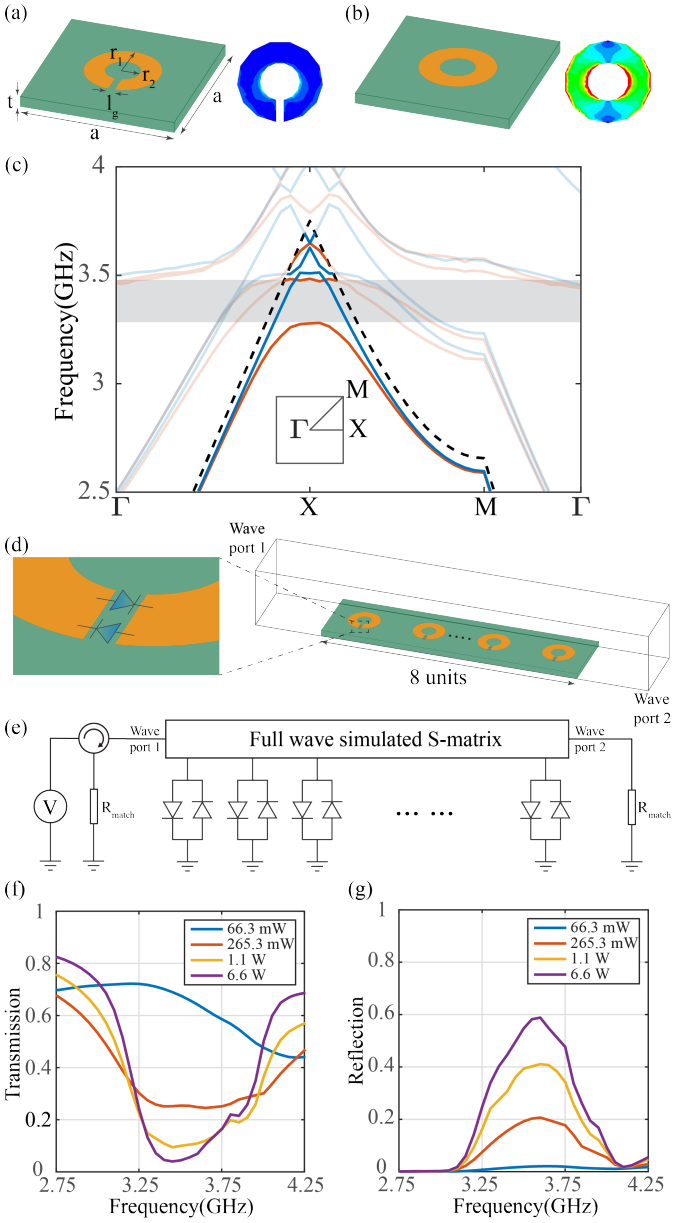

Figure 3.2. The ON and OFF unit cell design and EM-co simulation results. (a) The OFF state unit cell design (left) and its surface current at 3.4 GHz (right). $a = 40$ mm, $r_1 = 9.6$ mm, $r_2 = 4.44$ mm, $l_g = 1.7$ mm, $t = 3.175$ mm. The substrate is G10/FR4 with $\varepsilon_r = 4.8$. (b) The ON state unit cell design (left) and its surface current at 3.4 GHz (right). (c) Band diagram for the ON (red solid line) and OFF (blue solid line) state. Black dashed line: light line. Shaded area: the first bandgap region. (d) Full wave simulation model in a TEM waveguide. (e) Simulated schematics in Ansys Circuit. (f) The transmission rate at different power levels simulated for the model in (d). (g) The reflection rate at different power level simulated for (d).

smallest size to reduce high incident power by 10 dB, and additionally it allows low computation cost and high simulation accuracy. For a given incident power, the reflection first increases as the number of the units increases, then stops rising once the transmitted power is not high enough to trigger the next diode. The S-matrix of the structure in Fig.3.2 (d) is imported to Ansys Circuit as a component after being solved by the full wave simulator HFSS from DC to 12 GHz. The lumped ports at the gaps are connected with a pair of oppositely oriented diodes (Nexxim level 6 nonlinear microwave diode model) to perform a transient simulation in the circuit simulator as shown in Fig.3.2 (e). One of the wave ports is connected with a sinusoidal voltage source at different power levels, and the other one is connected with a resistor with the same resistance as the characteristic impedance of the wave port to measure the transmission. The structure works in a hybrid state of the ON and OFF states depending on the incident power as shown in Fig. 3.2 (f) and (g). It is observed that as the power rises, the transmission decreases and the reflection increases for frequencies inside the bandgap range, proving that the structure can reduce transmission by reflection with a self-induced bandgap. At 3.55 GHz, 66 % of the incident power propagates through the TEM waveguide with 66 mW input, while only 2 % is collected by the receiving port with 6.6 W input with 58 % of incident power reflected back to the transmitting port. We studied the loss in full-wave simulation for the 1 by 8 unit sample using the same setup as in Fig. 3.2 (d) by summing up the coupling coefficient between each of the lumped ports and the transmitting port with the impedance of the lumped ports assigned to be 5.8 Ohms. The total loss is around 1 %. Note that the rest of the power is absorbed by the lossy FR4 substrate (loss tangent 0.02), which could be reduced by using a lower loss substrate such as Rogers Duroid 5880. The results show that the working band (3 GHz to around 4 GHz) is wider than the bandgap shown in Fig. 3.2 (c), which stems from a second bangap above 3.55 GHz.

3.2 Measurements

To verify the existence of the bandgap and the power-dependent effect, two measurements are conducted on a pair of 2D 6 by 8 unit cell static surface and the diode-integrated PCB prototypes. All PCBs are manufactured in the OFF state. Copper wires are soldered at the gaps of the OFF state sample to create an ON state prototype in Fig. 3.3 (b), and a pair of opposite oriented Schottky diodes (Infineon BAT15-04W) are connected at the gaps to build a diode-integrated metasurface in Fig. 3.3 (c).

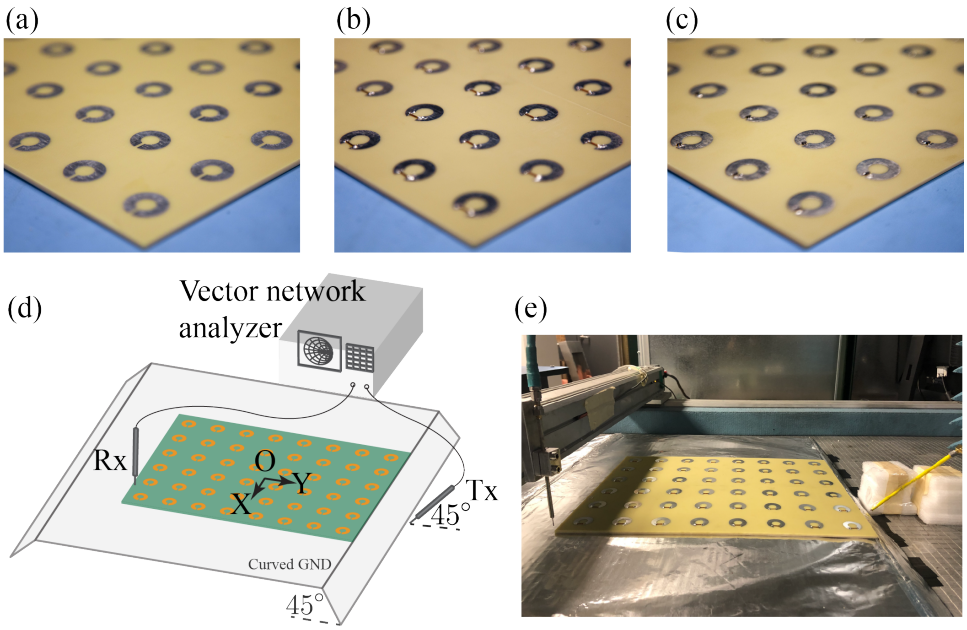

Figure 3.3. Prototypes and measurement setup. (a) The OFF state prototype. (b) The ON state prototype. (c) The diode-integrated prototype. (d) The near field scan measurement setup. (e) A picture of near field scan measurement.

3.2.1 Near Field Scan

The first measurement is the near field scan, as shown in Fig. 3.3(d) and (e), to confirm the bandgap region of the manufactured samples. The prototype is placed on a lifted ground plane, the end of which is a 5 cm long 45° slope, to separate the surface wave coupled to the structure and the free space plane wave generated from the 45° tilted transmitting probe Tx

which is connected to a two-port vector network analyzer (Keysight E5071C). After travelling through the device under test, the signal is collected by the receiving probe Rx, which scans over the sample with a 0.5 cm resolution in both X and Y directions at 1 cm height above the ON and OFF boards. The transmission S_{21} (average of 8 sets of measurements) from 2.5 GHz to 4 GHz is recorded to represent the E_z field intensity. To filter out reflections from the surrounding environment, a 1 ns time gating is applied in time domain by performing the inverse Fourier transform. The field scan at different frequencies are shown in Fig. 3.4.

Here we observe a suppression in transmission from 3.1 GHz to 3.6 GHz, which shows a good agreement with the eigenmode simulation in Fig.3.2 (c). For frequencies outside the bandgap, such as 2.75 GHz and 4.05 GHz, the difference in the field scan results between the ON and OFF states is negligible. On the other hand, for frequencies inside the bandgap, such as 3.3 GHz, 3.45 GHz and 3.6 GHz, the OFF state scan demonstrates a much stronger field compared to the ON state. These near field scan results indicate that the bandgap topology helps to reduce the transmission.

3.2.2 High-power Measurement

After verifying the working status of the static state models, the diode-integrated metasurface is measured under different power levels. The samples are placed on a 120 cm by 60 cm ground plane. As shown in Fig. 3.5 (a) and (b), the signal is generated by a VNA (Keysight E5071C) and amplified by an RF power amplifier (Ophir 5265), then radiated by a 50° tilted rectangular waveguide (WR284, 2.6 GHz to 3.95 GHz) to separate the surface wave and the plane wave. We estimate the amount of surface wave energy coupled to the surface via simulations using the exactly same setup in Fig.5 (a) and (b). By integrating the Poynting vector close to the ground plane, we achieve a conclusion that around 48 % of the total input power is coupled to surface waves. The output power varied from 30 dBm to 52 dBm across 3 GHz to 3.6 GHz. According to full wave simulation, the maximum voltage across the diodes is 3.2 V/m with a 52 dBm input, which is lower than the break down voltage of the diodes 4 V/m. Thus, all

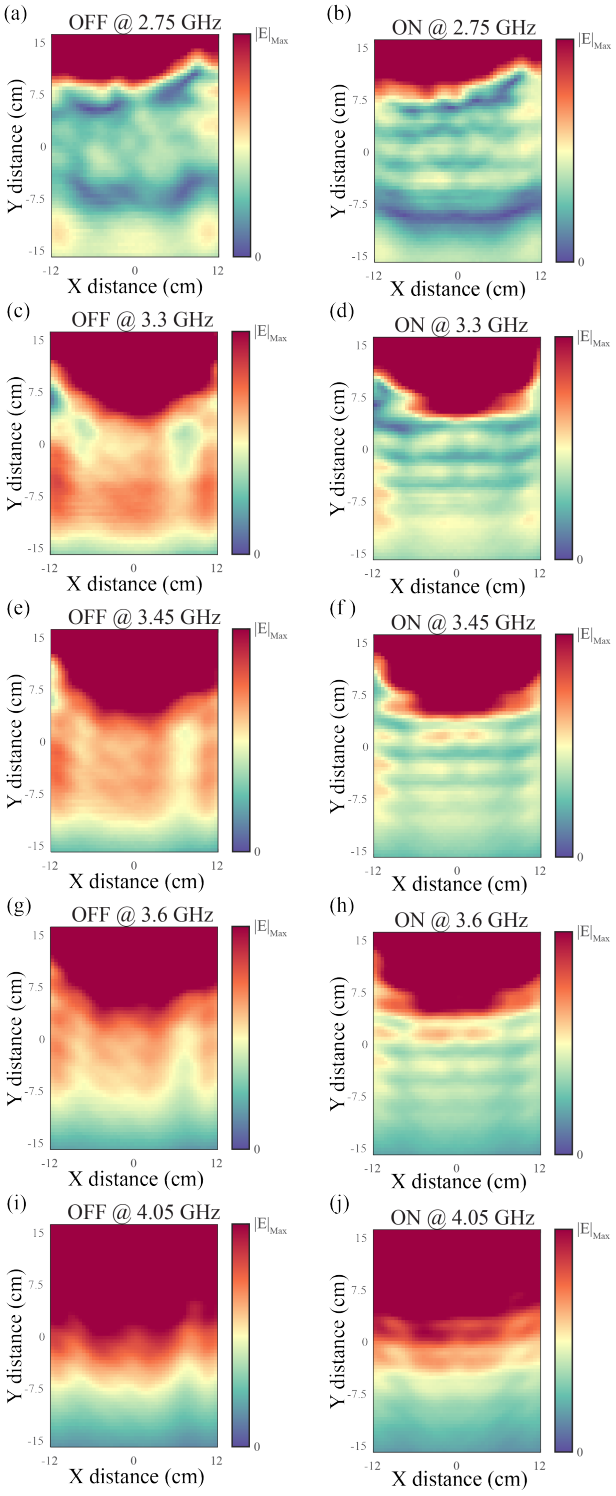

Figure 3.4. The near field scan results for the ON and OFF states at different frequencies. The first row: the OFF state field scan after adopting time gating at 2.75 GHz, 3.3 GHz, 3.45 GHz, 3.6 GHz, 4.05 GHz, respectively. The second row: the ON state field scan after adopting time gating at 2.75 GHz, 3.3 GHz, 3.45 GHz, 3.6 GHz, 4.05 GHz, respectively.

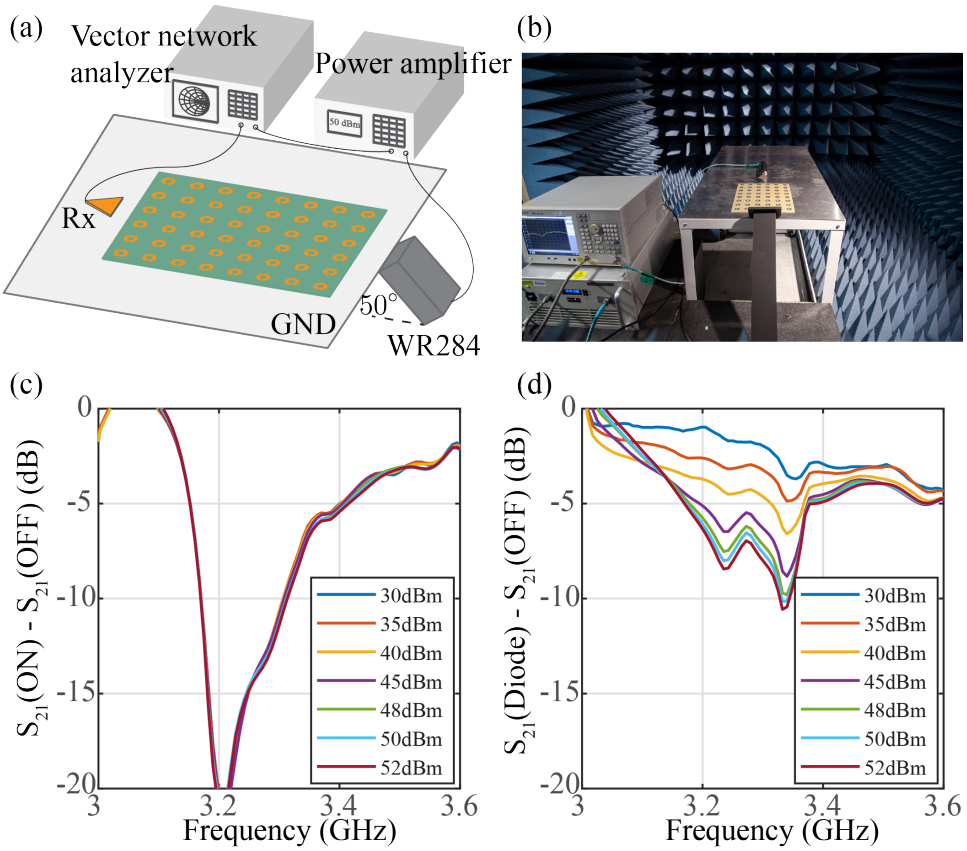

Figure 3.5. The high-power measurement and results. (a) The measurement setup. (b) A picture of the measurement. (c) The static state results. (d) The diode-integrated prototype results. The corresponding power density at the location of the source is 41 mW/cm^2 (30 dBm), 129 mW/cm^2 (35 dBm), 407 mW/cm^2 (40 dBm), 1288 mW/cm^2 (45 dBm), 2570 mW/cm^2 (48 dBm), 4073 mW/cm^2 (50 dBm), 6455 mW/cm^2 (52 dBm).

measurements are performed below the breakdown. After propagating through the device under test, the signal is received by a dielectric horn antenna Rx at 1 cm height above the surface with a 40 dB attenuator to guarantee the captured power is within the safe range of the VNA. This experiment is performed inside a sealed anechoic chamber, and all the measurement devices involved are remotely controlled to avoid human body exposure to RF radiation. To reduce the noise and fluctuations, the data is the average of 8 measurements.

The static state prototypes, as well as the diode-integrated sample are measured under various power levels. The OFF state results are used as the baseline representing the surface with no effect on the incoming wave. Subtracting the measured S_{21} for the OFF state from that

for the ON state or diode-integrate sample, the difference directly indicates the impact brought by the self-induced bandgap. As shown in Fig. 3.5 (c), the difference between the ON and OFF states remains the same for different power levels across the whole frequency range. The largest difference occurs at 3.2 GHz for all power levels. In contrast, the diode-integrated sample presents a power-dependent behaviour characterized by the same bandgap. As the incident power increases, the transmission decreases, reaching a 10.6 dB drop at 3.33 GHz with a 52 dBm input. The difference in S_{21} continuously increases as the power rises, because the diode gradually saturates and the reflection approaches a constant rate, showing a similar trend to the simulated results in Fig.3.2 (f). The results shown in Fig.3.5 (d) differs from that in (c) because the incident wave cannot trigger all the diodes, instead, only the diodes close to the Tx, and the difference caused by the diodes' rectification effect is magnified in dB scale. Additionally, the parasitic capacitance of the diodes shifts the lowest transmission point from 3.2 GHz to 3.33 GHz. The loss due to diodes' rectification is studied row by row in full-wave simulation using the same setup as in the measurement shown in Fig.5 (a) and (b). To examine the loss in the first row, 6 lumped ports are assigned at the gaps of the C-shape metallic rings in the first row to obtain the coupling between the waveguide and each lumped port. For the second row, we turned on the first row and assigned lumped ports at the gaps of the second row, etc. The total loss is the summation of all coupling coefficients, resulting in 5% even when the threshold voltage is ignored. Thus the power lost due to diode rectification is insignificant.

3.3 Conclusions

In this chapter, we propose the first power-dependent metasurface by directly changing the band structure to open a bandgap under high power illumination. It automatically changes from a surface wave supportive state to a bandgap topology as the incident power increases. Measurements, together with simulation results, prove the validity of this concept. The near field scan shows the static behaviour of the proposed topology in the ON and OFF states, proving

existence of a bandgap, which reflects incident signals, from 3.1 GHz to 3.6 GHz. The following high-power measurement demonstrates the power-level dependent performance for the diode-integrated prototype. The proposed sample shows 10 dB less transmission compared to the OFF state at approximately 3.3 GHz with 52 dBm input.

The proposed structure is low-cost, low-profile and it has a simple geometry which does not require any control circuit. Additionally, it shows a wider transmission variation range (10 dB) compared to previous work on power-dependent absorbers (approximately 4.8 dB for [46, 47]). This low-cost, PCB-based, power-dependent metasurface can be adopted to reduce RF exposure to sensitive electronic devices while still allowing small signal communication for the protected systems. This self-induced bandgap concept opens a way to many similar designs based on manipulating the topology of the surface wave band structure.

This chapter is based on the following paper: Yang, X., Wen, E., & Sievenpiper, D. F. (2022). "Power-Dependent Metasurface With Self-Induced Bandgap." *IEEE Antennas and Wireless Propagation Letters*, 21(6), 1115-1119. The dissertation author was the primary investigator and author of this paper.

Chapter 4

Nonlinearity Induced Nonreciprocity

Reciprocity is a fundamental property of non-magnetic, passive, linear and time-invariant systems, which states that the transmission from the source to the observation point remains the same if their locations are interchanged. In the past decades, with the fast development in acoustics[54], electromagnetism[55, 56], optics[57, 58], and electronics[59], breaking the transmission symmetry becomes a crucial task for various applications, from optical isolation to wireless communication[60, 61, 62, 63]. In the microwave regime[6, 64], nonreciprocal metasurfaces raise growing interests because they provide a compact, ultra-thin, lightweight platform to manipulate waves in a unidirectional manner, which enables nonreciprocal wave absorbing, nonreciprocal beam steering, frequency conversion, and consequently can be used to protect sensitive devices from high energy sources[65, 66, 62, 67].

The conventional approach to break reciprocity in electromagnetism relies on ferrite material, such as yttrium iron garnet and iron oxide with other metallic elements, which exhibits the Faraday effect[68, 69]. While the Faraday rotation enables the functionality of optical isolators and circulators, polarization rotations might not be preferred in wireless communication systems (especially for linear polarization, maintaining the polarization state of the transmitted signals is essential, unnecessary polarization mismatch occurs if the linear polarization is rotated which results in lower transmission rate and signal to noise ratio). Besides, ferrites are expensive compared to printed circuit board designs. It is bulky and brittle in large-scale applications

and incompatible with modern lightweight and compact integrated circuits devices. In addition, external magnetic bias is typically needed for ferrite-based designs [70, 71].

Recent research proposes to violate the fundamental assumption of the Lorentz reciprocity theorem to break the transmission symmetry by employing spatial-temporal modulation, active elements or nonlinearity[55, 56, 54]. However, such modulation strategy usually requires a controlling system which needs an additional power supply[72, 73, 67, 74, 75]. In addition, some works adopt active electronic elements, including transistor-based amplifiers/switches and varactors to break the reciprocity[63, 76, 77, 78]. Although modulation is absent, those designs still require a biasing circuit. Another concern is that these approaches require a large biasing/modulation signal under high power incident such that the biasing/modulation signal overwhelms the RF signal. Nonlinearity, on the other hand, provides an alternative to engineer all-passive nonreciprocal devices. Material with strong Kerr nonliearity has been proven to be a good candidate for nonreciprocal optical devices, including circulators and isolators, if the structure is designed to have field asymmetry when illuminated from opposite directions[79, 80, 81, 60, 82].

However, other types of nonlinearity need to be implemented as a counterpart to the electro-optic effect in microwave frequencies to develop an all-passive, magnetic-free nonreciprocal structure. Ref [83] adopts an asymmetrical structure and resonators loaded with an imaginary lumped component, whose capacitance varies with continuous AC signals, to imitate the Kerr effect, such that the resonance frequency shifts differently for waves propagating in opposite directions. An experimental work in microwave circuits proved this concept by adopting varactors to introduce a frequency shift to resonators in the megahertz range [84]. However, this approach can not be scaled to higher frequencies since the varactors are infeasible due to their high loss.

Here, we propose a feasible all-passive nonreciprocal metasurface design without any biasing based on a microstrip line (MSL) with the integration of accessible nonlinear elements, Schottky diodes, to break the transmission symmetry. The simplicity of this model allows fast design in a circuit model by treating the MSL as an ideal transmission line (TL), which makes this

method more appealing. The field asymmetry directly originates from the impedance contrast of the MSL, which is later proven to be the determining parameter of the nonreciprocity. The Schottky diodes connect a matching stub to the ground plane, and the field intensity at their location differs significantly for waves propagating in opposite directions. Thus, the matching stub is either open or shorted depending on the incidence direction, which further determines the transmission. In this article, we extend the MSL structure to a three-layered metasurface with low transmission in one direction while allowing wave propagation from the opposite direction, which resembles the diode behaviour. Immune to Faraday rotation, it is potentially applicable in various scenarios including protecting radar or communication systems against high power microwave sources, without using conventional EM circulators and isolators. Since modulation is absent, this design can be scaled to other frequencies, while time-modulated design is limited due to the difficulty of fast modulation at higher frequencies and the response time of the modulated components. In addition, it is more universally applicable when a bias is inaccessible.

4.1 Results

4.1.1 Transmission Line Design

Nonlinear devices are defined by their power-dependent behaviour. Thus when the field distribution changes between one incident direction and the opposite, placing a nonlinear component at the field asymmetrical location enables the whole system to be nonreciprocal. Take the ideal diode for instance, the ON and OFF working states are determined by the local field intensity and induce two distinct operating states of the system for different transmission/absorption due to the change of its topology. The nonreciprocity is maximized when deploying the diodes at the strongest asymmetry point. Then, a nonreciprocal metasurface can be developed by simply folding this building block and separating the two halves by a ground plane with antennas connected to receive and transmit signals.

The proposed TL model that creates and utilizes a field asymmetry is illustrated in

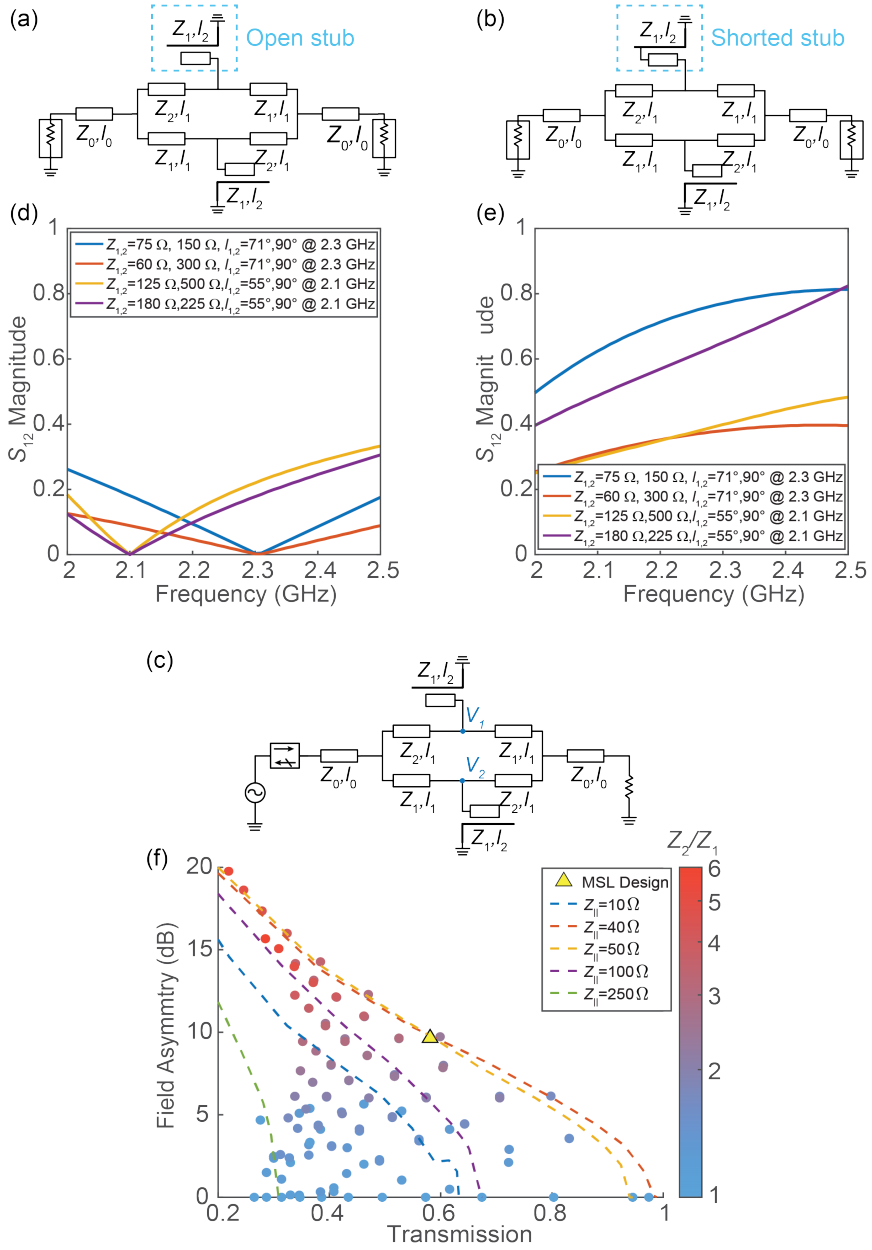

Figure 4.1. Ideal transmission line models. $Z_0 = 50\ \Omega$. Z_1 and Z_2 are the characteristic impedance of the transmission line branches. (a) OFF state (diodes not triggered, open stub) circuit model. (b) ON state (diodes triggered, shorted stub) circuit model. (c) Transient simulation model in OFF state. (d) Transmission in the OFF state. (e) Transmission in the ON state. (f) Trade-off between field asymmetry and the ON state transmission with $l_1 = 71°$, $l_2 = 90°$ at 2.3 GHz. The color of the dots represent the impedance contrast defined by Z_2/Z_1.

Fig.4.1. Starting with the ideal circuit model, two different impedances, Z_1 and Z_2, are chosen to create the field asymmetry at the end of the matching stub. Nonreciprocity is then achieved by integrating diodes on the upper stub. As a proof of concept, we simplified the nonlinear power-depended behaviour of the diodes to two static states so that the matching stub is either an open (the OFF state, Fig.4.1 (a)) or a shorted stub (the ON state, Fig.4.1 (b)) depending on the field intensity under different incident directions, while the lower stub is always open. When it is shorted, better matching occurs, resulting in higher transmission. Otherwise, it has lower transmission rate. Since the state of the upper matching stub is determined by the field intensity, a stronger asymmetry in field distribution is crucial for achieving higher nonreciprocity.

To analyze the field asymmetry of this TL design, we performed S parameter and transient simulations in Advanced Design System (ADS) to study the static states behaviour. The field asymmetry is defined by the ratio of voltage at two observation points, V_1 and V_2 in Fig.4.1 (c) as $20log_{10}(\frac{V_2}{V_1})$. Although the diode is located at the end of the matching stub, it is reasonable to approximate the ratio of the field intensity at that location by these observation points. The transmission rate for the static states are studied by S parameter simulation as in Fig.4.1 (d) and (e). The length of the matching stub, L_2, determines the operating frequency which has the highest field asymmetry. The minimum transmission occurs at the frequency when the electrical length of the matching stub is $\lambda/4$ in the OFF state, since the waves are shorted by the matching stub, as shown in Fig.4.1 (d). For the ON state, since one matching stub is shorted, higher transmission is observed as illustrated in (e). L_1 does not affect the overall performance here since only an ideal TL is involved, but it should be chosen properly in a real electromagnetic (EM) design to follow the TL principles. The field asymmetry is dominated by impedance contrast between Z_1 and Z_2. By examining different impedance values and contrast for $50\ \Omega \leq Z_1 \leq Z_2 \leq 500\ \Omega$, a trade-off between field asymmetry and the ON state transmission is observed in Fig.4.1 (f) [85]. All the data in (f) is simulated with $l_1 = 71^\circ$, $l_2 = 90^\circ$ at 2.3 GHz.The color in (f) represents the impedance contrast defined by $\frac{Z_2}{Z_1}$. Warm-colored dots are concentrated on the upper-left corner and the cold-colored ones are scattered at the bottom,

demonstrating the trade-off relationship between impedance contrast and field asymmetry. In addition, all data points are gathered in the lower-left half and is bounded by $Z_{\parallel} = 50\,\Omega$, where $\frac{1}{Z_{\parallel}} = \frac{1}{Z_1} + \frac{1}{Z_2}$, which proves the trade-off between field asymmetry and transmission. Higher impedance contrast does create stronger field asymmetry, but the discontinuities and reflections largely undermines the transmission rate. Thus, the upper limit scenario occurs when avoiding the unnecessary reflections due to mismatch. As expected, the field distribution is completely symmetrical if $Z_1 = Z_2$.

4.1.2 Microstrip Line Design

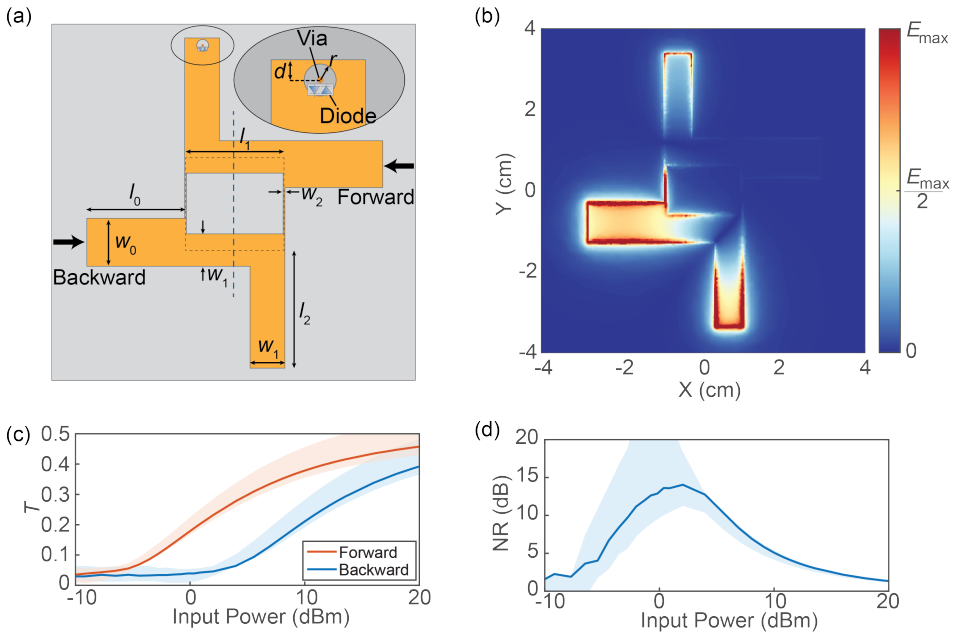

Figure 4.2. Microstrip line model. (a) Illustration of microstrip line translating from the yellow triangle in Fig.4.1 (f). The width of the microstrip line $w_{0,1,2}$, corresponds to characteristic impedance $Z_{0,1,2} = 50, 66, 200\,\Omega$. (b) Field distribution in the OFF state under backward incidence at 2.3 GHz. The color indicates the electric field strength. (c) The simulated transmission rate (T) under different propagation directions. Red line: forward incidence for 2.05 GHz. Blue line: backward incidence for 2.05 GHz. Red shaded area: forward incidence from 2.03 GHz to 2.15 GHz. Blue shaded area: backward incidence from 2.03 GHz to 2.15 GHz. (d) The simulated nonreciprocity (NR). Blue line: 2.05 GHz. Blue shaded area: 2.03 GHz to 2.15 GHz.

To transform the ideal circuit model to a feasible electromagnetic prototype, we adopt a MSL which can be easily fabricated and integrated to printed circuit board (PCB) designs.

Fig.4.2 (a) illustrates a MSL design with a reasonable field asymmetry and transmission rate at the upper limit of the trade-off relation, shown as the yellow triangle in Fig.4.1 (f). The impedance of Z_1 and Z_2 is 66 Ω and 200 Ω, respectively. The length of the matching stub is l_2 determines the center frequency to be around 2.3 GHz. l_1 should be as short as possible to shrink the size, but not to short to still behave as a TL. The thickness of the substrate is chosen such that the width of a 200 Ω MSL can be precisely manufactured. A pair of oppositely oriented diodes are required to react to sinusoidal waves. Incidence from the right-hand side is defined as forward propagation and excitation from the opposite side is called backward propagation.

The static field distribution in the OFF state is illustrated in Fig.4.2 (b) under backward excitation. Since this structure has 180° rotational symmetry, the forward field distribution can be obtained by rotating that of the backward by 180°. That is to say the field asymmetry at the location of the diode can be seen as the ratio between the upper stub and the lower stub under forward or backward incidence. The transmission rate for static forward and backward propagation is 0.65 and 0.09 at 2.3 GHz, and the field asymmetry is 8.3 dB, which agrees well with the circuit model.

This structure is further studied using EM-circuit co-simulation to verify its power-depended nonreciprocal behaviour with the integration of a real Schottky diode for fast response. Power-related nonreciprocal transmission is observed from 2.03 GHz to 2.15 GHz with more than 10 dB nonreicprocity as shown in Fig.4.2 (c) and (d). Frequency shift is inevitable due to the integration of real diodes. Here, the transmission (T) is the voltage ratio between the received and the transmitted, and the nonreciprocity is defined by

$$\mathrm{NR} = 20log_{10}(\frac{T_+}{T_-}), \tag{4.1}$$

where $T_\pm$ denotes the forward and backward transmission rate. The incident power is calculated by $\frac{V_{\text{tran.}}^2}{2Z_0}$, where $V_{\text{tran.}}$ is the amplitude of the voltage source. The system is reciprocal under low-power illumination since the diodes are not triggered. As the power increases, the nonreciprocity

rises because the diodes are only turned on under forward incidence and it reaches the maximum when the voltage across the diodes of backward excitation is close to the threshold of the diodes. The transmission rate finally converges as the incident power continues increasing, since the threshold of the diodes become negligible compared with the voltage cross the diodes. More than 10 dB nonreciprocity is achieved between -2.8 dBm and 5.6 dBm incidence for 2.05 GHz. The dynamic range of the proposed design is adjustable by varying the impedance contrast. An example is given in the 4.4.2 and Fig.4.7 with larger dynamic range by increasing $\frac{Z_2}{Z_1}$. Note that the width of the transmission line should be considered for easy fabrication. The static states and power-dependent nonreciprocal performance is further demonstrated through measurement and the results are included in 4.4.1 and Fig.4.5, which proves its potentiality as a building block of EM isolators and circulators.

4.1.3 Metasurface design and measurement

After demonstrating the nonreciprocity of the MSL through simulations and measurements, we extend it to a metasurface as illustrated in Fig.4.3 (a), which can be used to protect sensitive devices from high power sources while allowing one-way communication. This is attained by folding the MSL structure and separating the two halves on two layers with a ground plane in between as illustrated in Fig.4.3 (b). These MSL layers are connected by two vias through the holes on the central ground plane. Two patch antennas are attached to the MSL to receive and transmit the EM signals. Since the patch antenna only supports linear polarization in the Z direction, all the following results are the outcome under Z-polarization illumination. The simulated results for the orthogonal polarization in X direction is shown in 4.4.3 and Fig.4.8, showing zero transmission rate for both propagation directions.

The performance of this design is studied using EM-circuit co-simulation on a unit cell with periodic boundaries to reduce the computational cost. Since the excitation is free space waves, the definition of input power is different than that in the MSL simulations, where the incident is calculated by the voltage between the MSL and ground plane. Here, the input refers

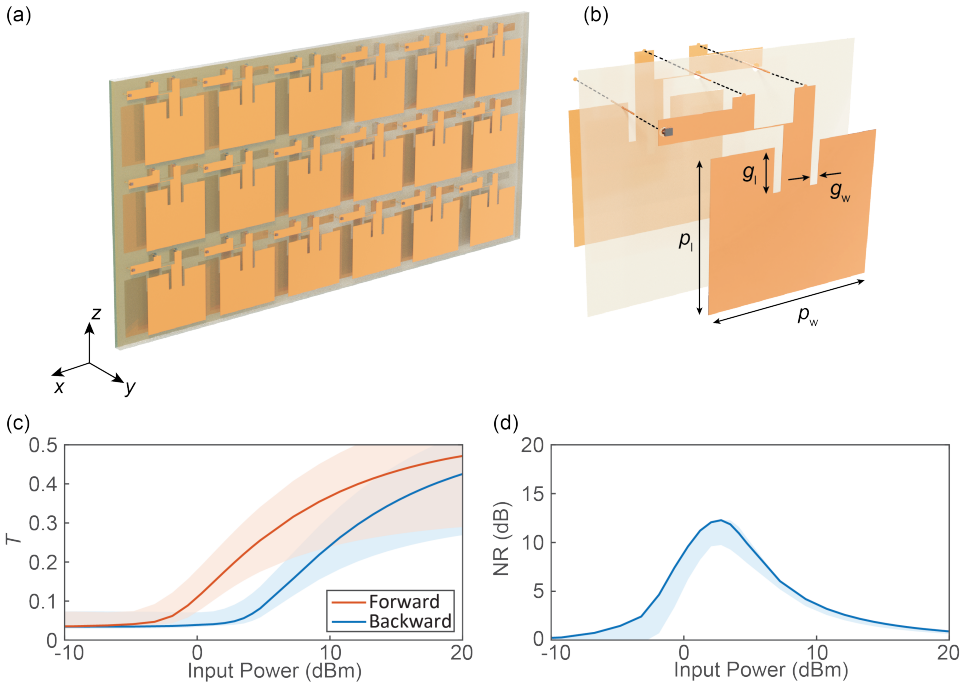

Figure 4.3. Metasurface design. (a) Illustration of a 6 by 3-unit surface. (b) A detailed illustration of the three-layer layout. p_l and p_w are the length and width of the patch antenna, respectively. g_l and g_w are the length and width of the matching slot on the patch antenna. (c) The simulated transmission rate (T) under different propagation directions. Red line: forward incidence for 2.21 GHz. Blue line: backward incidence for 2.21 GHz. Red shaded area: forward incidence from 2.18 GHz to 2.25 GHz. Blue shaded area: backward incidence from 2.18 GHz to 2.25 GHz. (d) The simulated nonreciprocity (NR). Solid line: 2.21 GHz. Shaded area: 2.18 GHz to 2.25 GHz.

to the power over the area of one unit cell. Similar to the MSL structure, a nonreciprocal transmission with the same trend is observed as shown in Fig.4.3 (c) and (d). The bandwidth of this unit cell is narrowed down to 2.18 GHz to 2.25 GHz due to the patch antenna.

A 6 by 3-unit prototype, as shown in Fig.4.4 (c), is fabricated to measure its nonreciprocity. This experiment is conducted in an anechoic chamber, as in Fig.4.4 (b), to minimize the effect from the environment. To avoid diffraction and to confine energy propagation, the surface is placed inside a parallel plate TEM waveguide with the same height as illustrated in Fig.4.4 (a). Microwave absorbers are placed at the top and the bottom of the waveguide to further reduce diffraction. The incident signal is generated by a vector network analyzer (VNA), amplified by a power amplifier and transmitted by a horn antenna. After propagating through the surface, the

signal is received by another horn antenna connected to the VNA. Note that the input power here has the same definition as in Fig.4.3 (c) and (d), referring to the the power incident on each unit cell. Having the setup fixed, the backward transmission is measured by flipping the sample. In addition to the forward and backward transmission scenarios, we also measured the transmission of a blank waveguide (the blank case), representing the total incident power, and the diffraction from the sides with an equal size aluminum sheet (the PEC case). Although the waveguide is wider than the sample, the diffraction measured under the PEC case is 30 dB less than that of the blank case, which is negligible. Thus, it is reasonable to assume that no diffraction occurs in this measurement. The transmission in the measurement is defined by

$$T_{\pm} = \sqrt{\frac{P_{\pm}}{P_{\text{blk}}}}, \tag{4.2}$$

where $P_{\pm/\text{blk}}$ is the absolute power received by Rx measured with board under forward/backward propagation and the blank case. The nonreciprocity is still defined by Equ.(4.1). The measurement results are shown in Fig.4.4 (d) and (e), similar to the simulation results in Fig.4.3, a nonreciprocal transmission behaviour is observed under different incident directions. More than 10 dB isolation is achieved between -1.8 dBm to 4.7 dBm at 2.05 GHz.

4.2 Discussion

We proposed a MSL-based all-passive nonreciprocal metasurface by applying nonlinear devices at field asymmetrical locations, and verified its "diode"-like one-way behavior under opposite incident directions through experiments. Unlike the Kerr effect approach in photonic systems, where the nonlinearity originates from the material, this method is rather general in the microwave regime. Since the field asymmetry comes from the metallic topology, the substrate is free of choice. The option for diodes are also numerous in various packages, material and arrangement. Moreover, it can be scaled to other frequencies, and it is rather easy to modify the input and output impedance by adjusting the width of the MSL. In addition, the working range of

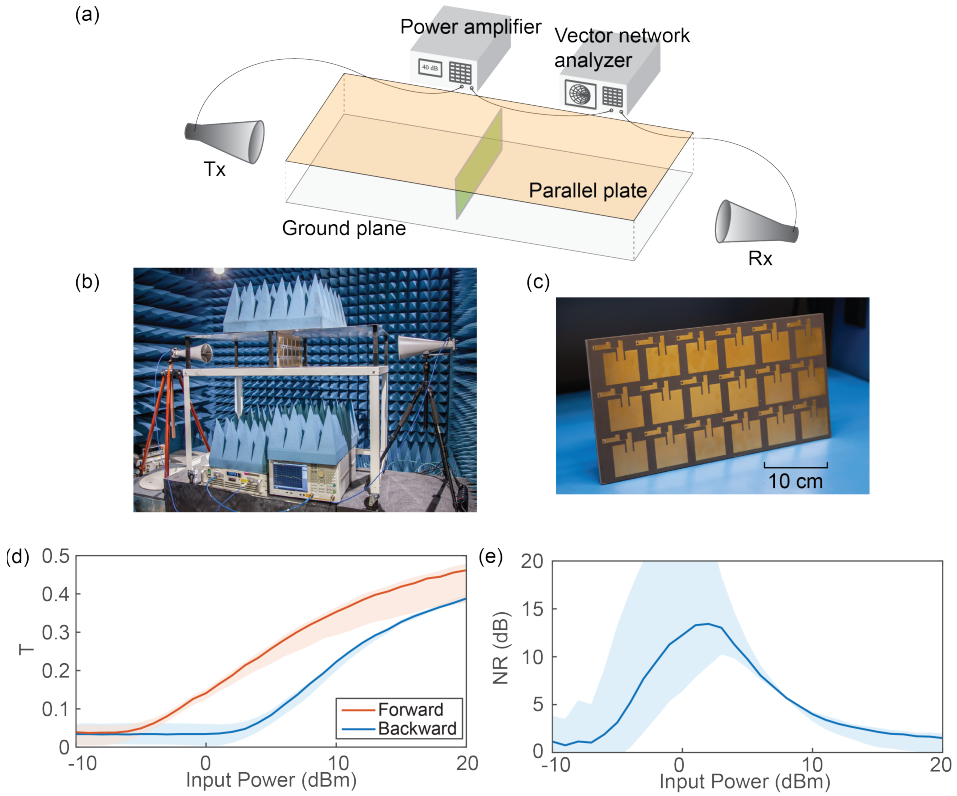

Figure 4.4. Measurement inside a TEM waveguide to reduce diffraction. (a) Illustration of measurement setup. (b) Picture of measurement setup. (c) Picture of the prototype. (d) The measured transmission rate (T) under different propagation direction. Red line: forward incidence for 2.05 GHz. Blue line: backward incidence for 2.05 GHz. Red shaded area: forward incidence from 2.02 GHz to 2.06 GHz. Blue shaded area: backward incidence from 2.02 GHz to 2.06 GHz. (e) The measured nonreciprocity (NR). Solid line: 2.05 GHz. Shaded area: 2.02 GHz to 2.06 GHz.

power is adjustable using different arrangements of diodes, which is equivalent to adopting diodes with different threshold voltages (see 4.4.2 and Fig.4.6). Different from the ferrite approach, its immunity to Faraday rotation makes it more appealing for communication systems. Different polarizations can be achieved using other types of antennas, or modifying the feeding point of the current design if polarization conversion is preferred. This lightweight, low-profile and low-cost PCB design is promising in various applications, including EM protecting layers such as radomes and nonreciprocal absorbing material, and EM isolators and circulators by cascading the MSL structure. We realize this design is subject to the limitation of dynamic reciprocity that small signals lose nonreciprocity in the presence of large signals [86], since the nonreciprocity is

induced by field intensity which is the summation of all signals.

4.3 Methods

4.3.1 Fabrication

The MSL structure is manufactured on a 3.175 mm thick 8.5 cm by 8.5 cm double-sided Duroid Rogers 5880 PCB with coaxial feed. The dimensions are $w_{0,1,2} = 9.7, 6.63, 0.31$ mm, $l_{0,1,2} = 1.9, 1.9, 2.4$ cm, $d = 1.4$ mm,$r = 1.2$ mm, and the radius of the vias are 10 mil. The center of the 66 Ω and 200 Ω MSL forms a square whose side length is l_1 shown as the black dotted line in Fig.4.2(a). The Schottky diode used in the EM-circuit co-simulation is BAT15-04W. There is a hole on the upper matching stub to place the diodes to connect the stub to the ground plane through a via in the ON state. The metasurface is fabricated on a three-layer 42.3 cm by 20.5 cm Duroid Rogers 5880 PCB, both of cores are 3.175 mm in thickness. The dimensions for the patch antenna, resonating at 2.19 GHz, are $p_{\mathrm{w}} = 53.87$ mm, $p_{\mathrm{l}} = 45$ mm, $g_{\mathrm{w}} = 2.5$ mm, $g_{\mathrm{l}} = 13$ mm. Note that the periodicity in y and z direction is 6.8 cm and 6.6 cm, respectively, to avoid overlapping of the top and bottom layer for a through via.

4.3.2 EM-circuit co simulation

After simulating the EM structure from DC to 8 GHz, we extract its S parameters and perform transient simulation in circuit with the diodes SPICE model provided by the manufacturer. The metasurface is simulated under periodic boundaries using unit cell. Studies of third order harmonics, third-order intermodulation product and 1-dB compression point is included in 4.4.4 and Fig.4.9-4.12, which show that the harmonics are negligible under all incident power and that the defined 1-dB compression point is out of the 10 dB nonreciprocity range.

4.3.3 Measurement

The TEM waveguide is 120 cm long, 60 cm wide and its height is 20.3 cm, which is the same as the prototype. The distance between the edge of the horn antenna (Rx) and the

TEM waveguide is 10 cm, which excites plane wave inside the waveguide. Devices involved: VNA, Keysight E5071C, power amplifier Ophir 5022, Tx and Rx RCDLPHA2G18B. Due to the involvement of an amplifier, instead of S parameters, the VNA is always measuring the absolute power on Rx. To measure under different incident power, the input power of the VNA varies from -40 dBm to -10 dBm with the amplifier providing a 30 dB amplification. All the data is averaged by 8 times, and the devices are controlled by Python.

4.4 Extended material

4.4.1 Microstrip line measurement

We fabricated three coax-feed MSL samples as shown in Fig.4.5. The measurement setup is similar to that using the TEM waveguide in the paper, despite that the prototype is directed connected to the VNA through coaxial cable. The transmission of static states agrees well with the simulated results, illustrated in (b) and (c). The diode-integrated sample exhibits more than 10 dB nonreciprocity from 2 GHz to 2.09 GHz, which validates the simulation results in Fig.4.2 of the paper. Here, the input power is exactly the same as in Fig.4.2, assuming the loss of cables and connectors in the measurement is negligible.

4.4.2 Dynamic range

The working range of power can be designed using different arrangements of diodes. In Fig.4.6, it is observed that using two pairs of opposite-oriented diodes shift the power up by 6 dBm, since the ”equivalent threshold” is doubled compared with one pair of diodes. Here, we are using ideal diodes with the same parameters in both scenarios to prove this concept. This can also be achieved by using diodes with different threshold.

The dynamic range can be expanded by increasing the impedance contrast between Z_1 and Z_2. Fig.4.7 shows an example to increase the dynamic range (-5.5 dBm to $+8.4$ dBm) of nonreciprocity, compared to the original design (-3 dBm to $+6$ dBm). Here, $Z_1 = 60\,\Omega$,

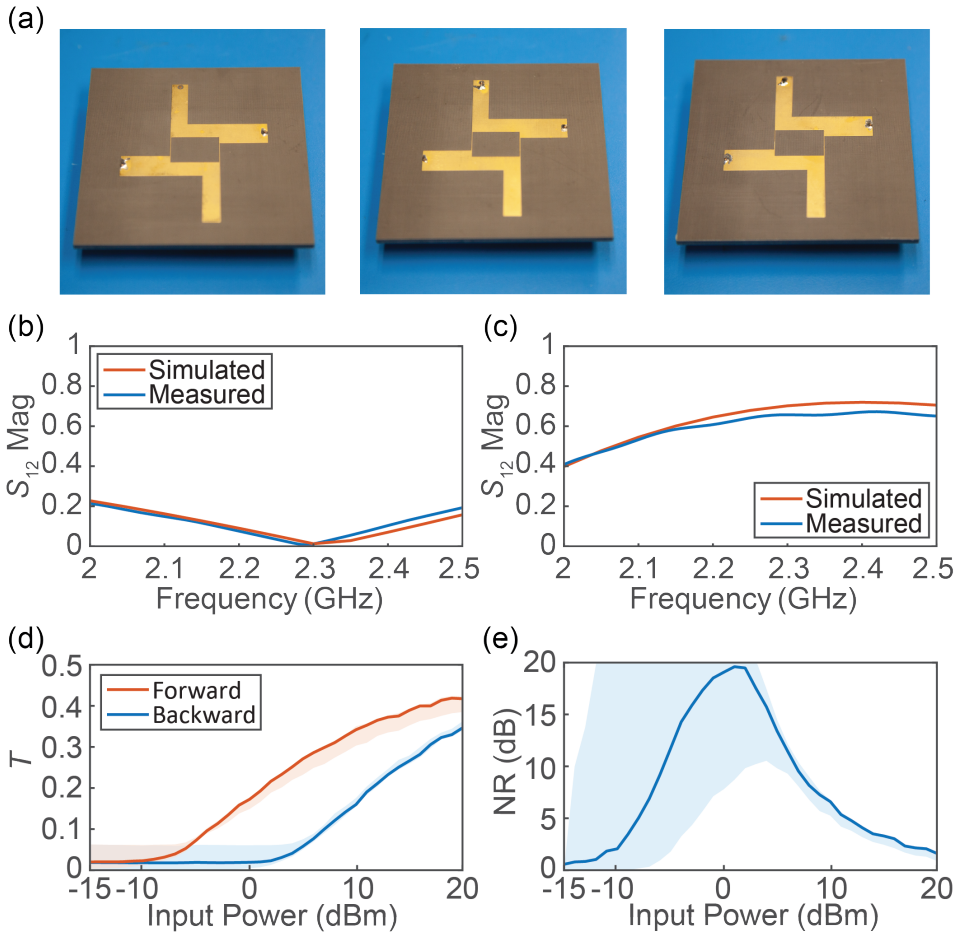

Figure 4.5. MSL measurement. (a) A picture of MSL prototypes for diode integrated sample, static ON state and static OFF state, respectively. (b) Measured and simulated transmission for static OFF state. (c) Measured and simulated transmission for static ON state. (d) Measured transmission under forward and backward propagation. (e) Measured nonreciprocity. Solid line: 2.04 GHz. Shaded area: 2 GHz to 2.09 GHz.

$Z_2 = 300\,\Omega$, corresponding to $w_1 = 7.4$ mm, $w_2 = 0.042$ mm. Note that in real applications, the width of the transmission line should be also considered for accurate fabrication.

4.4.3 Transmission for orthogonal polarization

To demonstrate the nonreciprocal behavior more rigorously, we show the transmission rate of the orthogonal linear polarization in the x direction as in Fig.4.8, showing zero transmission in the both propagation directions. Proving that the surface is reciprocal for z polarization, and polarization conversion is absent.

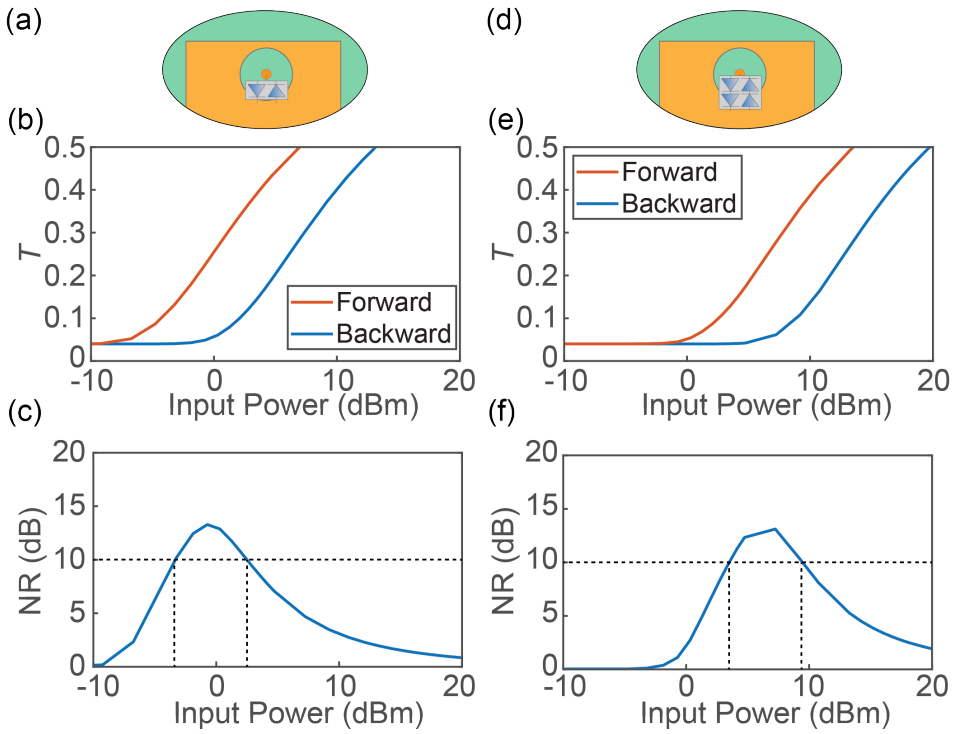

Figure 4.6. Dynamic range adjustment study. The power range can be modified by using different arrangement of diodes. (a)-(c) A pair of opposite-oriented diodes at the upper matching stub with its simulated transmission and nonreciprocity. (d)-(f) Two pairs of opposite-oriented diodes in series, shifting T and NR to higher working power by 6 dBm. All curves are plotted at 2.15 GHz.

4.4.4 Higher order harmonics, IM3 and 1-dB compression

We studied the higher order harmonics using a single-tone setup at $f_0 = 2.2$ GHz using EM-circuit co-simulation in Ansys HFSS, as shown in Fig.4.9. It is observed that the third order intercept point does not exist. The third order input intercept point (IIP3) is usually used to examine small signal input for weak nonlinear systems. However, in the proposed design, turning on the diodes results in an abrupt geometric change: the system is linear before the turning on of the diodes (before 0 dBm), and it becomes strongly nonlinear when the diodes are just triggered. Although IIP3 does not exist for the high power state, the harmonics are 20 to 30 dB lower than the fundamental frequency.

The third-intermodulation product is plotted in Fig.4.11 under different incident powers for forward and backward incidence at 2.2 GHz, respectively. The two-tone co-simulation setup

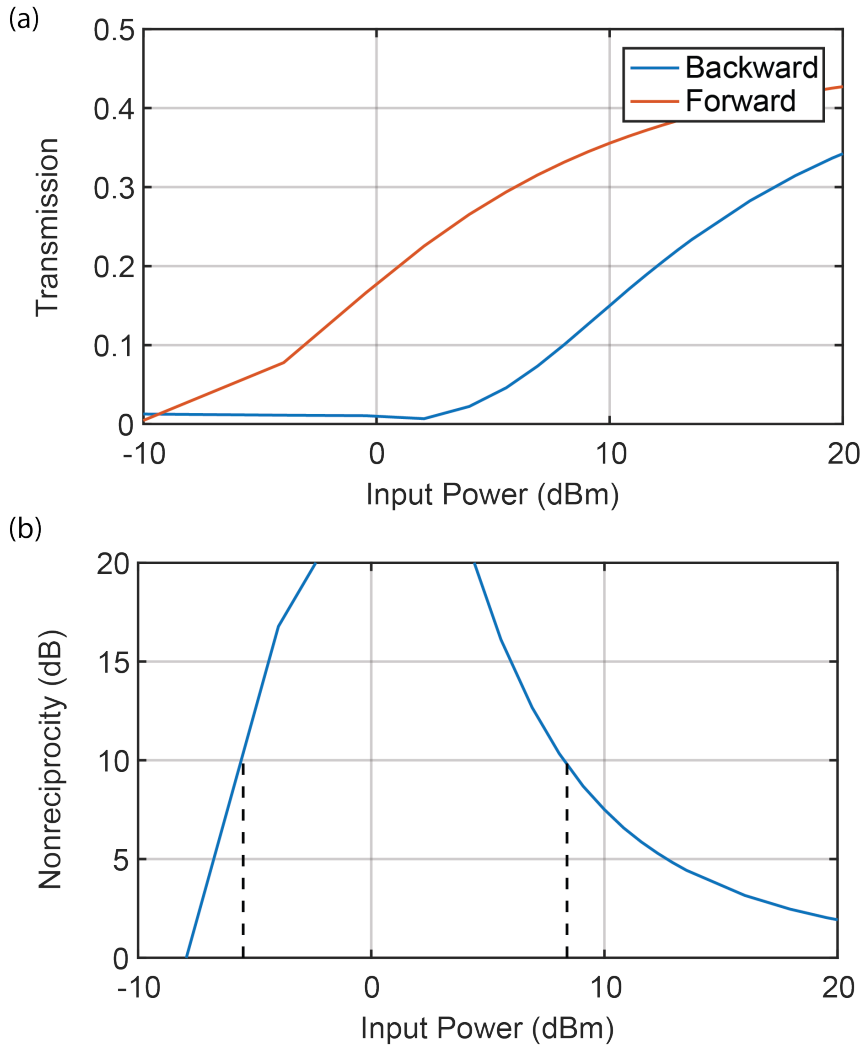

Figure 4.7. Expanded dynamic range study. The co-simulation results for $Z_1 = 60\,\Omega$, $Z_2 = 300\,\Omega$, corresponding to $w_1 = 7.4$ mm, $w_2 = 0.042$ mm at 2.1 GHz. (a) Transmission under forward and backward incidence. (b) Nonreciprocity.

in ADS is shown in Fig.4.10. The S parameters of the proposed unit cell are extracted from an HFSS simulation and imported to an ADS simulation as an s3p file. Marker 1 (m1) indicates the desired frequency and Marker 2 (m2) indicates the third order product. (a) and (b) are under -10 dBm incidence, corresponds to low power state (diodes not triggered). (c) and (d) are under 3 dBm incidence, that is when the highest nonreciprocity occurs. (e) and (f) are under 10 dBm incidence when the diodes are triggered for both incident directions. The results show that the IM3s are at least 15 dB smaller than the fundamental frequency.

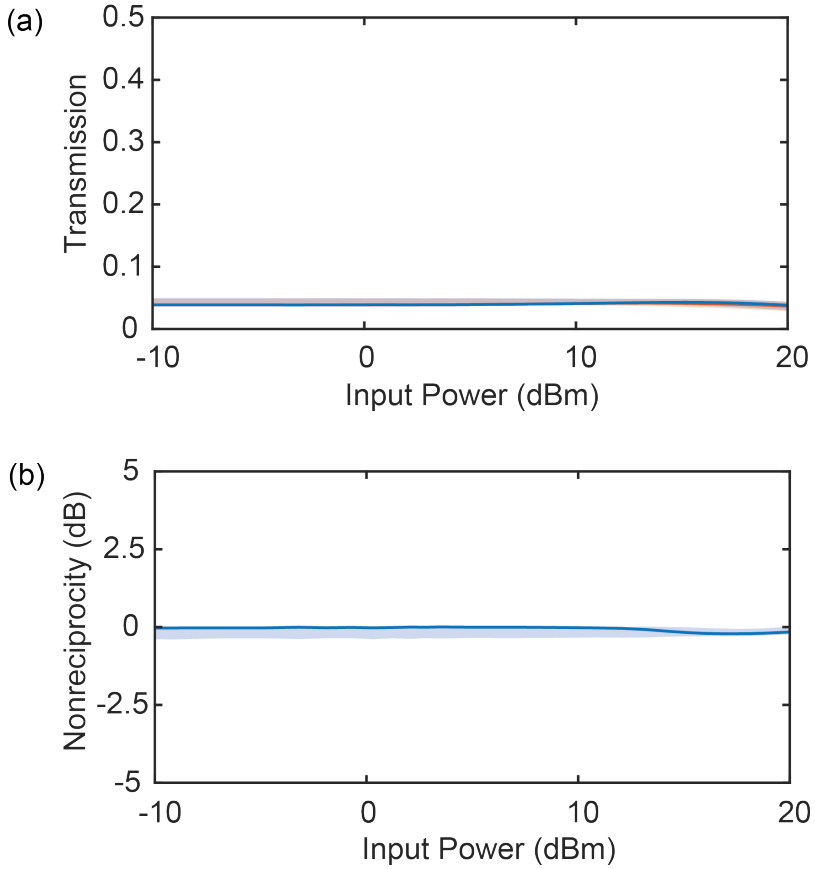

Figure 4.8. Transmission for orthogonal polarization. (a) The simulated transmission rate under different propagation directions. (b) The simulated nonreciprocity. Solid line: 2.21 GHz. Shaded area: 2.18 GHz to 2.25 GHz.

This design is completely linear under low power incidence (diodes are not triggered), slightly nonlinear in the high-power state after the diodes are triggered, and it is strongly nonlinear when the diodes are just triggered. While the nonlinearity for the amplifiers is weak, the proposed structure is strongly nonlinear when the diodes are just triggered since the nonlinearity of the diodes is magnified by the geometry change of the microstrip line. In addition, the design does not have an expected gain. Thus, the 1-dB compression definition might not apply perfectly. We only define the 1-dB compression point for the high-power state (after the diodes are triggered). Here, the 1-dB compression point is defined by fitting a straight line to the high power state as shown in Fig.4.12, and we studied when the output power dropped by 1 dB comparing to the fitted line. The defined 1-dB compression point for forward and backward propagation is 6

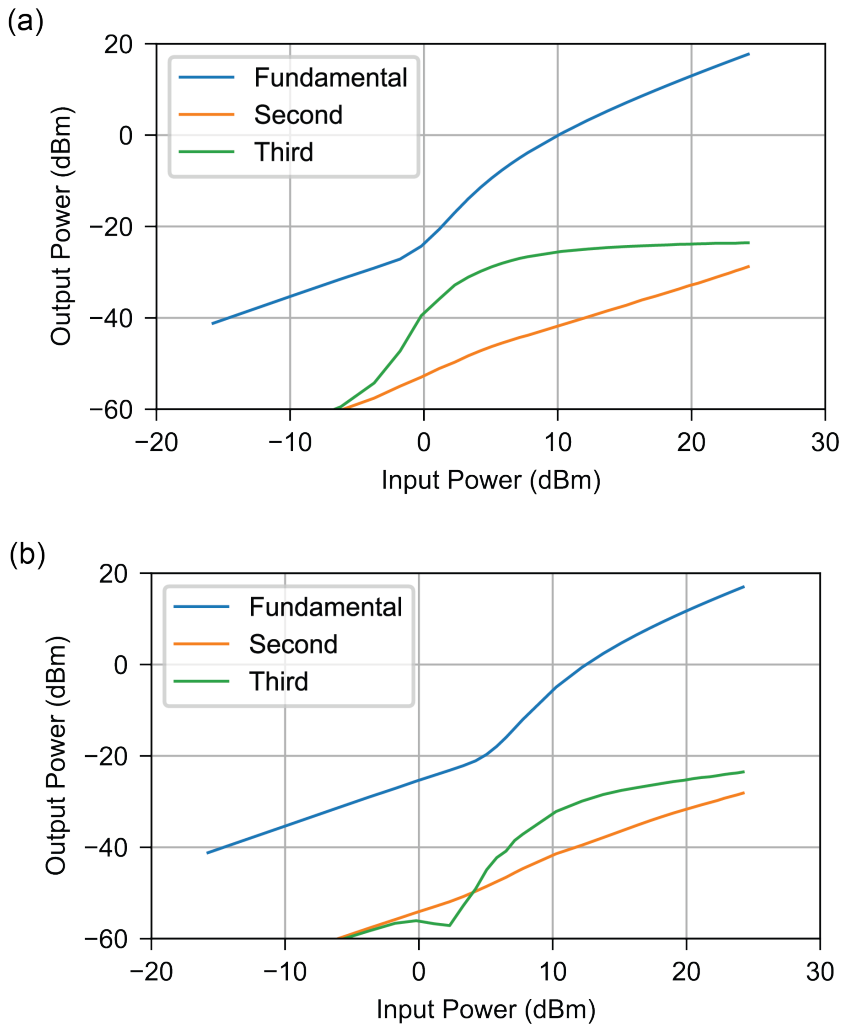

Figure 4.9. Harmonics under single-tone simulation with different incident power. (a) Forward propagation. (b) Backwar propagation.

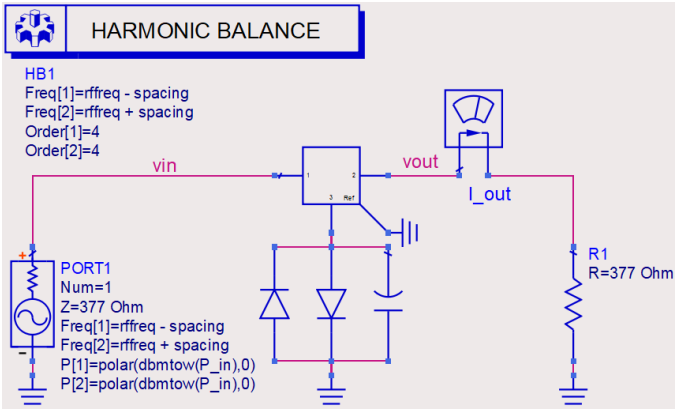

Figure 4.10. Two-tone simulation setup in ADS. rffreq=2.21 GHz, spacing= 10 MHz.

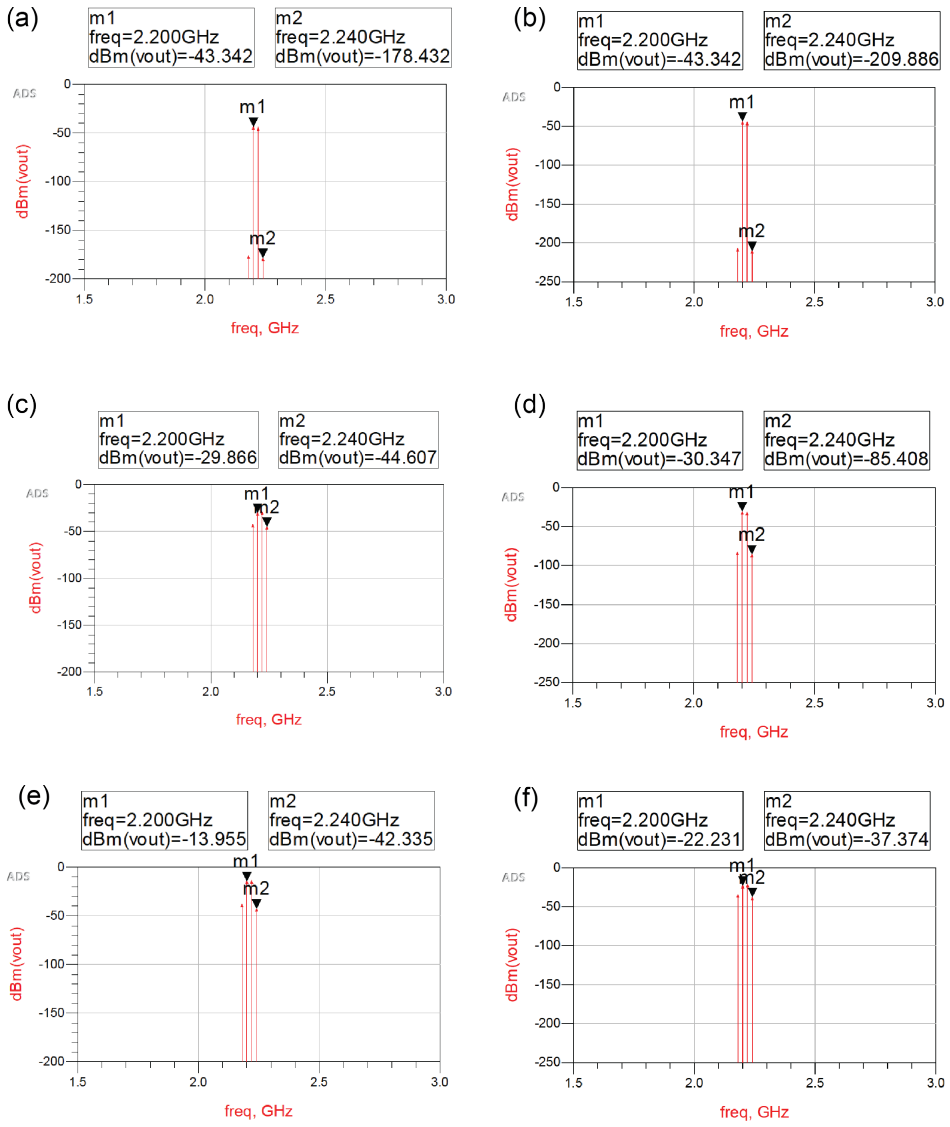

Figure 4.11. Third-intermodulation product. (a) and (b): Forward and backward propagation with $P_{in} = -10$ dBm. (c) and (d): Forward and backward propagation with $P_{in} = 3$ dBm. (r) and (f): Forward and backward propagation with $P_{in} = 10$ dBm.

dBm and 12 dBm, respectively, and it is outside of the 10 dB nonreciprocity range. The transfer function of both forward and backward propagation is ideally similar to a step function versus input power (if the diodes are ideal), but with a shift in input power. The 10 dB nonreciprocity range starts after the diodes are already well triggered for forward incidence (in high power state, the structure is slightly nonlinear), while the backward direction is just about to trigger the diode (low power state, the structure is linear). Thus, not much compression is observed within the 10

dB nonreciprocity range.

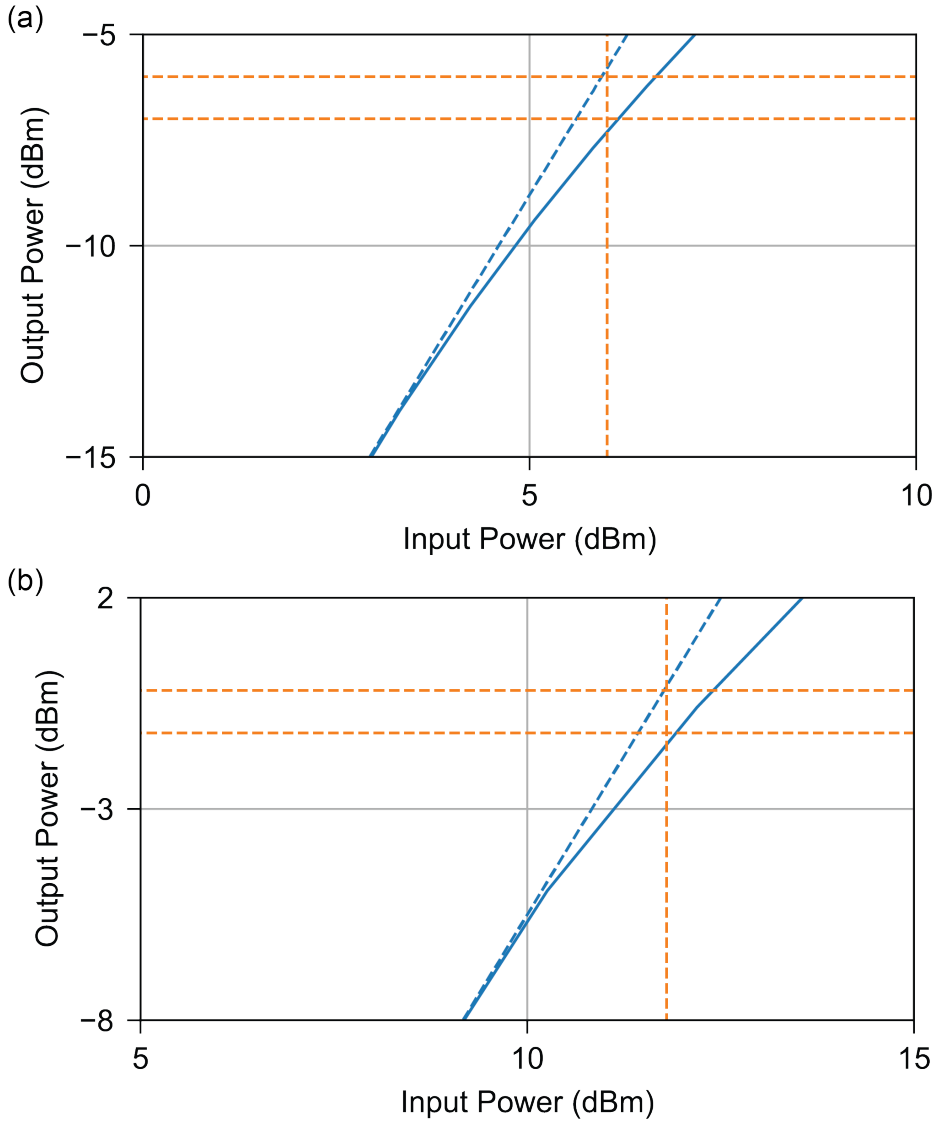

Figure 4.12. Fitted 1 **dB compression point.** (a) Forward propagation. (b) Backward propagation.

This chapter is based on the following paper: Yang, X., Wen, E., & Sievenpiper, D. F. (2023). "All-passive microwave-diode nonreciprocal metasurface." *Communications Physics*, 6(1), 333. The dissertation author was the primary investigator and author of this paper.

Chapter 5

Multifunctional Reconfigurable Metasurface

A metasurface (sometimes called a reflectarray/transmitarray if the unit cell is composed of common antenna designs), the two-dimensional (2-D) counterpart of a metamaterial, exhibits unprecedented abilities of wave manipulation such as polarization conversion, beam steering and phase control [3, 87]. Besides, compared to a 3-D metamterial, its low-profile, low-cost and easy fabrication features make it more appealing. It has aroused wide attention from the microwave regime, to the terahertz and optical ranges for its promising applications in wireless systems to improve robustness and efficiency of communication between the transmitter and receiver, especially for modern ultra-compact electronic systems which are usually linearly-polarized [88, 89]. The polarization mismatch can be alleviated by polarization conversion to match with the polarization of the direct path. By beam steering, the maximum amount of power is redirected to the receiver [90]. The reflected beam of a reflective metasurface can constructively combine with direct path by phase matching. In addition to that, such a surface can be a useful attachment to the stop sign, for retro-reflecting the signal back to radar, the polarization change would enable detection of the stop sign in the crowded reflection from the rest of the environment [91]. Except for polarization conversion and beam steering, another function, adding a phase offset, is potentially useful to be integrated to multifunctional reconfigurable metasurfaces. This function enables phase manipulation of the reflected beam, such that a spatial hot/cold spot could

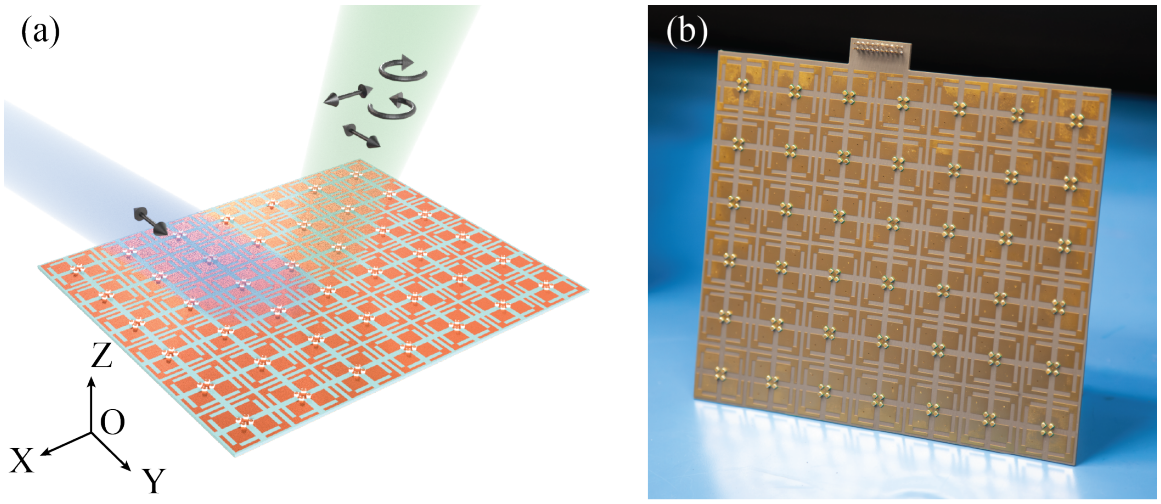

Figure 5.1. The proposed simultaneous multifunctional metasurface. (a) Illustration of the proposed design. Blue beam: incident wave. Green beam: outgoing beam. (b) A picture of the prototype.

be created when using more than one metasurface to cancel or enhance the local field. Recent research on smart surface enabled multiple-input and multiple-output (MIMO) requires phase manipulation on the reflected beam to provide a MIMO spatial multiplexing gain [90, 92]. We believe developing a metasurface with simultaneous polarization, beam steering and phase offset can find many applications in wireless communication systems.

Conventional passive metasurfaces are only capable of one specific polarization conversion function [93, 94, 5, 95, 96, 97, 98, 99]. It is also noticed that the polarization conversion is not optional, which hinders their applications in the real world. Studies on reconfigurable metasurfaces [100, 101, 102, 103, 104, 105] address this issue by integrating nonlinear components or materials to increase the versatility. However, previous research on varactor-based metasurfaces have only realized some of the functions [106, 107]. Other research on transmitarrays and reflectarrays use diodes to switch between different polarizations and phase delays [108, 109, 110]. Limited by the 1-bit phase resolution, it is challenging to achieve complete phase offset and it requires a large surface to achieve an accurate steering angle. Using a phase shifter (especially a discrete-phase shifter) also has this issue. In addition, adopting varactors can broaden the working bandwidth since the capacitance of the structure is tunable.

In this communication, we propose the first multifunctional reflective metasurface, as illustrated in Fig.5.1, with simultaneous beam steering, polarization conversion including X/Y polarization (XP/YP) to XP/YP/left-hand circular polarization (LHCP)/right-hand circular polarization (RHCP) conversion, and complete phase offset range from -180° to 180° by adopting biased varactors. A unit cell which responds to the two orthogonal linear-polarized components of the incident wave is designed. Deploying varactors allows phase manipulation on the orthogonal components to achieve polarization conversion within unit cells. An overall phase shift across adjacent unit cells enables beam steering. The phase offset is realized by assigning different initial phase values to the first column of unit cells.

5.1 Unit Cell Design and Simulation Results

5.1.1 Unit Cell Design and Mechanism

Any linear polarization (LP) can be decomposed into two orthogonal LPs, take y-polarized wave as an example,

$$\hat{y}Ee^{j\phi_0} = \frac{\hat{x}+\hat{y}}{\sqrt{2}}\frac{E}{\sqrt{2}}e^{j\phi_1} + \frac{\hat{y}-\hat{x}}{\sqrt{2}}\frac{E}{\sqrt{2}}e^{j\phi_2}, \tag{5.1}$$

where $\phi_{1,2} = \phi_0$. If the phase of the orthogonal components can be manipulated properly, polarization conversion is achieved. LP to LP/circular polarization (CP)/cross-linear polarization (C-LP) conversion is realized by simply adding on an extra phase delay to the components in Eqn.(5.1) when $\phi_1 - \phi_2 = 0^\circ/\pm 90^\circ/\pm 180^\circ$, otherwise, LP to elliptical polarization conversion.

To realize this, we first design a unit cell structure which naturally decomposes the XP/YP to two orthogonal components with independent electromagnetic response. As illustrated in Fig.5.2 (a) to (c), the unit consists of four identical arrow-shape patches with ungrounded vias underneath and a grounded square island at the center. The slots on the patch are designed to shrink the electrical size for the resonance. The locations of the ungrounded vias are chosen to be the nulls of the field distribution, so that the vias do not interfere with the resonance and this also prevents the RF leakage to the biasing system, which makes it reasonable to neglect the

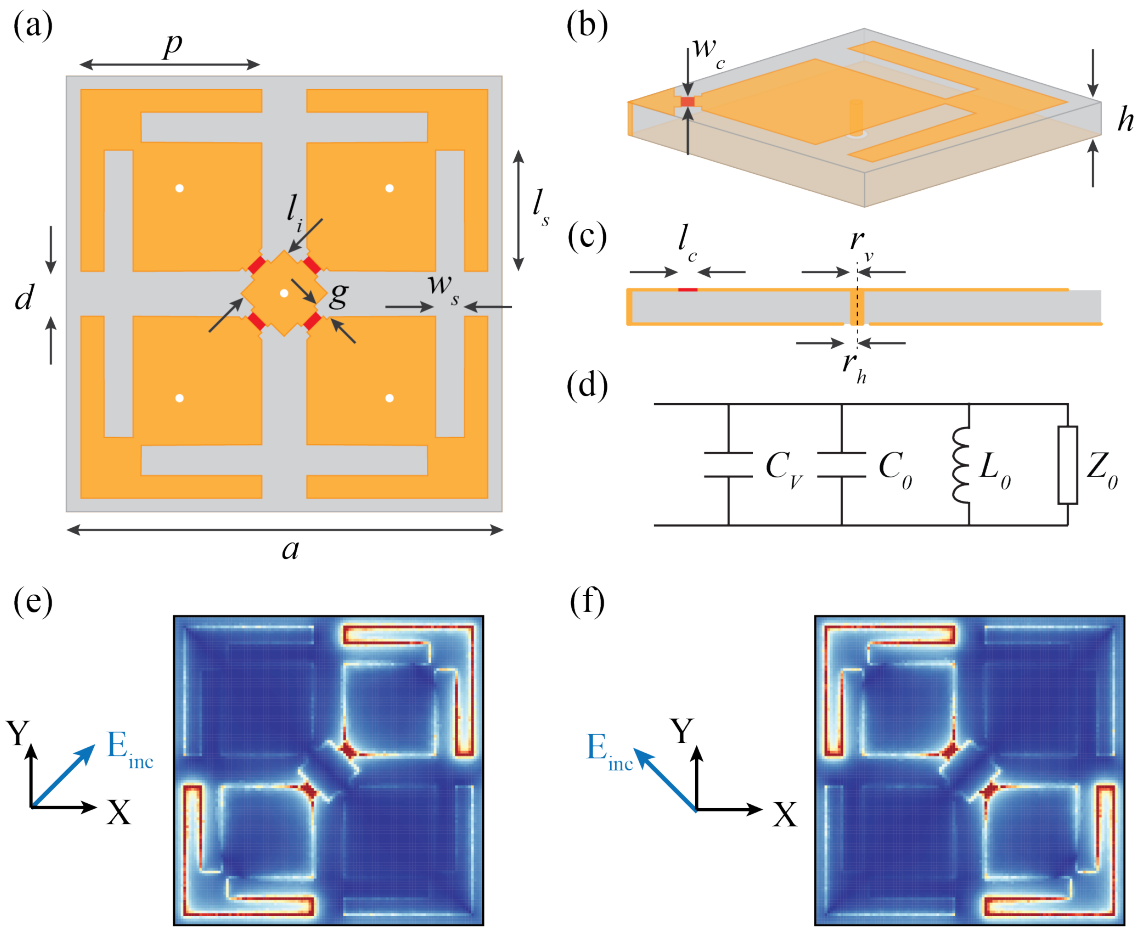

Figure 5.2. Unit cell illustration and simulated results. (a) Top view of the unit cell. (b) and (c) Side view of a quarter unit cell. (d) Equivalent circuit of a quarter-cell with a varactor. Substrate: Duroid Rogers 5880. (e) and (f): field distribution under two orthogonal incident, respectively. $a = 29$ mm, $p = 12$ mm, $d = 3$ mm, $g = 1.2$ mm, $h = 1.575$ mm, $l_i = 4$ mm, $w_s = 2$ mm, $l_s = 8$ mm, $w_c = 1.2$ mm, $l_c = 0.58$ mm, $r_v = 0.25$ mm, $r_h = 0.50$ mm.

biasing network in the simulations. When illuminated by a Y-polarized electric field, the patches on the two diagonals react independently to the orthogonal components of the incident wave, as shown in Fig.5.2 (e) and (f), demonstrating its capability to respectively modify the reflection phase of the orthogonal field components.

Reflection phase manipulation of this design relies on varactors, illustrated as the red rectangles in Fig.5.2 (a). Four varactors are applied in parallel to the metal patches across the gap between patches and the central island, creating an equivalent circuit shown in (d) for one

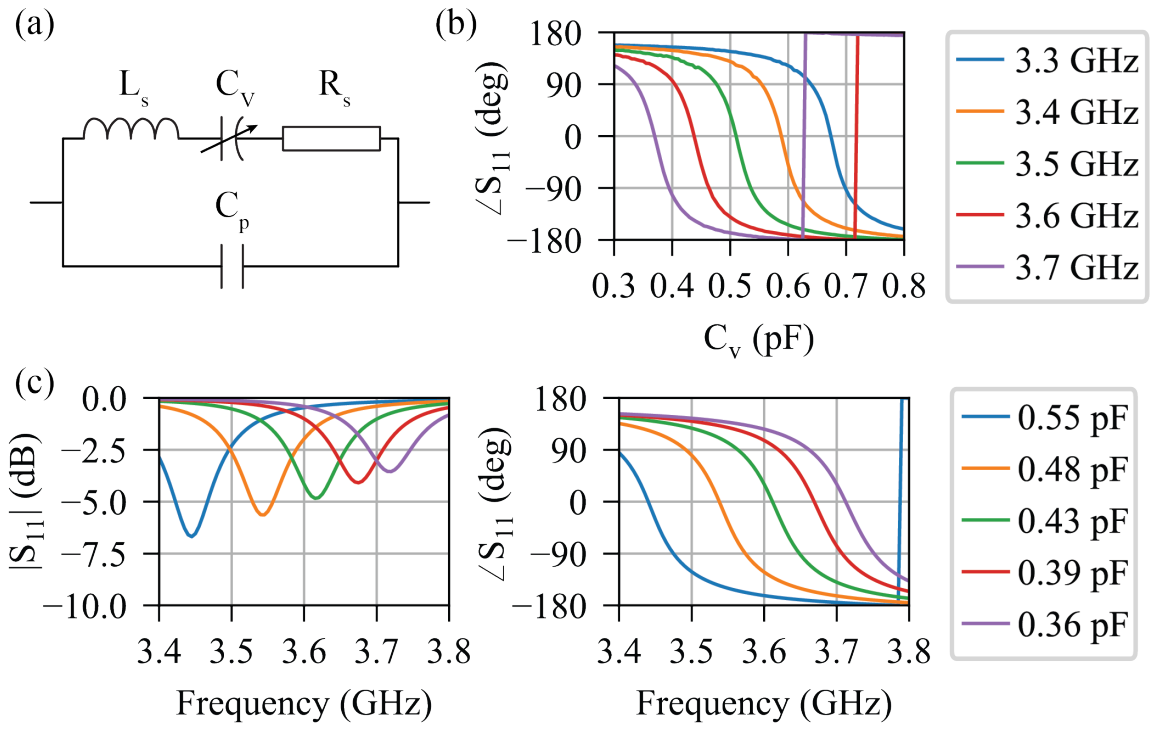

Figure 5.3. The simulated reflection phase and magnitude of the unit cell. The equivalent circuit model of the packaged varactor (MA46H070-1056) is used in simulations. (a) The equivalent circuit of the packaged varactor, where C_v is the junction capacitance, $L_s = 0.45$ nH, $C_p = 0.05$ pF, $R_s = 1.8\ \Omega$. (b) Simulated reflection phase as a function of C_v. (c) The simulated reflection magnitude and phase using the equivalent circuit in (a). $0.55, 0.48, 0.43, 0.39, 0.36$ pF corresponds to $3.0, 4.0, 5.0, 6.0, 7.0$ V biasing, respectively.

quarter of the unit. The resonating frequency is determined by

$$f_0 = \frac{1}{2\pi}\sqrt{\frac{1}{L_0(C_0+C_v)}}, \tag{5.2}$$

where L_0 and C_0 is the intrinsic inductance and capacitance of the patch, and C_v is the capacitance introduced by a varactor. When applying different voltage through the ungrounded vias, a frequency shift on f_0 occurs, resulting in a reflection phase change. The Q factor is actually a very important part of the design. If the Q is too narrow, the bandwidth of any steering or polarization conversion effects will also be narrow, and losses will also be higher near resonance. However, if it is too broad, then the varactor tuning range may not be sufficient to provide the

full phase range. Thus there is a tradeoff between these effects which must be incorporated into the design. Fortunately, the Q factor can be controlled in most metasurface designs through the thickness, with thicker substrate generally providing lower Q for a given resonance frequency. The height of the substrate is chosen to be 1.575 mm to achieve full phase range. To study the reflection phase, all varactors are assigned with the same C_v in the unit cell simulation with periodic boundaries, and the results are shown in Fig.5.3 (b) to (d). According to the datasheet, the packaged varactors are represented by the equivalent circuit model in Fig.5.3 (a) in the simulations. A complete reflection phase range from -180° to 180° is observed from 3.3 GHz to 3.7 GHz within the varactors capacitance range under normal incidence for XP/YP.

Beam steering is realized by a phase difference across adjacent units. An external phase difference $\Delta\phi_e$ should be added on to the next neighboring unit while maintaining the internal phase difference $\Delta\phi_i$ ($0^\circ/\pm 90^\circ/\pm 180^\circ$ for XP to XP/CP/YP conversion) between the two diagonals for simultaneous beam steering and polarization conversion.

There are numerous combinations of reflection phases that result in the same steer angle and polarization conversion, since the phase of the first unit cell (referred to as the initial phase ϕ_0 in this paper), is free of choice from -180° to 180°, which gives the third function of the proposed structure: phase offset. As ϕ_0's range is complete, the phase of the outgoing beam is also complete from -180° to 180°.

5.1.2 Extending to Metasurface

TThe unit cell is then extended to a 7 by 6 unit metasurface, as shown in Fig.3.1 (a), to prove its simultaneous multifunctional capability in driven modal simulations. For simplicity, each column of the surface is assigned with the same capacitance to achieve 1-D steering in the XOZ plane. In Fig.5.4, all results are obtained using $\phi_0 = 150^\circ$ and the design frequency is 3.6 GHz, using the red curve in Fig.5.2 (b). The black dashed line represents the ideal directivity for an equal size PEC sheet. A loss around 4 dB is observed for all cases, which agrees with the simulated loss of a unit cell in Fig.5.2 (c). Note that all units with 0° steering share the same

reflection phase (150°) far away from the resonance, resulting in lower loss.

The simulated phase offset by varying ϕ_0 is illustrated in Fig.5.5. The simulated phase offset $\phi_{rE}^{Simu.}$ is defined by the phase of the radiated far field,

$$rE = |rE|e^{\phi_{rE}^{Simu.}}. \tag{5.3}$$

The ideal phase offset if calculated by

$$\phi_{rE}^{Ideal} = \phi_{rE}^{Simu.}(\phi_0 = -180^\circ) + \phi_0, \tag{5.4}$$

which assumes that any variation in ϕ_0 results in the same amount of variation in the phase of the radiated far field. Due to the imperfect choice of capacitance, a phase error between $\phi_{rE}^{Simu.}$ and ϕ_{rE}^{Ideal} occurs. A $\pm 10^\circ$ accuracy is observed for the main beam direction, and the phase variation for $\pm 5^\circ$ around the main beam is $\pm 20^\circ$.

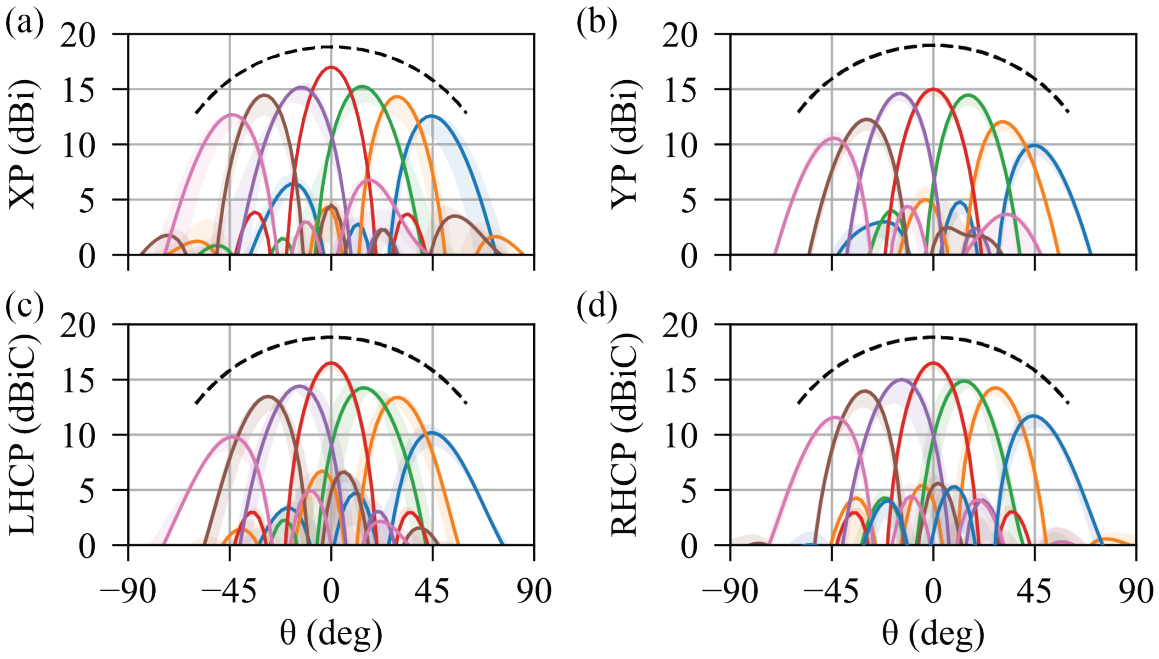

Figure 5.4. Simulated pattern for the 7 by 6-unit metasurface design under normal *y*-polarized incidence. The design frequency is 3.6 GHz with $\phi_0 = 150^\circ$. Solid line: 3.6 GHz, shaded area:3.58 GHz to 3.63 GHz. (a)-(d): XP to XP/YP/LHCP/RHCP conversion.

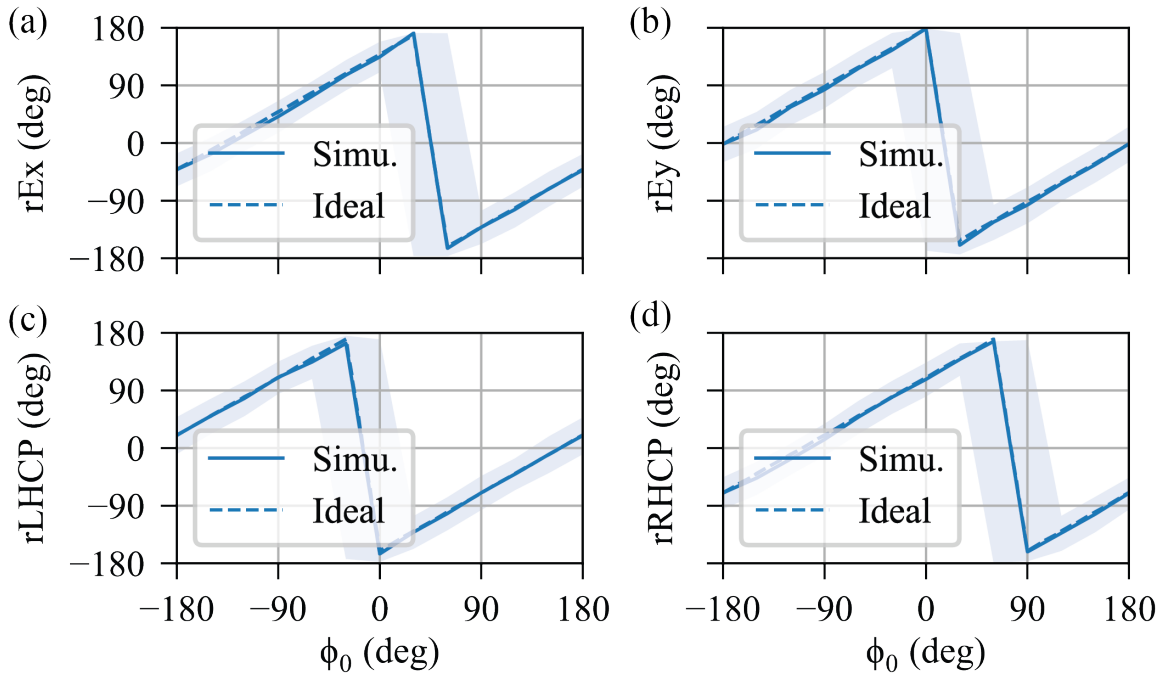

Figure 5.5. The phase offset added to the reflected beam with various ϕ_0, for 30° steering at 3.6 GHz. Solid line: main beam direction, shaded area: ±5° of the main beam. (a)-(d): XP to XP/YP/LHCP/RHCP conversion.

5.2 Measurement and Results

5.2.1 Fabrication and Measurement Setup

After numerical validations for the proposed structure, a varactor-loaded, four-layer, 7 by 6-unit 1-D surface is manufactured as shown in Fig.3.1 (b). The top two layers are the varactor-integrated patches and the ground plane, respectively. Underneath is a double-layer DC biasing network, as shown in Fig.5.6 (a). Each unit has two biasing channels, corresponding to the patches on the two diagonals, and the units on each column are connected together, resulting in 14 DC channels, as illustrated in Fig.5.6 (b).

The experiment setup for all measurements is shown in Fig.5.7. The surface under test (SUT) and the transmitter (Tx) rotate together in azimuth. The surface is biased by a data acquisition device (DAQ, NI PXIe-1062Q). The Tx and receiver (Rx) are identical dual-polarization (XP and YP) horn antennas (RCDLPHA2G18B) and thus can be used to measure

the polarization conversion. Using the vector network analyzer (VNA, E5071C) to excite XP, the incident wave is reflected by the SUT and then collected Rx to measure the XP to XP (S_{xx}) and XP to YP conversion (S_{yx}).

Three sets of data, with/without SUT and an equal size metal sheet case (aluminum, PEC case), is collected for both the reflection phase and the pattern measurement. The PEC case is used as a baseline study to observe the maximum power that the SUT is able to reflect if lossless. By measuring the blank (BLK) case (without SUT), the data contains all the reflections from the background and the direct talk between Tx and Rx. Thus, subtracting the blank case data from that of the SUT case eliminates environmental signals. Time-gating technique is also applied to further filter out the reflected signal from the SUT.

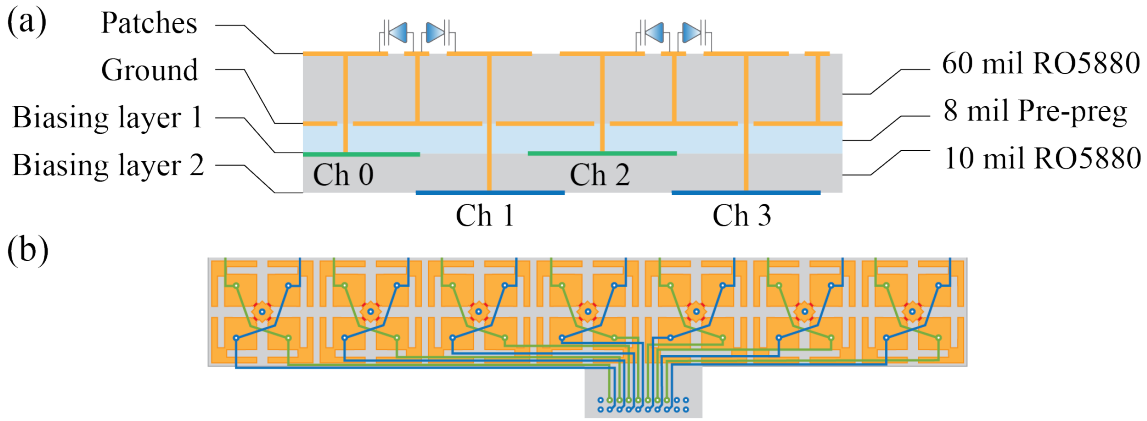

Figure 5.6. The stack-up info. (a) The stack-up illustration including the biasing layers. (b) Illustration of biasing line arrangement. The green and blue copper lines are located on biasing layer 1 and 2, respectively.

5.2.2 Measurement Results

Before examining the ability of wave manipulation, we first measure the reflection phase of the surface under different biasing voltage. All channels are biased with the same voltage under normal incidence and the motor at $\theta = 0°$, as in Fig.5.7. Since polarization conversion is absent in this measurement, S_{xx} for the SUT/BLK/PEC cases measures the loss and reflection

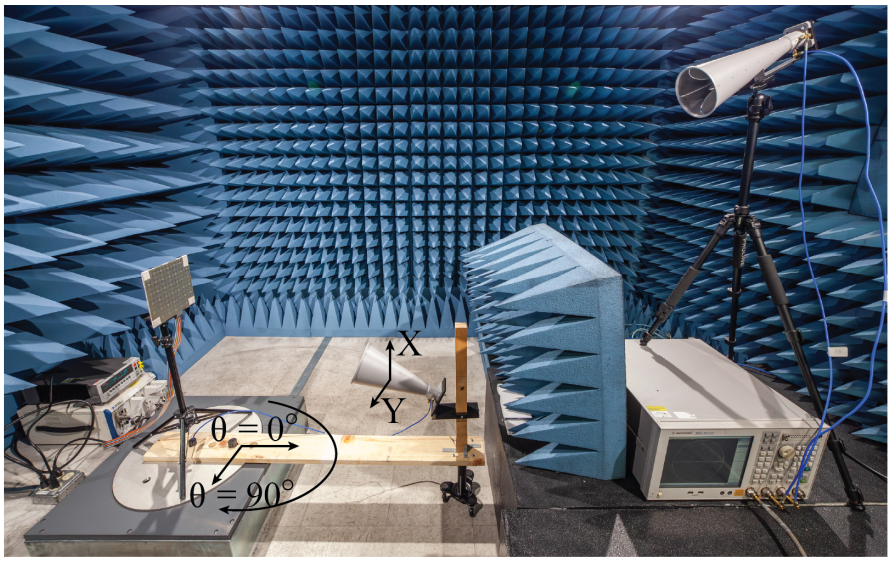

Figure 5.7. Experiment setup. θ denotes the rotation angle of the Tx. X and Y indicate the direction of XP and YP.

phase of the metasurface. The calibrated S parameter of the surface is determined by

$$S_{xx,yx}^{SUT,cal}(f,u) = \frac{S_{xx,yx}^{SUT}(f,u) - S_{xx,yx}^{BLK}(f,u)}{S_{xx,yx}^{PEC}(f,u) - S_{xx,yx}^{BLK}(f,u)}, \tag{5.5}$$

where f and u denotes the frequency and biasing voltage for all channels, respectively. All results presented below are time-gated and calibrated using the Eqn.(5.5). Since the equal size PEC case can be considered as lossless, after subtracting the environmental noises, dividing the SUT by the PEC case directly indicates the loss (δ) and deembedded reflection phase (ϕ) of the metasurface,

$$S_{xx}^{SUT,cal}(f,u) = \delta(f,u)e^{j\phi(f,u)} \tag{5.6}$$

A complete phase range from -180° to 180° is observed in Fig.5.8 (a), demonstrating the tuning bandwidth of the metasurface covers from 3.3 GHz to 3.7 GHz. As depicted in Fig.5.8 (b), δ decreases as biasing voltage increases, because the varactors are more lossy at higher capacitance. In agreement with the simulated unit cell reflection phase and loss, the maximum loss around 3.6 GHz is approximately 4 dB, which is reasonable compared to existing work [105]-[107, 111].

Even at the lower frequency end, higher loss only occurs when all units are working at the resonant bias voltage, which does not happen when polarization conversion and beam steering are active, since units are not assigned with the same biasing that happen to maximize this loss. Even if none of the functions are active, this maximum loss scenario can still be avoided by choosing off-resonance biasing.

The look-up table between biasing voltage and reflection phase in Fig.5.8 (a) is used to design the biasing voltages for simultaneous beam steering, polarization conversion and phase offset. Here, we verify its performance by showing the results at 3.6 GHz in Fig.5.9. Although the data only records S_{xx} and S_{yx}, the calibrated S parameter between XP to RHCP/LHCP can be reconstructed by

$$S_{rx,lx}^{SUT,cal} = \frac{S_{xx}^{SUT,cal} \pm iS_{yx}^{SUT,cal}}{\sqrt{2}}. \tag{5.7}$$

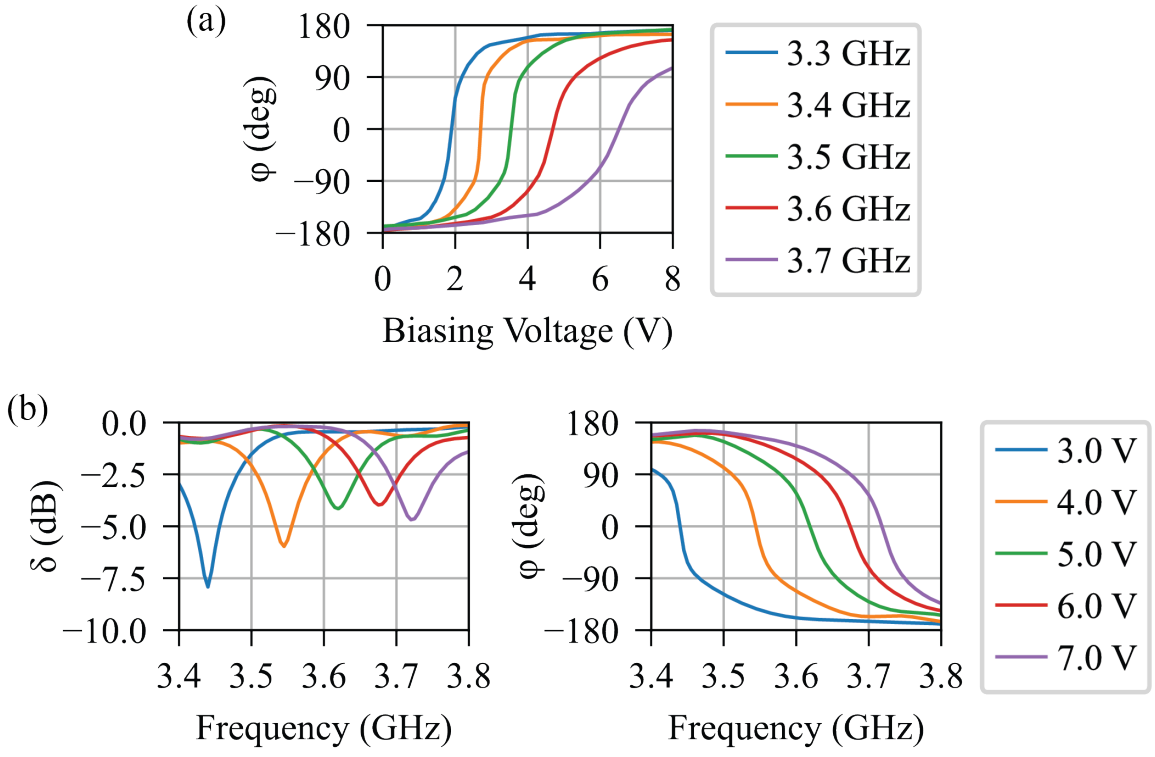

Figure 5.8. Measured S parameter of the metasurface after time-gating and calibration. (a) The mapping between biasing voltage and reflection phase. (b) Loss and reflection phase of the surface.

To convert these S parameter into directivity, we calculated the directivity of PEC using $D^{PEC} = \frac{4\pi}{\lambda^2}S = 18.0$ dBi/dBiC. Then, a relationship between $S^{SUT,cal}$ and directivity D^{SUT} is established by $D^{SUT} = 20log_{10}|S^{SUT,cal}| + D^{PEC}$. The results for four polarization conversion scenarios with different steering angles are shown in Fig.5.9. Similar to the simulation results, a cosine envelope with around 4 dB loss is observed across various steering angle. For XP to YP conversion, the difference between the diagonal components has to be 180°. Thus, it has a higher chance to fall around the resonance (which has higher loss) according to Fig.5.8, resulting in general slightly higher loss than XP to XP/LHCP/RHCP conversion. The nulls in the pattern are filled in due to a 15.5° quadratic phase error. However, its impact on the overall pattern is negligible.

Another metric for polarization conversion is polarization conversion rate (PCR), which is defined by

$$PCR_{xx} = \frac{(S_{xx}^{SUT,cal})^2}{(S_{xx}^{SUT,cal})^2 + (S_{yx}^{SUT,cal})^2}, \tag{5.8}$$

$$PCR_{yx} = \frac{(S_{yx}^{SUT,cal})^2}{(S_{xx}^{SUT,cal})^2 + (S_{yx}^{SUT,cal})^2}, \tag{5.9}$$

$PCR_{rx,lx}$ are defined similarly. The measured PCR for different polarization conversions are shown in Fig.5.10. The PCR at the designed frequency is above 0.9 for almost all scenarios, except 45° steering LP to LHCP, and −45° steering LP to RHCP conversion. Note that this is not because of the large steering angle or conversion to CP, since −45° steering LP to LHCP, and 45° steering LP to RHCP conversion both show PCR above 0.9. It happens due to the discrepancies among non-ideal varactors: the accuracy gets worse for certain cases involving more elements working around the resonant frequency. This could be improved by a fine capacitance tuning of each channel, or using real-data driven machine learning techniques to study the relationship between biasing voltage and reflection phase [111]. However, this is beyond the scope of this paper.

By sweeping the initial phase ϕ_0 from −180° to 180°, the phase of the outgoing beam

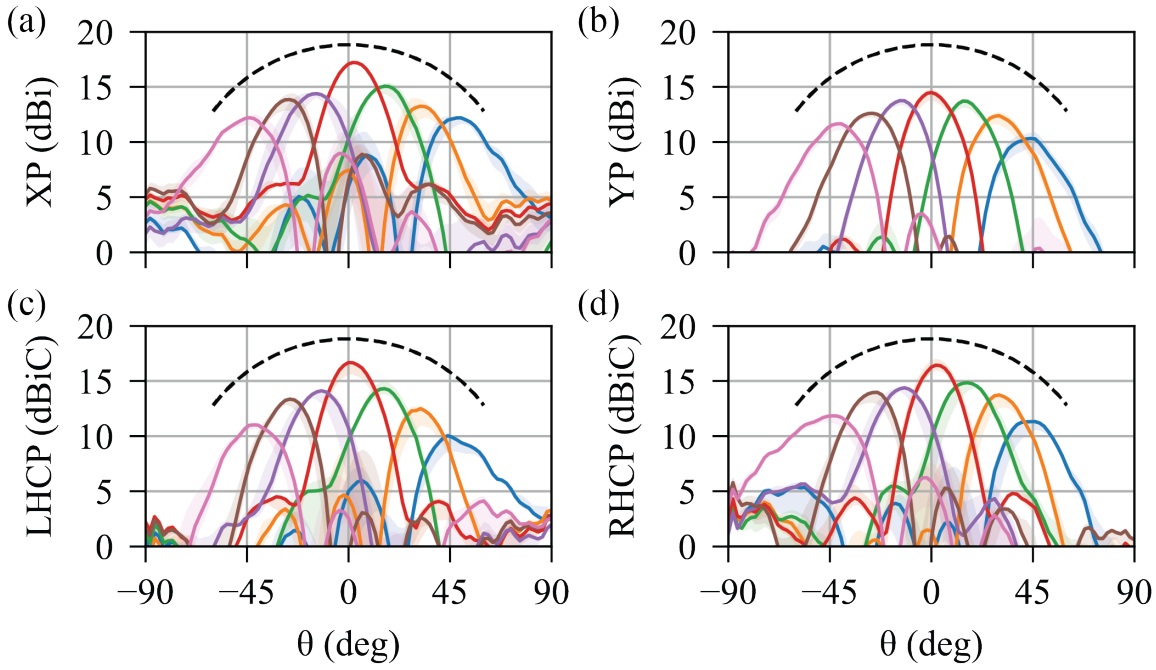

Figure 5.9. Measured pattern for different polarization conversion and steering angle. The reflection phase look-up table in Fig.5.8 (c) is used to design the pattern. (a)-(d): XP to XP/YP/LHCP/RHCP conversion. Solid line: 3.6 GHz, shaded area: 1 dB bandwidth, 3.58 GHz to 3.63 GHz.

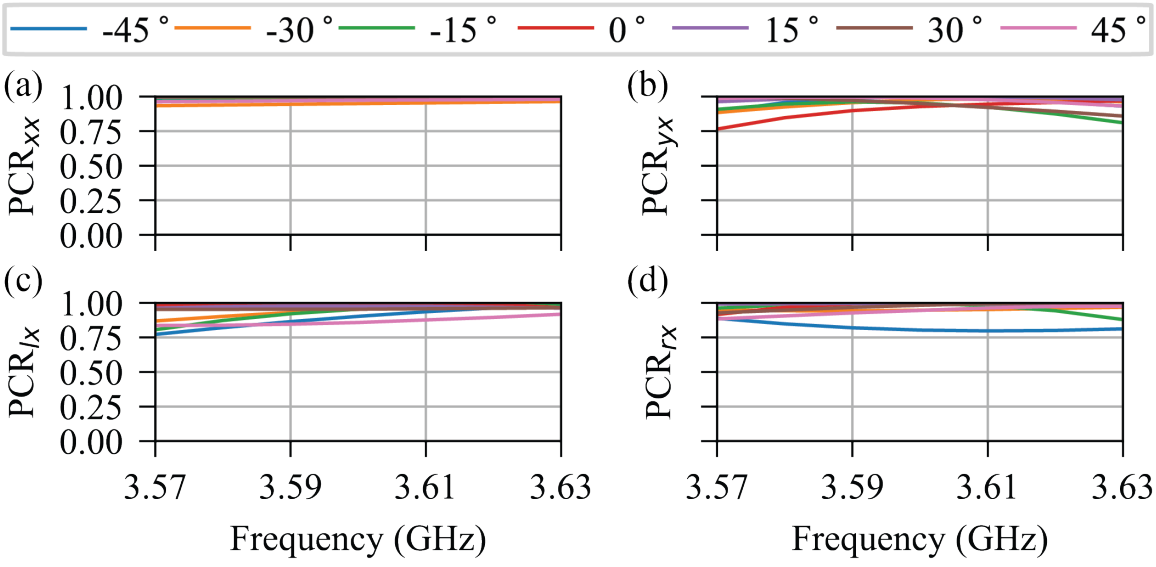

Figure 5.10. The measured PCR for four polarization conversion scenarios with different steering angle from $-45°$ **to** $45°$**.** The design frequency is 3.6 GHz. (a)-(d): PCR for XP to XP/YP/LHCP/RHCP conversion.

varies accordingly from -180° to 180°. Fig.5.11 illustrates an example of the measured and ideal phase offset with 30° steering for four polarization conversion scenarios. The phase offset in the measurement is defined by

$$\phi_{Rx}^{Meas.} = \text{ang}(S^{SUT,cal}), \tag{5.10}$$

and the ideal phase is plotted by

$$\phi_{Rx}^{Ideal} = \phi_{Rx}^{Meas.}(\phi_0 = -180^\circ, f = 3.6\,GHz) + \phi_0. \tag{5.11}$$

A phase error between ϕ_{Rx}^{Ideal} and $\phi_{Rx}^{Meas.}$ ranges within $\pm 20^\circ$ for all polarization conversions at the main lobe directions. This error could also be improved by the techniques mentioned above.

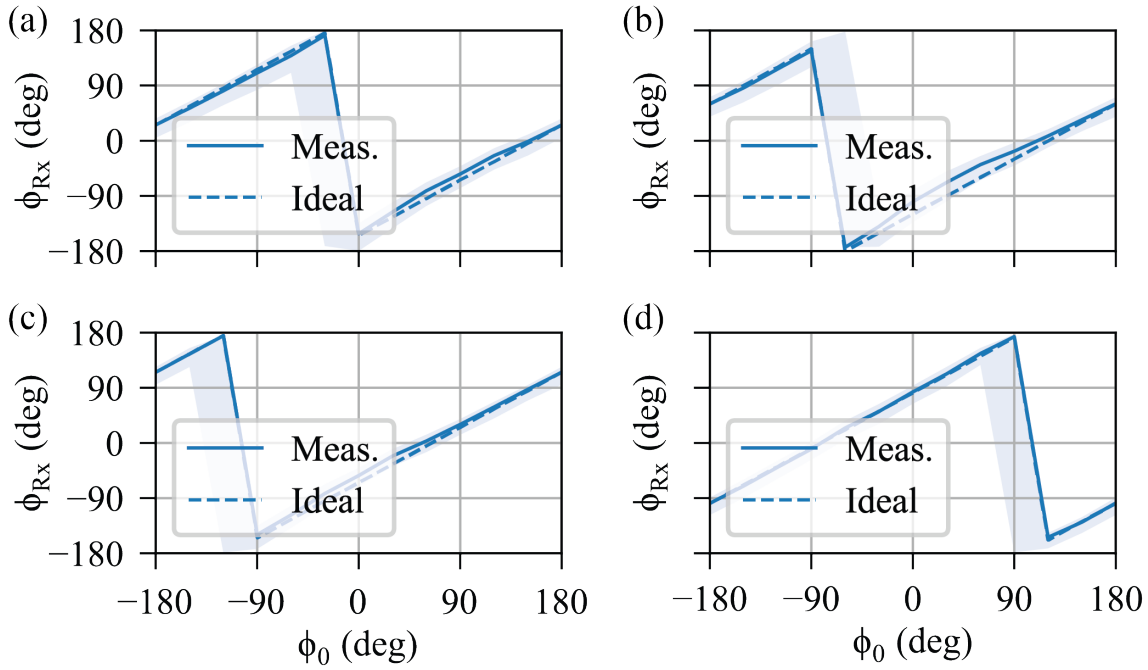

Figure 5.11. The measured phase offset at the main lobe direction. The results are derived by changing the initial phase assigned to the first column of the surface, with a 30° steering angle. (a)-(d): XP to XP/YP/LHCP/RHCP conversion. Solid line: at the main lobe direction. Shaded area: $\pm 5^\circ$ of the main lobe direction.

5.3 Conclusion

A four-layer varactor-based multifunctional metasurface for simultaneous beam steering, polarization conversion and phase offset is proposed and experimentally demonstrated. The incident XP is naturally decomposed by the metallic patches into two orthogonal LPs, whose reflection phase is controlled by the loaded biased varactor. Unlike the N-bit p-i-n diode approach, which is limited by the states of the diodes, this method is capable of continuous phase offset from 180° to 180°. Although neglecting the differences between varactors and using the overall reflection phase of the whole surface as that of a unit cell, more than 0.9 PCR is observed for almost all polarization conversion scenarios. XP to XP/YP/RHCP/LHCP conversion with $-45°$ to 45° steering and a $\pm 20°$ error of phase offset at the main beam direction is achieved. The bandwidth covers from 3.3 GHz to 3.7 GHz, while once a combination of biasing voltages is chosen, the 1 dB bandwidth is 50 MHz. We believe the proposed metasurface can find many applications in wave manipulation and increasing communication efficiency.

This chapter is based on the following manuscript to be published: Yang, X., Wen, E., Bharadia, D., & Sievenpiper, D. F. (2024). "Multifunctional Metasurface: Simultaneous Beam Steering, Polarization Conversion and Phase Offset." *IEEE Transactions on Antennas and Propagation*, 72(5), 4589 - 4593. The dissertation author was the primary investigator and author of this paper.

Chapter 6

Conclusion and Future Work

6.1 Summary of Work

This thesis presents a comprehensive investigation on the performance and advantages of non-LTI and reconfigurable metasurfaces compared to conventional passive metasurfaces through analysis, simulation and experiment. By loading nonlinear devices and applying time-modulation, the metasurfaces exhibit enhanced performance in multifunction and promising ability to achieve power-dependent transmission, ultra-wide bandwidth and nonreciprocity that LTI metasurfaces are not capable of.

Chapter 1 reviews the background and applications of metasurfaces, and explains the motivation and advantages of integrating electronic components to achieve non-LTI and reconfigurable metasurfaces.

Chapter 2 propose a broadband absorber beyond the Bode-Fano limit by creating an energy trap using time-modulated switch/diodes. This work starts with an ideal circuit model to prove the concept, followed by two EM realizations - a freuqnecy selective surface approach for general bandwidth broadening and a low-profile PCB design. The prototype of the latter is built and measured, demonstrating a Bode-Fano integral larger than one. This approach paves a way to many practical ultra-wide band absorber designs.

Chapter 3 presents a metallic ring based, diode-integrated, low-profile, power-dependent metasurface. The triggering of the diodes directly transforms the structure from a surface wave

supportive state to a self-induced bandgap topology if exposed to high power RF illumination. The concept is demonstrated by EM-circuit co-simulation and measurements for a 6 by 8 unit 2D prototype. Near field scan experiments verify that the proposed topology works in two distinct states, the ON and OFF state, and high-power measurements prove that the reflection varies with the incident signal power. This structure can be used to protect sensitive devices from large signals while otherwise supporting a communication channel for small signals.

Chapter 4 theoretically demonstrates the nonreciprocal behaviour on a transmission line building block creating a strong field asymmetry with a switchable matching stub to enable two distinct working states. After translating to an electromagnetic model, this concept is first proved by simulation and then experimentally verified on a microstrip-line-based diode-integrated metasurface showing nonreciprocal transmission. This printed circuit board design is expected to find various applications in electromagnetic protecting layers, communication systems, microwave isolators and circulators.

Chapter 5 introduces a varactor-based reconfigurable multifunctional metasurface capable of simultaneous beam steering, polarization conversion and phase offset. The unit cell is designed to naturally decompose the incident waves into two equal amplitude orthogonal linear components, and by integrating varactors, the reflection phase of the field components can be engineered from -180° to 180°. Taking advantage of the infinite states of the varactors, this design integrates a new function, the phase offset. After simulation validation of its capability, a four-layer one-dimensional prototype is fabricated as a printed circuit board. It is experimentally demonstrated that it switches between X/Y and circular polarization with more than 0.9 polarization conversion rate, while reaching $\pm 45^\circ$ steering and $\pm 180^\circ$ phase offset.

6.2 Future Work

Non-LTI metasurfaces have the benefits in broadening bandwidth, creating nonreciprocity, enabling power-dependent behaviour and tunability, which conventional metasurfaces cannot

achieve. Meanwhile, the nonlinear components such as diodes and varactors also bring harmonics and loss. Exploring possible approaches to address these issues could enable more applications. However, it could be beneficial to developing broadband absorbers with frequency conversion and higher dielectric loss. Time-modulation strategy is challenging and complex to realize in real-world applications, especially at higher frequencies in optical range. Thus, designing a self-triggered biasing network using active components could avoid modulation and reduce biasing difficulty. It is also possible to apply time-modulation to transmitters and receivers for wideband applications, or create nonreciprocity.

Bibliography

[1] Francesco Monticone and Andrea Alù. Metamaterial, plasmonic and nanophotonic devices. *Reports on Progress in Physics*, 80(3):036401, 2017.

[2] Dan Sievenpiper, Lijun Zhang, Romulo FJ Broas, Nicholas G Alexopolous, and Eli Yablonovitch. High-impedance electromagnetic surfaces with a forbidden frequency band. *IEEE Transactions on Microwave Theory and techniques*, 47(11):2059–2074, 1999.

[3] Aobo Li, Shreya Singh, and Dan Sievenpiper. Metasurfaces and their applications. *Nanophotonics*, 7(6):989–1011, 2018.

[4] Konstantin N Rozanov. Ultimate thickness to bandwidth ratio of radar absorbers. *IEEE Transactions on Antennas and Propagation*, 48(8):1230–1234, 2000.

[5] M Ismail Khan, Zobaria Khalid, and Farooq A Tahir. Linear and circular-polarization conversion in x-band using anisotropic metasurface. *Scientific reports*, 9(1):4552, 2019.

[6] David M Pozar. *Microwave engineering*. John wiley & sons, 2011.

[7] Robert E Collin. *Foundations for microwave engineering*. John Wiley & Sons, 2007.

[8] Constantine A Balanis. *Advanced engineering electromagnetics*. John Wiley & Sons, 1999.

[9] Constantine A Balanis. *Antenna theory: analysis and design*. John wiley & sons, 2015.

[10] Adel S Sedra, Dean Emeritus Adel S Sedra, and Kenneth Carless Smith. *Microelectronic circuits*. New York: Oxford University Press, 1998.

[11] Carlo Kopp. The e-bomb–a weapon of electrical mass destruction. In *Proceedings of the InfoWarCon V Conference*, 1996.

[12] Yanxia Cui, Jun Xu, Kin Hung Fung, Yi Jin, Anil Kumar, Sailing He, and Nicholas X Fang. A thin film broadband absorber based on multi-sized nanoantennas. *Applied Physics Letters*, 99(25):253101, 2011.

[13] Lu Zhu, Yue Jin, Huan Liu, and Yuanyuan Liu. Ultra-broadband absorber based on metal-insulator-metal four-headed arrow nanostructure. *Plasmonics*, 15(6):2153–2159, 2020.

[14] Juan Yang and Zhongxiang Shen. A thin and broadband absorber using double-square loops. *IEEE Antennas and Wireless Propagation Letters*, 6:388–391, 2007.

[15] Binchao Zhang, Cheng Jin, and Zhongxiang Shen. Low-profile broadband absorber based on multimode resistor-embedded metallic strips. *IEEE Transactions on Microwave Theory and Techniques*, 68(3):835–843, 2019.

[16] Lei Lei, Shun Li, Haixuan Huang, Keyu Tao, and Ping Xu. Ultra-broadband absorber from visible to near-infrared using plasmonic metamaterial. *Optics express*, 26(5):5686–5693, 2018.

[17] Jing Liu, Wei Chen, Jia-Chun Zheng, Yu-Shan Chen, and Cheng-Fu Yang. Wide-angle polarization-independent ultra-broadband absorber from visible to infrared. *Nanomaterials*, 10(1):27, 2020.

[18] Jianfei Zhu, Zhaofeng Ma, Wujiong Sun, Fei Ding, Qiong He, Lei Zhou, and Yungui Ma. Ultra-broadband terahertz metamaterial absorber. *Applied Physics Letters*, 105(2):021102, 2014.

[19] Sadegh Biabanifard, Mohammad Biabanifard, Somayyeh Asgari, Shahrouz Asadi, and CE Mustapha. Tunable ultra-wideband terahertz absorber based on graphene disks and ribbons. *Optics Communications*, 427:418–425, 2018.

[20] Xingxing Chen, Hanmo Gong, Shuowei Dai, Ding Zhao, Yuanqing Yang, Qiang Li, and Min Qiu. Near-infrared broadband absorber with film-coupled multilayer nanorods. *Optics letters*, 38(13):2247–2249, 2013.

[21] Hendrik Wade Bode. *Network analysis and feedback amplifier design*. Van Nostrand, 1945.

[22] Robert M Fano. Theoretical limitations on the broadband matching of arbitrary impedances. *Journal of the Franklin Institute*, 249(1):57–83, 1950.

[23] AR Kerr. Some fundamental and practical limits on broadband matching to capacitive devices, and the implications for sis mixer design. *IEEE transactions on microwave theory and techniques*, 43(1):2–13, 1995.

[24] A Ghorbani, MA Ansarizadeh, NJ McEwan, Raed A Abd-alhameed, and D Zhou. The bode-fano integrals as an objective measure of antenna bandwidth reflection coefficient product limit. In *2006 International RF and Microwave Conference*, pages 210–215. IEEE, 2006.

[25] A Ghorbani, Raed A Abd-Alhameed, Neil J McEwan, and Dawei Zhou. An approach for calculating the limiting bandwidth-reflection coefficient product for microstrip patch antennas. *IEEE transactions on antennas and propagation*, 54(4):1328–1331, 2006.

[26] Leonid Brekhovskikh. *Waves in layered media*, volume 16. Elsevier, 2012.

[27] Amir Shlivinski and Yakir Hadad. Beyond the bode-fano bound: Wideband impedance matching for short pulses using temporal switching of transmission-line parameters. *Physical review letters*, 121(20):204301, 2018.

[28] Stephen E Sussman-Fort and Ronald M Rudish. Non-foster impedance matching of electrically-small antennas. *IEEE Transactions on Antennas and Propagation*, 57(8):2230–2241, 2009.

[29] Pai-Yen Chen, Christos Argyropoulos, and Andrea Alù. Broadening the cloaking bandwidth with non-foster metasurfaces. *Physical review letters*, 111(23):233001, 2013.

[30] Ting Shi, Ming-Chun Tang, Zhentian Wu, He-Xiu Xu, and Richard W Ziolkowski. Improved signal-to-noise ratio, bandwidth-enhanced electrically small antenna augmented with internal non-foster elements. *IEEE Transactions on Antennas and Propagation*, 67(4):2763–2768, 2019.

[31] Hengzhen Crystal Jing, Xiaojing Jessie Xu, and Yuanxun Ethan Wang. Direct antenna modulation (dam) with switched patch antenna-performance analysis. *Applied Computational Electromagnetics Society Journal*, 29(5), 2014.

[32] Weijun Yao and Yuanxun Ethan Wang. An integrated antenna for pulse modulation and radiation. In *Proceedings. 2004 IEEE Radio and Wireless Conference (IEEE Cat. No. 04TH8746)*, pages 427–429. IEEE, 2004.

[33] Weijun Yao and Yuanxun Wang. Direct antenna modulation-a promise for ultra-wideband (uwb) transmitting. In *2004 IEEE MTT-S International Microwave Symposium Digest (IEEE Cat. No. 04CH37535)*, volume 2, pages 1273–1276. IEEE, 2004.

[34] Chen Firestein, Amir Shlivinski, and Yakir Hadad. Absorption and scattering by a temporally switched lossy layer: Going beyond the rozanov bound. *arXiv preprint arXiv:2105.01487*, 2021.

[35] Huanan Li and Andrea Alù. Temporal switching to extend the bandwidth of thin absorbers. *Optica*, 8(1):24–29, 2021.

[36] D Correas-Serrano, JS Gomez-Diaz, DL Sounas, Y Hadad, A Alvarez-Melcon, and A Alù. Nonreciprocal graphene devices and antennas based on spatiotemporal modulation. *IEEE Antennas and Wireless Propagation Letters*, 15:1529–1532, 2015.

[37] Aobo Li, Yunbo Li, Jiang Long, Ebrahim Forati, Zhixia Du, and Dan Sievenpiper. Time-moduated nonreciprocal metasurface absorber for surface waves. *Optics Letters*, 45(5):1212–1215, 2020.

[38] Andrew E Cardin, Sinhara R Silva, Shai R Vardeny, Willie J Padilla, Avadh Saxena, Antoinette J Taylor, Wilton JM Kort-Kamp, Hou-Tong Chen, Diego AR Dalvit, and Abul K Azad. Surface-wave-assisted nonreciprocity in spatio-temporally modulated metasurfaces. *Nature communications*, 11(1):1–9, 2020.

[39] GT Ruck and DE Barrick. W. d. stuart, and ck krichbaum. *Radar cross section handbook*, 1:50–59, 1970.

[40] Eugene F Knott. *Radar cross section measurements*. Springer Science & Business Media, 2012.

[41] Winfield W Salisbury. Absorbent body for electromagnetic waves. 1952.

[42] Ben-Xin Wang, Yuanhao He, Pengcheng Lou, and Wenhui Xing. Design of a dual-band terahertz metamaterial absorber using two identical square patches for sensing application. *Nanoscale Advances*, 2(2):763–769, 2020.

[43] N I Landy, S Sajuyigbe, Jack J Mock, David R Smith, and Willie J Padilla. Perfect metamaterial absorber. *Physical review letters*, 100(20):207402, 2008.

[44] Hiroki Wakatsuchi, Sanghoon Kim, Jeremiah J Rushton, and Daniel F Sievenpiper. Circuit-based nonlinear metasurface absorbers for high power surface currents. *Applied Physics Letters*, 102(21):214103, 2013.

[45] Daniel F Sievenpiper. Nonlinear grounded metasurfaces for suppression of high-power pulsed rf currents. *IEEE Antennas and Wireless Propagation Letters*, 10:1516–1519, 2011.

[46] Aobo Li, Sanghoon Kim, Yong Luo, Yunbo Li, Jiang Long, and Daniel F Sievenpiper. High-power transistor-based tunable and switchable metasurface absorber. *IEEE Transactions on Microwave Theory and Techniques*, 65(8):2810–2818, 2017.

[47] Sanghoon Kim, Hiroki Wakatsuchi, Jeremiah J Rushton, and Daniel F Sievenpiper. Switchable nonlinear metasurfaces for absorbing high power surface waves. *Applied Physics Letters*, 108(4):041903, 2016.

[48] Han Xiong and Fan Yang. Ultra-broadband and tunable saline water-based absorber in microwave regime. *Optics express*, 28(4):5306–5316, 2020.

[49] Zhengyong Song, Zhisheng Wang, and Maoliang Wei. Broadband tunable absorber for terahertz waves based on isotropic silicon metasurfaces. *Materials Letters*, 234:138–141, 2019.

[50] Nanli Mou, Xiaolong Liu, Tao Wei, Hongxing Dong, Qiong He, Lei Zhou, Yaqiang Zhang, Long Zhang, and Shulin Sun. Large-scale, low-cost, broadband and tunable perfect optical absorber based on phase-change material. *Nanoscale*, 12(9):5374–5379, 2020.

[51] Zhangjie Luo, Xing Chen, Jiang Long, Ryan Quarfoth, and Daniel Sievenpiper. Nonlinear power-dependent impedance surface. *IEEE Transactions on Antennas and Propagation*, 63(4):1736–1745, 2015.

[52] Hiroki Wakatsuchi, Sanghoon Kim, Jeremiah J Rushton, and Daniel F Sievenpiper. Waveform-dependent absorbing metasurfaces. *Physical review letters*, 111(24):245501, 2013.

[53] L Raghavan and A Srikantha Phani. Local resonance bandgaps in periodic media: Theory and experiment. *The Journal of the Acoustical Society of America*, 134(3):1950–1959, 2013.

[54] Hussein Nassar, Behrooz Yousefzadeh, Romain Fleury, Massimo Ruzzene, Andrea Alù, Chiara Daraio, Andrew N Norris, Guoliang Huang, and Michael R Haberman. Nonreciprocity in acoustic and elastic materials. *Nature Reviews Materials*, 5(9):667–685, 2020.

[55] Christophe Caloz, Andrea Alu, Sergei Tretyakov, Dimitrios Sounas, Karim Achouri, and Zoé-Lise Deck-Léger. Electromagnetic nonreciprocity. *Physical Review Applied*, 10(4):047001, 2018.

[56] Ahmed Kord, Dimitrios L Sounas, and Andrea Alu. Microwave nonreciprocity. *Proceedings of the IEEE*, 108(10):1728–1758, 2020.

[57] Y Shoji, K Miura, and T Mizumoto. Optical nonreciprocal devices based on magneto-optical phase shift in silicon photonics. *Journal of Optics*, 18(1):013001, 2015.

[58] Sergey V Kutsaev, Alex Krasnok, Sergey N Romanenko, Alexander Yu Smirnov, Kirill Taletski, and Vyacheslav P Yakovlev. Up-and-coming advances in optical and microwave nonreciprocity: From classical to quantum realm. *Advanced Photonics Research*, 2(3):2000104, 2021.

[59] Negar Reiskarimian. A review of nonmagnetic nonreciprocal electronic devices: Recent advances in nonmagnetic nonreciprocal components. *IEEE Solid-State Circuits Magazine*, 13(4):112–121, 2021.

[60] Xun-Wei Xu, Yong Li, Baijun Li, Hui Jing, and Ai-Xi Chen. Nonreciprocity via nonlinearity and synthetic magnetism. *Physical Review Applied*, 13(4):044070, 2020.

[61] Cui Kong, Hao Xiong, and Ying Wu. Magnon-induced nonreciprocity based on the magnon kerr effect. *Physical Review Applied*, 12(3):034001, 2019.

[62] Lei Zhang, Xiao Qing Chen, Rui Wen Shao, Jun Yan Dai, Qiang Cheng, Giuseppe Castaldi, Vincenzo Galdi, and Tie Jun Cui. Breaking reciprocity with space-time-coding digital metasurfaces. *Advanced materials*, 31(41):1904069, 2019.

[63] Bogdan-Ioan Popa and Steven A Cummer. Non-reciprocal and highly nonlinear active acoustic metamaterials. *Nature communications*, 5(1):1–5, 2014.

[64] Constantine A Balanis. *Advanced engineering electromagnetics*. John Wiley & Sons, NJ, 2012.

[65] Dan Sievenpiper, Lijun Zhang, Romulo FJ Broas, Nicholas G Alexopolous, and Eli Yablonovitch. High-impedance electromagnetic surfaces with a forbidden frequency band. *IEEE Transactions on Microwave Theory and techniques*, 47(11):2059–2074, 1999.

[66] Daniel F Sievenpiper, James H Schaffner, H Jae Song, Robert Y Loo, and Gregory Tangonan. Two-dimensional beam steering using an electrically tunable impedance surface. *IEEE Transactions on antennas and propagation*, 51(10):2713–2722, 2003.

[67] Aobo Li, Yunbo Li, Jiang Long, Ebrahim Forati, Zhixia Du, and Dan Sievenpiper. Time-moduated nonreciprocal metasurface absorber for surface waves. *Optics Letters*, 45(5):1212–1215, 2020.

[68] AJ Baden Fuller. *Ferrites at microwave frequencies*. IET, London, 1987.

[69] J Douglas Adam, Lionel E Davis, Gerald F Dionne, Ernst F Schloemann, and Steven N Stitzer. Ferrite devices and materials. *IEEE transactions on microwave theory and techniques*, 50(3):721–737, 2002.

[70] Nil Apaydin, Kubilay Sertel, and John L Volakis. Nonreciprocal leaky-wave antenna based on coupled microstrip lines on a non-uniformly biased ferrite substrate. *IEEE transactions on antennas and propagation*, 61(7):3458–3465, 2013.

[71] Armin Parsa, Toshiro Kodera, and Christophe Caloz. Ferrite based non-reciprocal radome, generalized scattering matrix analysis and experimental demonstration. *IEEE transactions on antennas and propagation*, 59(3):810–817, 2010.

[72] Tolga Dinc, Mykhailo Tymchenko, Aravind Nagulu, Dimitrios Sounas, Andrea Alu, and Harish Krishnaswamy. Synchronized conductivity modulation to realize broadband lossless magnetic-free non-reciprocity. *Nature communications*, 8(1):1–9, 2017.

[73] Andrew E Cardin, Sinhara R Silva, Shai R Vardeny, Willie J Padilla, Avadh Saxena, Antoinette J Taylor, Wilton JM Kort-Kamp, Hou-Tong Chen, Diego AR Dalvit, and Abul K Azad. Surface-wave-assisted nonreciprocity in spatio-temporally modulated metasurfaces. *Nature communications*, 11(1):1–9, 2020.

[74] Xiaozhen Yang, Erda Wen, and Daniel F Sievenpiper. Broadband time-modulated absorber beyond the bode-fano limit for short pulses by energy trapping. *Physical Review Applied*, 17(4):044003, 2022.

[75] Aravind Nagulu, Xiang Ni, Ahmed Kord, Mykhailo Tymchenko, Sasank Garikapati, Andrea Alu, and Harish Krishnaswamy. Chip-scale floquet topological insulators for 5g wireless systems. *Nature Electronics*, 5(5):300–309, 2022.

[76] Negar Reiskarimian and Harish Krishnaswamy. Magnetic-free non-reciprocity based on staggered commutation. *Nature communications*, 7(1):1–10, 2016.

[77] Sajjad Taravati, Bakhtiar A Khan, Shulabh Gupta, Karim Achouri, and Christophe Caloz. Nonreciprocal nongyrotropic magnetless metasurface. *IEEE Transactions on Antennas and Propagation*, 65(7):3589–3597, 2017.

[78] Benjamin J Chapman, Eric I Rosenthal, Joseph Kerckhoff, Bradley A Moores, Leila R Vale, JAB Mates, Gene C Hilton, Kevin Lalumiere, Alexandre Blais, and KW Lehnert. Widely tunable on-chip microwave circulator for superconducting quantum circuits. *Physical Review X*, 7(4):041043, 2017.

[79] Li Fan, Jian Wang, Leo T Varghese, Hao Shen, Ben Niu, Yi Xuan, Andrew M Weiner, and Minghao Qi. An all-silicon passive optical diode. *Science*, 335(6067):447–450, 2012.

[80] Boyuan Jin and Christos Argyropoulos. Self-induced passive nonreciprocal transmission by nonlinear bifacial dielectric metasurfaces. *Physical Review Applied*, 13(5):054056, 2020.

[81] Ki Youl Yang, Jinhie Skarda, Michele Cotrufo, Avik Dutt, Geun Ho Ahn, Mahmoud Sawaby, Dries Vercruysse, Amin Arbabian, Shanhui Fan, and Andrea Alù. Inverse-designed non-reciprocal pulse router for chip-based lidar. *Nature Photonics*, 14(6):369–374, 2020.

[82] Ahmed Mekawy, Dimitrios L Sounas, and Andrea Alù. Free-space nonreciprocal transmission based on nonlinear coupled fano metasurfaces. In *Photonics*, volume 8, page 139. MDPI, 2021.

[83] Ahmed M Mahmoud, Arthur R Davoyan, and Nader Engheta. All-passive nonreciprocal metastructure. *Nature communications*, 6(1):1–7, 2015.

[84] Dimitrios L Sounas, Jason Soric, and Andrea Alu. Broadband passive isolators based on coupled nonlinear resonances. *Nature Electronics*, 1(2):113–119, 2018.

[85] Dimitrios L Sounas and Andrea Alù. Fundamental bounds on the operation of fano nonlinear isolators. *Physical Review B*, 97(11):115431, 2018.

[86] Yu Shi, Zongfu Yu, and Shanhui Fan. Limitations of nonlinear optical isolators due to dynamic reciprocity. *Nature photonics*, 9(6):388–392, 2015.

[87] Jie Hu, Sankhyabrata Bandyopadhyay, Yu-hui Liu, and Li-yang Shao. A review on metasurface: from principle to smart metadevices. *Frontiers in Physics*, 8:586087, 2021.

[88] Foez Ahmed, Khushboo Singh, and Karu P Esselle. State-of-the-art passive beam-steering antenna technologies: Challenges and capabilities. *IEEE Access*, 2023.

[89] Tong Cui, Benfeng Bai, and Hong-Bo Sun. Tunable metasurfaces based on active materials. *Advanced Functional Materials*, 29(10):1806692, 2019.

[90] Manideep Dunna, Chi Zhang, Daniel Sievenpiper, and Dinesh Bharadia. Scattermimo: Enabling virtual mimo with smart surfaces. In *Proceedings of the 26th Annual International Conference on Mobile Computing and Networking*, pages 1–14, 2020.

[91] Kshitiz Bansal, Manideep Dunna, Sanjeev Anthia Ganesh, Eamon Patamsing, and Dinesh Bharadia. R-fiducial: Reliable and scalable radar fiducials for smart mmwave sensing. *arXiv preprint arXiv:2209.13109*, 2022.

[92] Sajjad Nassirpour, Alireza Vahid, Dinh-Thuan Do, and Dinesh Bharadia. Beamforming design in reconfigurable intelligent surface-assisted iot networks based on discrete phase shifters and imperfect csi. *IEEE Internet of Things Journal*, 2023.

[93] HL Zhu, SW Cheung, Kwok Lun Chung, and Tong I Yuk. Linear-to-circular polarization conversion using metasurface. *IEEE transactions on antennas and propagation*, 61(9):4615–4623, 2013.

[94] Hengyi Sun, Changqing Gu, Xinlei Chen, Zhuo Li, Liangliang Liu, and Ferran Martín. Ultra-wideband and broad-angle linear polarization conversion metasurface. *Journal of applied physics*, 121(17), 2017.

[95] Houjin He, Shiwei Tang, Ziwei Zheng, and Fei Ding. Multifunctional all-dielectric metasurface quarter-wave plates for polarization conversion and wavefront shaping. *Optics Letters*, 47(10):2478–2481, 2022.

[96] Xiaojun Huang, Xia Ma, Xuewen Li, Jingdao Fan, Liang Guo, and Helin Yang. Simultaneous realization of polarization conversion for reflected and transmitted waves with bi-functional metasurface. *Scientific reports*, 12(1):2368, 2022.

[97] Cormac McDonnell, Junhong Deng, Symeon Sideris, Guixin Li, and Tal Ellenbogen. Terahertz metagrating emitters with beam steering and full linear polarization control. *Nano Letters*, 22(7):2603–2610, 2022.

[98] Fei Ding, Yuanqing Yang, Rucha A Deshpande, and Sergey I Bozhevolnyi. A review of gap-surface plasmon metasurfaces: fundamentals and applications. *Nanophotonics*, 7(6):1129–1156, 2018.

[99] Fei Ding. A review of multifunctional optical gap-surface plasmon metasurfaces. *Progress In Electromagnetics Research*, 174, 2022.

[100] Sidrish Zahra, Liang Ma, Wenjiao Wang, Jian Li, Dexu Chen, Yifeng Liu, Yuedan Zhou, Na Li, Yongjun Huang, and Guangjun Wen. Electromagnetic metasurfaces and reconfigurable metasurfaces: a review. *Frontiers in Physics*, 8:593411, 2021.

[101] Qiong He, Shulin Sun, and Lei Zhou. Tunable/reconfigurable metasurfaces: physics and applications. *Research*, 2019, 2019.

[102] Xiaojian Fu, Fei Yang, Chenxi Liu, Xiaojun Wu, and Tie Jun Cui. Terahertz beam steering technologies: from phased arrays to field-programmable metasurfaces. *Advanced optical materials*, 8(3):1900628, 2020.

[103] Myeongha Hwang, Gyoungdeuk Kim, Jongyeong Kim, and Sangkil Kim. A simultaneous beam steering and polarization converting s-band transmitarray antenna. *IEEE Access*, 10:105111–105119, 2022.

[104] Chun Ni, Ming Sheng Chen, Zhong Xiang Zhang, and Xian Liang Wu. Design of frequency-and polarization-reconfigurable antenna based on the polarization conversion metasurface. *IEEE Antennas and Wireless Propagation Letters*, 17(1):78–81, 2017.

[105] Daniel F Sievenpiper, James H Schaffner, H Jae Song, Robert Y Loo, and Gregory Tangonan. Two-dimensional beam steering using an electrically tunable impedance surface. *IEEE Transactions on antennas and propagation*, 51(10):2713–2722, 2003.

[106] Xin Ge Zhang, Qian Yu, Wei Xiang Jiang, Ya Lun Sun, Lin Bai, Qiang Wang, Cheng-Wei Qiu, and Tie Jun Cui. Polarization-controlled dual-programmable metasurfaces. *Advanced science*, 7(11):1903382, 2020.

[107] Jun Chen Ke, Jun Yan Dai, Ming Zheng Chen, Li Wang, Cheng Zhang, Wankai Tang, Jin Yang, Wei Liu, Xin Li, and Yunfeng Lu. Linear and nonlinear polarization syntheses and their programmable controls based on anisotropic time-domain digital coding metasurface. *Small structures*, 2(1):2000060, 2021.

[108] Biswarup Rana, In-Gon Lee, and Ic-Pyo Hong. Digitally reconfigurable transmitarray with beam-steering and polarization switching capabilities. *IEEE Access*, 9:144140–144148, 2021.

[109] Cheng Huang, Wenbo Pan, Xiaoliang Ma, Bo Zhao, Jianhua Cui, and Xiangang Luo. Using reconfigurable transmitarray to achieve beam-steering and polarization manipulation applications. *IEEE Transactions on Antennas and Propagation*, 63(11):4801–4810, 2015.

[110] Jianjia Hu, Pei-Ling Chi, and Tao Yang. Novel 1-bit beam-scanning reflectarray with switchable linear, left-handed, or right-handed circular polarization. *IEEE Transactions on Antennas and Propagation*, 71(2):1548–1556, 2022.

[111] Erda Wen, Xiaozhen Yang, and Daniel F. Sievenpiper. Real-data-driven real-time reconfigurable microwave reflective surface. *Nature Communications*, 14(1):7736, 2023.